Allowed and forbidden β-decay rates for astrophysical applications

By

Muhammad Majid

Supervised by

Prof. Dr. Jameel-Un Nabi

A thesis submitted for the partial fulfillment
of the requirements for the Degree of
Doctor of Philosophy (Ph.D.) in
Engineering Sciences (Applied Physics)

Faculty of Engineering Sciences
Ghulam Ishaq Khan Institute of Engineering Sciences and Technology
Topi, Swabi, KP, Pakistan.

June, 2018

In the name of Allah, the most merciful and the most compassionate.

"He created the heavens and the earth with truth. He wraps the night around the day and wraps the day around the night, and has made the Sun and Moon subservient, each one running for a specified term. Is He not indeed the Almighty, the Endlessly Forgiving?"

Al-Quran, (Surah Az-Zumar, 5)

Certificate of Approval

It is certified that the research work presented in this thesis, entitled "Allowed and forbidden β-decay rates for astrophysical applications" was conducted by Mr. Muhammad Majid under the supervision of Prof. Dr. Jameel-Un Nabi.

(Supervisor/Pro-Rector Academics)
Prof. Dr. Jameel-Un Nabi
Faculty of Engineering Sciences

(External Examiner)

(Dean)
Prof. Dr. M. Hassan Sayyad
Faculty of Engineering Sciences

(Internal Examiner)

Dedication

Dedicated to my beloved ***parents****, loving* ***siblings*** *and respected* ***teachers****,*
whose utmost efforts and motivations since my childhood, made me what I am today.

Acknowledgements

First of all I am extremely grateful to Almighty Allah, for giving me the strength and perseverance to complete my Ph.D. studies. I would like to thank my supervisor, Prof. Dr. Jameel-Un Nabi (Pro-Rector Academics, GIKI), for proposing interesting thesis project and for his continuous support and enthusiasm toward it. I am grateful to him for expanding my knowledge of physics, both from the academic point of view, but surely also from a human perspective. During my research work, I found him wholehearted and helpful. I found him a very good supervisor and indomitable researcher. He made my debut in the Physics of the Heavens (stars) and the nucleus. I am thankful to Prof. Dr. M. Hassan Sayyad (Dean, FES), Prof. Dr. Ghulam Shabbir (Dean Graduate Studies) Prof. Dr. Sirajul Haq (Dean Student Affair), Prof. Dr. Irgaziev Bakhadir, Dr. M. Zahir Iqbal, Dr. Muhammad Fayaz and Dr. Tahseen Amin for their kind interaction and valuable suggestions during the course and research work. I am thankful to all the faculty members for their full cooperation in this regard. I will never forget the encouraging and sincere help of Muhammad Riaz and Ms. Mavra Ashfaq, doing their Ph.D. in the same field. They gave me a lot of suggestions and guidance during this work. I am also really indebted to Prof. Natalie Jachowicz (Ghent University, Belgium), Mr. Nils Van Diesel (Ph.D. researcher, Ghent university) and Mr. Muhammad Gul (Ph.D. researcher, Ghent university), for their support, suggestions and discussions on netrino-nucleus interaction topics during my foreign six months research stay at Ghent University, Belgium. I am immensely grateful to my sweet brothers Mr. M. Saleh (Chief Coordinator GCS), M. Irfan (Principal GCS) and Engr. Quaid Khan for their sincere help and for bearing with me during the challenges. I am also pleased from my friends and colleagues, especially Prof. Abid Ahmad, Mr. Kabir, Mr. Kaleem, Mr. Mehran Bashir, and Mr. Muneem khan for their encouragement and prayers. All my love and thanks goes to my loving parents, sisters and my life partner, for their support and prayers, which are a constant source of strength for me. Finally I acknowledge the financial support of Higher Education Commission (HEC), Pakistan for giving me fully funded scholarship for my Ph.D. studies. Thanks to IRSIP team HEC, for providing grant for my six months research work at Ghent University, Belgium, this was really a great award for me.

Muhammad Majid

June, 2018

Declaration

I declare that this is my own work and has not been submitted in any form for another degree or diploma at any university or other institution for tertiary education. Information derived from published or unpublished work of others has been acknowledged in the text and a list of references is provided at the end of this dissertation.

Muhammad Majid

June, 2018

Abstract

The allowed charge-changing transitions are considered to be the most general weak processes of spin-isospin ($\sigma\tau$) form that play a crucial role in several nuclear processes. Equally important is their contribution in astrophysics, particularly in nuclear synthesis and supernova-explosions. As per previous simulation results, weak interaction rates on *fp* shell nuclide are considered intensely significant for supernova physics. These transitions have significant influence on the stellar core vis-$\grave{a}$-vis controlling the lepton content (Y_e) of stellar matter throughout the silicon shell burning stages of massive stars to the presupernova and core-collapse stages. Simulation of stellar events require Gamow-Teller (GT) strength distributions, preferably for hundreds of nuclei. Because of scarcity of experimental data, one is compelled to calculate GT strength distributions using microscopic theoretical nuclear models. The knowledge of measured GT strength should be broadened and theoretical attempts should be done to reproduce them and the charge-changing transitions of nuclei that are present far away from the stability line should be calculated. The first-forbidden (FF) transition becomes important, in the circumstances where allowed charge-changing transitions are not favored, specifically for neutron-rich (heavier) nuclide due to phase space considerations.

In this thesis the deformed proton-neutron quasi-particle random phase approximation (pn-QRPA) theory was applied in stellar environment, for the investigation of allowed GT and unique first-forbidden (U1F) transitions ($|\Delta J| = 2$) strength for a number of astrophysical important (medium heavy and heavy) nuclei. The calculated terrestrial beta-decay half-lives ($T_{1/2}$) values were compared with previous theoretical work and experimental results where it was concluded that the deformed pn-QRPA calculation are in decent comparison with measured data. The agreement of the calculated $T_{1/2}$ values with the experimental data provide an idea about the correctness of the calculated weak-rates. The stellar weak interaction rates (GT and U1F) were computed over broad range of stellar temperature (0.01 GK – 30 GK) and density (10 – 10^{11} g/cm^3) domain for astrophysical applications.

We have compared the calculated weak-rates with previous other theoretical models compilations (wherever possible). Differences were noticed with these previous models results and their impacts on the presupernova mechanism and for core-collapse supernova were discussed.

In a recent study by Cole et al. [A. L. Cole, et al., Phys. Rev. C 86, 015809 (2012)], it was concluded that QRPA calculations show larger deviations and overestimate the total experimental GT strength. It was also concluded that QRPA calculated electron capture rates exhibit larger deviation than those derived from the measured charge-changing transitions strength. This work has probed the conclusion of the Cole et al. study and provides useful information on the performance of QRPA-based models. Our findings showed that this is not the case for all type of QRPA models. In this work we did not assume Brink-Axel hypothesis as considered in previous shell models calculation. This made the current calculation unique and fully microscopic in nature. It is hoped that these microscopic compilations of stellar rates (allowed GT and U1F) will demonstrate enormous significance for core-collapse simulator worldwide. Our study suggests that the addition of rank (0 and 1) operators in FF transitions can further improve the comparison which remains unattended in this work.

Contents

List of Figures

Chapter 1

Chapter 2

Chapter 3

Chapter 4

Chapter 5

List of Tables

List of Abbreviations

$M_\odot$	Solar Mass
SN II	Type II Supernovae
SN Ia	Type I Supernovae
s-process	Slow Neutron Capture Process
r-process	Rapid Neutron Capture Process
p-process	Proton Capture Process
rp-process	Rapid Proton Capture Process
NSM	Neutron Star Mergers
MeV	Mega Electron Volt
GT	Gamow-Teller
FF	First-Forbidden
U1F	Unique First-Forbidden
TDA	Tamm Dancoff Approximation
HF	Hartree-Fock
RPA	Randon Phase Approximation
pn-QRPA	proton-neutron Quasi-particle Random Phase Approximation
pp	Particle-Particle
ph	Particle-Hole
HBF	Hartree-Fock-Bogoliubov
BCS	Bardeen-Cooper-Schrieffer
IAS	Isobaric Analog State
XUNDL	Experimental Unevaluated Nuclear Data List

List of publications during my Ph.D. studies

Published Papers

- **M. Majid** and J.-U. Nabi, "Study of electron capture rates on chromium isotopes for core-collapse simulations", *Rom. Rep. Phys.*, 68, 1447-1465 (2016).
- J.-U. Nabi, N. Çakmak, **M. Majid** and Çevad Selam, "Unique first-forbidden β-decay transitions in odd-odd and even-even heavy nuclei", *Nucl. Phys. A*, 957, 1-20 (2017).
- J.-U. Nabi and **M. Majid**, "Gamow-Teller strength and lepton captures rates on $^{66-71}$Ni in stellar matter", *Int. J. Mod. Phys. E*, 26, 1750005 (2017).
- **M. Majid**, J.-U. Nabi and G. Daraz "Allowed and unique first-forbidden stellar electron emission rates of neutron-rich copper isotopes", *Astrophys. Space Sci.*, 362, 108 (2017).
- M. Fayyaz, J.-U. Nabi, **M. Majid**, "Gamma heating and Neutrino cooling rates due to weak interaction processes on *sd*-shell nuclei in stellar cores", *Astrophys. Space Sci.*, 362, 132 (2017).
- **M. Majid**, J.-U. Nabi and M. Riaz "Study of Gamow-Teller strength and associated electron capture rates on odd-A stable nuclei in stellar matter ", *Int. J. Mod. Phys. E*, 27, 1850019 (2018).
- J.-U. Nabi, T. Bayram and **M. Majid**, "Ground-state nuclear properties of neutron-rich copper isotopes and lepton capture rates in stellar matter", *Act. Phys. Pol. B*, (accepted on 28 May, 2018).

Submitted Paper

- J.-U. Nabi, **M. Majid** and Ramoona Shehzadi, "Gamow-Teller strength and (anti)neutrino energy loss rates on Ni isotopes", Submitted.

Chapter 1

Stellar evolution and weak interaction processes

1.1 Introduction

Basic laws describing the astrophysical events are mostly dealt within two main branches of physics, nuclear physics and astrophysics. The synergic efforts in theoretical as well as experimental research in these two domains have given rise, to the fascinating interdisciplinary field of nuclear astrophysics in the last decades. To understand the story of the origin of the elements as well as of ourselves, is a very interesting and attractive question in physics. It's a challenging task to answer this question. It requires to intensely dig simultaneously into astrophysics and nuclear physics, known as nuclear astrophysics. The former tells us from where the nuclei have been formed, while the later shows how they have been formed. The elements that make up our bodies reflect the cosmic abundance of the elements, and their very presence on the Earth is in itself the part of the evolutionary history of stars. Nuclear astrophysics basically deals about the naturally existing nuclei production and how they evolved into our present universe with different nuclear mechanisms, commencing with the Big Bang and ongoing today in stellar objects such as stars, x-ray bursters, and supernovae. The study of the present thesis is intended to establish a decent contribution to the development of this field.

1.2 Birth and death of the stars

Stars are considered the sole laboratories in which all kinds of interactions happening in the universe come into the play and play a crucial role in the evolutionary stages of high mass stars. Stars begin the birthing from interstellar clouds of gases and dust particles. Due to gravity these gases and dust particles are compressed and thus create a protostar. As the protostar further contracts, its density and temperature increases. Due to Coulomb repulsive forces the hydrogen (H) nuclide repel each other, specifically at low temperature. But as the hydrogen nuclei becomes enough close to each other, they attract each other due to the short range strong nuclear force. The increase in stellar temperature provides the energy necessary for this attraction to form a nuclei. As the temperature rises the kinetic energy of the hydrogen nuclei increases, and this energy becomes high enough to overcome the Coulomb barrier and start fusion reaction. At this stage, the star life begins known as main sequence star where most of its life will spend, producing helium (He) nuclei through fusion reaction [1]. Stars are also able to fuse elements having higher masses depending on their mass and stars whose mass M $\gtrsim$ 8M$_{\odot}$ keep on fusing the heavier nuclei until a core having iron group nuclide is formed through silicon burning phases. In this mass region (A $\approx$ 56), the Coulomb barrier suppresses further reactions due to the maximum binding energy (B.E) per nucleon of these nuclei. The B.E per nucleon (B.E/A) versus mass number can be seen in Fig. 1.1. Once the core of massive stars become made of the iron-group nuclei, this stops fusion reaction inside the core, because fusing iron-group nuclei would carry off energy instead of providing it [1]. This ultimately pushes the star to core collapse supernova stage. Thus the star life ends through supernova (SNe). Majority of the nuclide having mass number A $\sim$ 60 are formed during the main sequence phases of stellar evolution, however stellar weak reactions become significant in later stages, when the stellar core temperature and density become larger, due to which the Fermi energy of the degenerate leptons gas rises and thus favors the lepton capture reactions. Indeed, it is a well-known fact that stellar weak interaction mechanisms are very essential processes to recognize the stellar evolution late phases, thus playing a decisive role to find out stellar structure of presupernova as well as the nucleosynthesis of heavier elements [2].

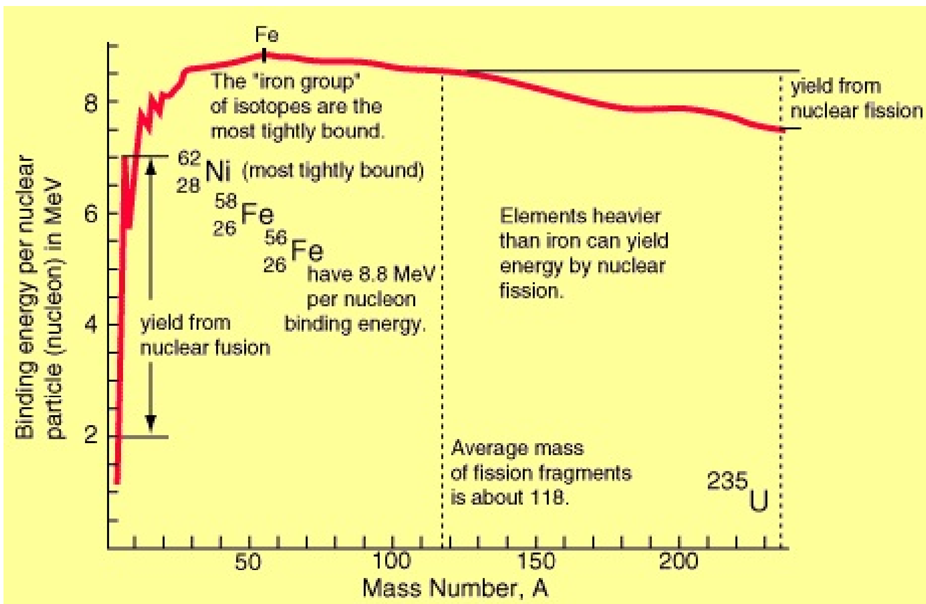

Figure 1.1: Binding energy per nucleon as a function of mass number, reproduced from [3].

Less massive stars end their lives after main sequence phase and become the red giants and ultimately converted to white dwarfs (discussed in details in the next sections). These kinds of stellar explosions are significant, because they are considered the main sources of heavier elements in the nature.

1.3 Supernovae classification

The ancient Chinese observers have labeled these events initially as ”guest star” [4]. Centuries later, the name ”nova” was basically introduced by Tycho Brahe, with the publication of his book ”De Nova Stella” meaning ”Of the New Star” [5]. Fritz Zwicky in the 1930s, has given the name ”supernovae” to differentiate it from more general novae. Minkowski in 1941 has divided the supernova into two different types i.e. Type-I and Type-II supernova, depending on whether they depict or do not display the hydrogen lines in their spectrum, respectively. By observing the large amount of observational data in the 1980s, it became clear that the Type-I supernova should be further classified (e.g. Harkness Wheeler (1990)). By then Type-I supernovae were viewed, which do not display the strong absorption feature of Si II characteristic for the majority of Type Is, now known as Type Ia. The events having no Si II feature were classified further into Type-Ib and Type-Ic, depending on whether they posses the He-lines or not, respectively. Type-II supernova are normally less homogeneous. Therefore, their light curve shape is taken into account as a further parameter for the sub division of these astrophysical events. It is to be noted that some astrophysical events are noticed, which demonstrate prominent hydrogen lines in their spectrum initially, but are absent late-time spectrum (Filippenko 1988, Matheson et al. 2000). These hybrid stellar events, between Type-II and Type-Ib/c, are now known as Type-IIb. It is considered that Type-Ia SNe are basically thermonuclear. Though the accurate mechanism of these catastrophic explosions are not well-known for either astrophysical phenomena, however, it is obvious that weak interaction rates, especially the lepton capture rates, play a decisive role [6].

1.3.1 Core-collapse supernova

Core-collapse SNe occurs in massive stars having M $\gtrsim$ 8M$_\odot$, this type of explosion takes place when the massive star used all its nuclear fuel necessary for fusion reactions inside the core. These stars have much shorter lifespan and are able to ignite the ashes of their earlier burning phases via continual contraction. The energy output of each burning phase reduces as compared to the earlier phase; due to this the massive stars have to burn their fuel more rapidly in order to balance the strong gravitational attractive force. This mechanism of contraction and burning of various phases can carry on up to the iron group nuclei. At this point, the stars are not capable to produce more energy and their inner parts begin to collapse. The massive stars eventually explode in a catastrophic way known as a core-collapse SNe. This mechanism is halted by the pressure of the degenerate electrons in the ionized matter. Chandrasekhar showed that this could only stabilize a mass specified by $M_{ch} = 1.44(2Y_e)^2)[1 + F(T)]M_\odot$, where Y_e represents the electrons to baryons ratio and F(T) shows the finite temperature correction for massive stars its value is generally considered as 0.2–0.3. It is known as Chandrasekhar mass (M_{ch}) limit. As the core contracts the electrons Fermi energy increases, so capture of electrons become energetically favorable. Due to this capture process Y_e decreases and as a result also M_{ch}. In this process, the energetic electron neutrinos are also produced and escape from the core. Therefore, it reduces the energy of the core and this will eventually trigger almost free-fall collapse in the core [7]. The core-collapse phenomenon ejects the matter above the inner core into the interstellar medium and leaves behind a neutron star. Depending on mass of the star, there is also possibility that gravity could overcome the neutron degeneracy pressure and the massive star convert into a black-hole. Fig. 1.2 shows the remnant of a core-collapse SNe (SN 1987a) . During the pre- and post-collapse stages, leptons capture happen on a various pf- and sdg-shell nuclide [8], many of them are unstable (terrestrial conditions). Furthermore, because of high temperature leptons capture process can occur on the thermally populated excited levels. Measurements of all these excited states transitions are not possible experimentally.

Therefore, it is critical that theoretical nuclear models should be established and tested against measurements [6].

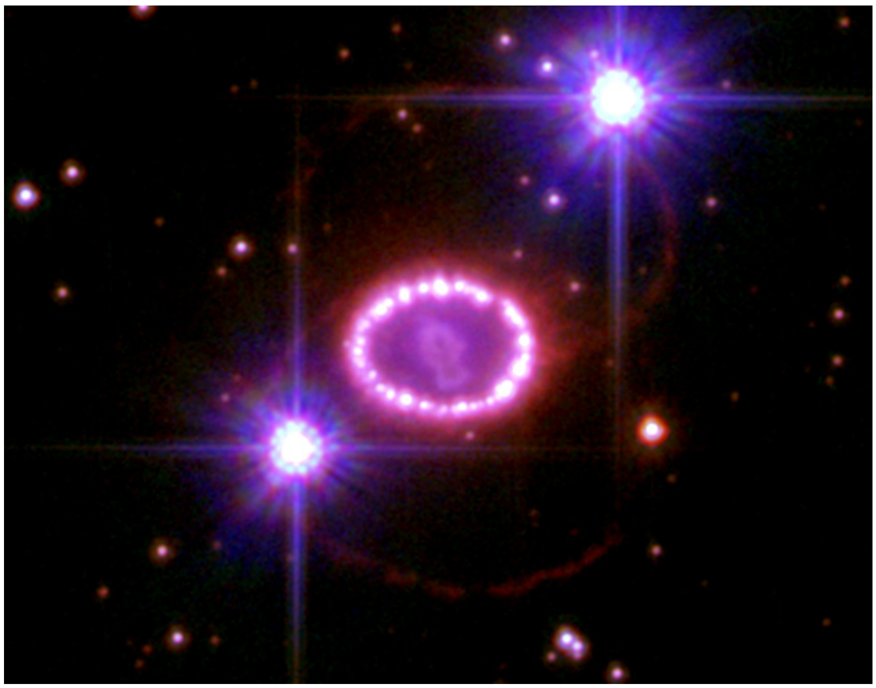

Figure 1.2: The remnant of supernova 1987a. Courtesy Space Telescope Science Institute/NASA [9].

1.3.2 Thermonuclear supernovae

These kinds of SNe do not include the H-lines in their light spectral curves, and, however, they contain the Si-lines having wavelength equal to $6150A^o$ in their spectrum. Thermonuclear explosions are responsible for the production of these Type Ia SNe. This kind of SNe begin in a binary star systems. In binary star system two stars revolve around each other or both orbits around a common point. In this process, one star (white dwarf) attracts the matter from the outer layer of the companion star due to the gravitational pull. The white dwarf density increases and it mass reaches to Chandrasekhar mass (M_{ch}) limit (1.4

$M_\odot$). When the dwarf core mass is less than the 1.4 $M_\odot$, it remains stable because the degenerate pressure of electrons and gravitational pull balance each other. But once the core mass increases from M_{ch} it becomes unstable. At this stage, the outward electrons degenerate pressure further cannot compete with the huge gravity. The ignition at core of the dwarf begins the thermonuclear reactions and finally thermonuclear explosion occurs with a supersonic speed and releases huge amount of energy (10^{51} ergs), the sun would radiate that much of energy in approximately 8 billion years. This huge amount of energy is produced by several thermonuclear reactions that begin from ^{12}C and ^{16}O nuclei and ends in iron-group nuclei. During these nuclear reactions intermediate-mass isotopes of neon, magnesium, silicon and calcium are also produced. Thermonuclear SNe thus provide the raw matter for the formation of new stars and planets. However, Type Ia supernova are not considered to be significant contributors to stellar nucleosynthesis beyond the iron-group nuclei. Type Ia SNe are considered to be the brightest event, but it happened very rarely, approximately 10 times rare as compared to core collapse SNe. This type of events are used by the astronomers for the exploration of the universe geometry, due to this reason they serve as "standard candles" in the astronomy. The Type I SNe are further divided into Type Ib and Ic. In type Ib supernova there is presence of strong He-lines in their spectrum [10]. While in Type Ic spectral curves there are no strong He-lines or having weak He absorption lines. The Type Ib and Type Ic supernova are less brighter than Type Ia.

1.4 Nucleosynthesis of heavy elements

After the Big Bang the Universe consisted of a primordial mixture of only hydrogen and helium with traces of a few heavier elements. Almost all of the nuclei that exist today have been formed in stars, which fuse lighter elements to form heavier ones, generating huge amount of energy. Depending on the properties of stars at various phases of its life, it can release energy from different thermonuclear reactions. The nuclei with the highest binding energy per nucleon are located around the iron peak having Z $\approx$ 26 as shown in Fig. 1.1.

These are the nuclei that are primarily synthesized by silicon burning in thermodynamic equilibrium. For heavier elements, the binding energy per nucleon decreases, which means that fusion reactions consume energy instead of releasing it. Therefore, fusion reactions do not produce elements heavier than iron. Moreover, as the number of protons in the nuclei grows, the resulting Coulomb barrier increases and reactions involving charged particles become more and more unlikely. The many existing elements heavier than iron must have been produced by reactions that involve neutral particles which are therefore not affected by the high Coulomb barrier: neutron capture reactions. Some proton-rich isotopes are considered to be produced by a succession of rapid proton captures (rp) process.

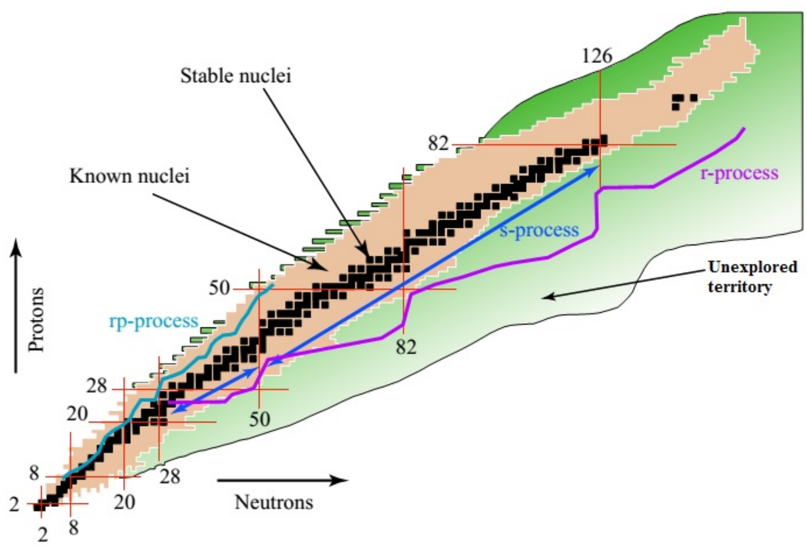

Figure 1.3: Schematic outline of the nuclear reactions sequences that generate energy and create new elements in stars and stellar explosions, reproduced from [11].

1.4.1 Neutron capture process

When a nucleus captures a neutron it generates the next massive isotope of the same element. Capturing of free neutrons occur most readily by nuclide having high neutron capturing cross section and are abundant. Therefore, capturing of neutrons mostly occur onto ^{56}Fe nuclide, which are abundant because of their formation by the ^{56}Ni–^{56}Co–^{56}Fe disintegration network in supernovae. In neutron capture process neutron-rich nuclei are produced which are normally unstable and disintegrate through the electron emission (EE) weak decay process, thereby nuclei with larger charge number are formed. In general, the neutron captures processes are classified into two main processes: the rapid (r) and slow (s) -process paths [12,13]. The nuclide possessed in these r- and s- processes are depicted in Fig. 1.3. To track the path of this process, one needs to know how likely it is that the unstable isotope can β-decay before it can capture an additional neutron. This is where a distinction between the s and r -processes are made. The pattern of the isotopes that are mainly created due to neutron capture reactions is mostly determined by their capture cross sections. Some elements are particularly stable and do not capture neutrons. These acts as bottlenecks of the path which create a pile up at these particular isotopes. From shell model this behavior can be understood. Analogous to the electron distribution in atoms, the nucleons are also distributed in shells. The nucleons shells are closed at magic numbers. For isotopes heavier than iron the magic neutron numbers 50, 82 and 126 are relevant and therefore these nuclei are particularly stable against further neutron captures and show the low capturing cross-section. The detailed discussion on slow and rapid neutron capture process are shown in the following sections.

1.4.1.1 The s-process

In case of slow neutron capture process (s-process), the time scale for beta-decay of unstable isotopes is generally lower than that of neutron captures. S-process elements are created when iron peak elements capture free neutrons. Since this process requires the earlier production of a seed nucleus (e.g. Fe), the s-process is classified as a secondary process. When reaching an unstable isotope, the β-decay forms a nucleus of another element with one more proton and one less neutron. Hence, the s-process path goes toward the valley of stable nuclide and creates stable target nuclei along this path. The neutron capture process mech-

anism is depicted in Fig. 1.4. The low neutron densities which are required to meet the conditions for the s-process are approximately 10^7 cm^{-3} to 10^{10} cm^{-3} [14]. There exists a decent qualitative image of the s-process in nature today and it is quite well understood than the rapid capture process (for more discussion see Refs. [14–16]).
The distribution of Solar-System abundance produced as a result of s- and r- process mechanism are shown in Fig. 1.4.

In the Solar-System abundance there are typically three main peaks in the s-process contribution. The first peak includes the stable elements having magic neutron number equal to 50, for example, ^{86}Kr, ^{87}Rb, ^{88}Sr, ^{89}Y and ^{90}Zr. As these nuclei are stable, therefore their neutron capture cross-section is low and an abundance peak piles up, the so called light s-process peak. The second peak produces the isotopes around Ba-Ce, having magic neutron number equal to 82, known as heavy s-process peak. The last peak of the s-process path forms the most massive stable nuclei (Pb and Bi), with 126 neutrons (see Fig. 1.4).

1.4.1.2 The r-process

In this type of neutron capture process, the iron-group nuclide are bombarded with an enormously huge neutrons flux, as a result highly neutron-rich unstable nuclei are formed. This mechanism of rapid neutron capture process (r-process) is the significant way to create the heaviest elements such as thorium and uranium, needs extremely huge neutron densities of 10^{20}- 10^{25} cm^{-3}. As this process needs extreme environment, so one of the main sites of r-process is believed to be supernovae explosions. Also the more exotic occurrences like black hole/neutron star mergers are also considered sites for the r-process (detailed discussion may be seen in Ref. [17]).

This process results in the production of most unstable nuclei that are present in nature, therefore, their decay channel and half-lives measurements are extremely hard to make with laboratory experiments. The r-process also piles up at elements having magic neutron numbers. However, in comparison to the s-process, the r-process approaches each of the closed neutron-shells at lower mass number, because it runs far from the line of stability zone. In this process, the pile up occurs at the magic nuclei that are not stable and will decay back to the stability region, conserving the mass number. Therefore, the peaks of r-process are located at mass numbers that are less by around 10 than those of the s-process isotopes, as shown in Fig. 1.4. For example, there is a pile up at heavier unstable nuclide of Cd, In and Sn having magic neutron number equal to 82, which eventually decay to produce a peak at Xe, around A≈130 [18].

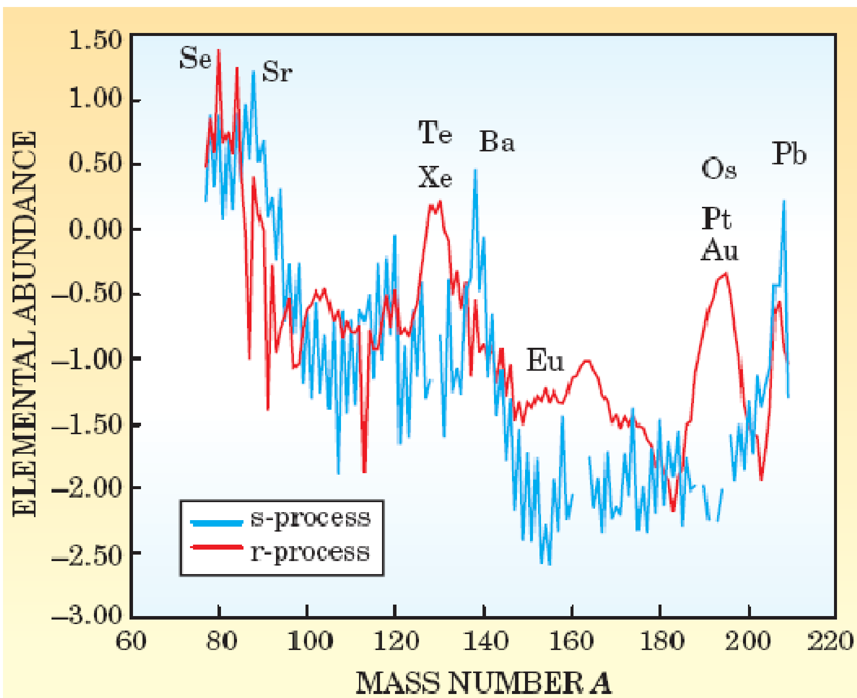

Figure 1.4: The contributions of s- and r- process to solar-system abundances. The elemental abundance is given as $\log(N_A/N_H) + 12$, where N_A and N_H are the number abundances of the nuclei with mass number A and of hydrogen, respectively [19].

1.5 β-decay process

The history of β-decay began in 1896 with the discovery of radioactivity by Henri Becquerel. Within a few years it was understood that three kinds of invisible radiations alpha (α), beta (β) and gamma (γ) are emitted from unstable isotopes. One great puzzle relevant to the beta-decay mechanism was that the energies of the electrons emitted were observed to be continuous, in contrast with α and γ-decay. This non-discrete emitted electrons distribution energy was a puzzling measured result, that was observed in the 1920s since it seemed to contradict the law of conservation of energy. The emitted β-particle energy distribution begins from zero to an upper limit, that was equal to the difference of the quantized nuclear energy states. This confusion was cleared by Pauli and gave the idea of existence of a new weakly-interacting particle known as neutrino, which is emitted in the β-decay process. In 1930 this was a revolutionary step as the neutrino was the carrier of the 'missing' energy. Another puzzle in weak β-decay interaction understanding was that the emitted particles did not exist inside the nucleus. Fermi in 1934 gave the idea that in weak β-decay mechanism, the electron and antineutrino particles are produced during the decay process. Fermi assumed that the creation of these particles are analogous to the photon emission that occur in atomic as well as in nuclear decay processes and he constructed the theory for weak β-decay interaction in this manner. On the contrary, to the electromagnetic interaction, the beta-decay process are considered to be short range. In quantum field theory (QFT), the range is inversely proportional to the exchange charge carrier masses. Therefore, the exchange of a hypothetical particle known as intermediate boson ($W^{\pm}$) was assumed. In this manner, the symmetry aspects related to the electromagnetic interaction and weak-decay process are introduced.

The most general weak-decay process are given below:

β^- decay: $\quad {}^{A}_{Z}X \longrightarrow {}^{A}_{Z+1}X + \overline{e} + \overline{\nu}$

β^+ decay: $\quad {}^{A}_{Z}X \longrightarrow {}^{A}_{Z-1}X + e^+ + \nu$

Electron capture: $\quad {}^{A}_{Z}X \longrightarrow {}^{A}_{Z-1}X + \nu$

Positron capture: ${}^{A}_{Z}X + e^{+} \longrightarrow {}^{A}_{Z+1}X + \overline{\nu}$

Neutrino capture: ${}^{A}_{Z}X_{N} + \nu \longrightarrow {}^{A}_{Z-1}X_{N+1} + \overline{e}$

Anti-Neutrino capture: ${}^{A}_{Z}X_{N} + \overline{\nu} \longrightarrow {}^{A}_{Z-1}X_{N+1} + e^{+}$

When a nucleus undergoes β-decay this involves the weak interaction and a change of a quark flavor inside one of the nucleons. For example, in β^{+}-decay (positron emission) a proton will convert into a neutron and in this process an up quark decays into a down quark. It is due to the fact that proton consist of two up quarks and one down quark, but in β^{+}-decay it converts into neutron, which consist of two down quarks and one up quark. This conversion of an up quark in the proton into a down quark is basically mediated by a gauge boson. W^{+} boson is emitted in case of β^{+}-decay, which in turn transforms into a positron and a neutrino. The final product is therefore neutron together with the positron and neutrino carrying away energy and momentum. Charge is conserved in the weak-decay processes.

1.6 Fermi theory of β-decay

The theory for beta decay was developed by Fermi in 1934, to include the neutrino, presumed to be massless and chargeless particle, dealing with the calculation of the transition probability of the process of β-decay. This cannot be done starting from any other theory. A complete new force had to be introduced to explain the β-decay transition which transform neutron into proton or proton into neutron. In these reactions electron (or positron) and antineutrino (or neutrino) are also produced. Such a force was introduced by Fermi, using the analogy with the electromagnetism. The transition probability in the weak β-decay process can be specified in terms of the first order, time-dependent perturbation theory, later known as the Fermi Golden Rule,

$$\lambda = \frac{2\pi}{\hbar} \mid \langle f|H_{\beta}|i\rangle \mid^{2} \rho_{f}, \tag{1.1}$$

where $\langle f|H_\beta|i\rangle$ is the matrix element of the interaction take place among the initial ($|i\rangle$) state and the final ($|f\rangle$) state of the complete system (nucleus and other relevant light particles). In the above equation ρ_f represents the density of final states. Whereas, the final state of the system is given by the electron and neutrino momenta and energies, (p_e, E_e) and (p_υ, E_υ), with $E_\upsilon = cp_\upsilon$.

The nature of the interaction (H_β) in β-decay was unknown in Fermi's time. But in considering all possible shapes, he specified that H_β should be replaced with an operator O which could, mathematically, take the form of a vector, scalar, pseudoscalar, axial vector or tensor. So, in case of β-decay,

$$| \langle f|H_\beta|i\rangle |= \sum g \int d\overrightarrow{r}[\Phi^*\psi_e^*\psi_\upsilon^*]O\Phi_i, \tag{1.2}$$

where the terms Φ^*, ψ_e^* and ψ_υ^* show the final wave-functions of the system after the beta decay. The value of 'g' represents the strength of the coupling interaction between initial and final states. The electron and neutrino are treated like free-particles, thus their wave functions have the form,

$$\psi_e(\overrightarrow{r}) = \frac{1}{\sqrt{V}}e^{i\overrightarrow{p}_e.\overrightarrow{r}/\hbar}, \psi_\upsilon(\overrightarrow{r}) = \frac{1}{\sqrt{V}}e^{i\overrightarrow{p}_\upsilon.\overrightarrow{r}/\hbar}. \tag{1.3}$$

If we expand the exponentials, using the fact that over the nuclear volume $pr \ll 1$, we have the allowed approximation. If we replace the electron and neutrino wave functions in Eq. 1.2 and use the allowed approximation, the matrix element is now $M_{fi} = g\int d\overrightarrow{r}\Phi_f^*O\Phi_i$, so the decay rate is

$$\lambda = \frac{g^2}{2\pi^3\hbar^7}\int \frac{dp_\upsilon}{dE_f}p_e^2p_\upsilon^2|M_{fi}|^2dp_e, \tag{1.4}$$

for a fixed E_e the term $\dfrac{dp_\upsilon}{dE_f} = 1/c$. On the other hand, if we define the Q as the total decay energy, then the neutrino momentum is given as $p_\upsilon = (Q - T_e)/c$. The β-decay rate is now represented as

$$\lambda = \frac{g^2}{2\pi^3\hbar^7c^3}\int dp|M_{fi}|^2p^2(Q - T_e)^2, \tag{1.5}$$

but here we are not taking into account the interaction between the beta particle and the Coulomb field in the daughter nucleus. For Coulomb effect consideration, an additional factor is added to the decay rate formalism, where Z_d and T_e represent the charge number of the daughter nuclide and kinetic energy of emitted β particle, respectively. The total β-decay rate is now given as

$$\lambda = \frac{g^2|M_{fi}|^2}{2\pi^3\hbar^7 c^3}\int p^2(Q-T_e)^2 F(Z_d,T_e)dp, \tag{1.6}$$

which can be written as;

$$\lambda = \frac{g^2|M_{fi}|^2}{2\pi^3\hbar^7 c^3} m_e^5 c^7 f(Z_d,T_e)dp. \tag{1.7}$$

This integral depends on Z_d and the maximum electron energy, however, the constants in the equation are added in order to make the function $f(Z_d,T_e)$ dimensionless. This function is called the Fermi integral and it is evaluated for values of Z_d and T_e. Knowing that $\lambda = \frac{\ln 2}{t_{1/2}}$, it leads to

$$f(Z_d,T_e)t_{1/2} = \frac{2\pi^3\hbar^7\ln 2}{g^2 m_e^5 c^4 |M_{fi}|^2}. \tag{1.8}$$

The quantity on the left side of Eq. 1.8 is known as ft-value or the comparative half-life. It provides a standard measure to calculate the β-decay transition probabilities in different nuclide and provides the information about the nuclear matrix element and their nuclear wave-functions.

1.7 Allowed and forbidden weak-decays

In weak beta decay reactions there are different quantum mechanical operators governing the transition probabilities among the parent and daughter nucleus states. Generally there exist two main types of allowed charge-changing transitions, "Fermi" and "Gamow-Teller (GT)". The operators of these charge-changing transitions acts on nuclear wave functions to transform a proton into neutron or vice-versa. For example, an isospin raising operator will transform a proton into a neutron, however the isospin lowering operator transform neutron

to proton. An isospin lowering operator acting on a proton will yield a null wave function, essentially it annihilates the proton state. An isospin raising operator acting on a neutron does the same. In the decay the emitted particles can carry away angular momentum. Decays with smaller angular momentum are more probable than those with larger angular momentum. $L = 0$ decays are called "allowed". The emitted β-particle and the neutrino intrinsic spins can couple to S = 0 or S = 1. In the case of allowed decay, the former is referred to as Fermi decay, and the latter as GT decay. Fermi decay occurs between states of identical isospin, i.e. ΔT = 0 and has a very fast decay time, as it requires no change in angular momentum, isospin or parity. The Fermi and GT decays are governed by different operators represented as O_F and O_{GT}.
The matrix elements of Fermi is given as

$$M_{fi} = M_F = g_V \int d\overrightarrow{r}\,\Phi_f^* O_F \Phi_i, \tag{1.9}$$

and for GT decays is specified as

$$M_{fi} = M_{GT} = g_A \int d\overrightarrow{r}\,\Phi_f^* O_{GT} \Phi_i. \tag{1.10}$$

The Fermi transition operator is specified as $O_F = \sum_i \tau^{\pm}(i)$, where τ^+ and τ^- denote the isospin raising (β^+) and lowering (β^-) operators, respectively. For GT transitions the corresponding operator is $O_{GT} = \sum_i \overrightarrow{\sigma}(i)\tau^{\pm}(i)$, where $\overrightarrow{\sigma}(i)$ are the Pauli spin matrices, which also act on the ith nucleon. The GT operator also includes a Pauli spin matrix operator, for change in spin. In term of Fermi and GT matrix elements equation 1.8 can be written as

$$ft_{1/2} = \frac{K}{|M_F|^2 + \frac{g_V^2}{g_A^2}|M_{GT}|^2} = \frac{K}{B(F) + \frac{g_V^2}{g_A^2}B(GT)}, \tag{1.11}$$

where $K = \frac{2\pi^3\hbar^7 \ln 2}{g_V^2 m_e^5 c^4}$, *B(F)* and *B(GT)* denote the reduced transition probabilities of Fermi and GT strengths, respectively. Since the work done by G. Gamow and E. Teller [20], the calculation of the so-called GT-matrix elements from β-decay and charge-exchange reactions has led to a series of discoveries relevant to the spin-isospin transitions properties as well as to the nuclear structure of the nuclei. These GT transitions matrix elements provide the valuable information on the spin-isospin excitations in nuclide, which are also of great significance in the extension and testing of present nuclear models.

β-decay process posses higher values of lepton orbital angular momenta (L) are known as forbidden β-decay transitions. These transitions are usually less probable as compare to allowed transitions. Each value of lepton orbital angular momenta corresponds to higher order of forbiddenness. For example, in case of weak-decays with L = 1, is called first-forbidden (FF) (in this work FF transitions are of interest). L = 2 is known as second forbidden and so on. Both Fermi and GT transitions can exist for each forbidden decay. If the emitted beta particle and neutrino have spins anti-parallel then ΔJ = 0, 1 (Fermi type). In case of GT transitions the spins are aligned so ΔJ = 0, 1, 2. In FF transitions due to L = 1, the parity changes between final and initial states. The selection rules for allowed and forbidden transitions and their range of *ft*-values are shown in Table 1.1.

Table 1.1: Selection rules and observed range of log*ft* values for nuclear β-decay from [21]

Type of Transition	ΔJ	ΔT	$\Delta\pi$	$\log_{10}ft_{1/2}$
Super allowed	$0^+ \rightarrow 0^+$	0	No	3.1 - 3.6
Allowed	0,1	0,1	No	2.9 - 10
First Forbidden	0,1,2	0,1	Yes	5 - 19
Second Forbidden	1,2,3	0,1	No	10 - 18
Third Forbidden	2,3,4	0,1	Yes	17 - 22
Fourth Forbidden	3,4,5	0,1	No	22 - 24

In case of forbidden transitions the *ft*-values are larger (less probable). Because in forbidden decays the L > 0, so the angular momentum barrier prevents the emission of leptons. This causes reduction in the forbidden nuclear matrix element and, hence *ft*-values becomes increases. Generally, the calculation of forbidden transition strength is a difficult job as compared to allowed transitions [21].

1.8 Astrophysical significance of stellar weak-decay rates and pn-QRPA model

The connection between the generation of energy in stars and weak interaction leads to large-scale stellar events. Supernova explosions and related physics are one of the most studied phenomena to be known in astrophysics. Supernovae are intimately connected with the nucleosynthesis problem (for detail see [19]). The weak decay processes are the crucial constituents in all major astrophysical events. The core of the massive star collapses due to weak interaction reactions activating a supernova explosion. Another key phenomenon where weak interactions play a significant part includes neutronisation of stellar core via capturing of electrons by nuclei and by free protons. This process effects the creation of heavier elements beyond iron through r-process. The stellar weak-rates determine the mass of the core and provide a fair estimate of the fate and strength of the shock waves that are created as a result of supernova outburst [22, 23]. The weak interaction properties of heavy nuclide are essential in order to understand the r-process. Though in astrophysical context the mechanism of the rapid neutron capture reaction is not accurately understood, however it is generally considered that it occur in an extremely explosive situations containing intensely high neutron densities ($\geq 10^{20}$ cm^{-3}) and high temperatures (T $\geq 10^{9}$ K). In these circumstances, the neutrons are captured by the nuclei more rapidly as compared to the β-decays and in the nuclear chart the r-process path runs toward the neutron-rich domain with comparatively small (and having round-about constant) neutron separation energies of $\lesssim$ 3 MeV [24]. The allowed charge-changing transitions are the most general weak nuclear reactions of spin-isospin ($\sigma\tau$) kind. These processes play a significant role in several astrophysical reactions in the domain of nuclear physics. Equally important is their contribution in astrophysics, particularly in nuclear synthesis and supernova-explosions. In situations where allowed charge-changing transitions are not favored, then the first-forbidden (FF) decays play a significant role, mainly in heavy nuclide. In case of heavier nuclide, the FF transitions took part mostly because of phase-space amplification.

The theoretical explanation of weak processes, especially the double β-decay process, is an open question for the nuclear-structure theories [25]. The calculated theoretical as well as measured results can be seen in [26]. The analysis of some of the recent developments, both in experiments and theory were discussed in [27]. The estimation of beta decay half-lives ($T_{1/2}$), in accordance with the measured values, is one of the challenging difficulties for nuclear theorists. The β-decay rates and half-lives of nuclei are determined widely by using various nuclear models. Takahashi *et al.* [28] calculated these rates using the gross theory which is statistical in nature. In this model the shell structure of nucleons is not entirely accounted for and the theory considered the average values of transitions strength functions. Very soon it was realized that the microscopic theory should be used in order to get more decent results of computed nuclear $T_{1/2}$ values. In investigation of nuclear weak reaction properties the pn-QRPA theory has extensively employed in literature. In pn-QRPA a quasiparticle basis via pairing interaction is constructed first, and then the equation of RPA having schematic Gamow-Teller (GT) residual interaction is solved. Sorensen and Halbleib [29] developed this model by simplifying the usual RPA to calculate the relevant transitions. The pn-QRPA calculations were then extended to deformed nuclei by many authors [30–32]. Microscopic calculations of allowed weak-rates, from atomic number 6 to 114, were first performed by [33]. Later on this model was employed for the estimation of nuclear weak-decay properties of nuclei exist far away from the line of stability, in the β-decay [34] as well as electron capture (β^+) direction [35]. These calculations [34, 35] highlighted the strong and reliable results of this theoretical model specially when it is applied on unstable nuclei. This model was later employed for the studies of unique first-forbidden (U1F) transitions ($|\Delta J| = 2$) by [36, 37] under terrestrial conditions. These calculation demonstrated that for near-magic as well as near-stable nuclide, greater contribution to the total distribution arises from U1F strength [36]. For the first time, the authors in Ref. [38–40] have applied the pn-QRPA model, for the estimation of charge-changing reaction rates in stellar scenario. The same model was later modified to calculate U1F rates in stellar matter by Nabi and Stoica [41]. The QRPA model based on the Fayans energy functional was extended by Borzov to study the *r*-process mechanism [22]. In Ref. [22] it was shown that the FF transitions contribute largely to weak decay half-lives, mostly in case of nuclei containing closed protons and neutrons shells.

As per previous simulation results, weak interaction rates on *fp*-shell nuclei have significant influence on the stellar core vis-*à*-vis controlling the lepton content of stellar ingredients throughout the silicon shells burning stages of massive stars up to the presupernova stages. In this dissertation we report on the calculation of allowed GT as well as U1F ($|\Delta J| = 2$) charge-changing transition properties and the corresponding weak rates for astrophysical applications, by employing the deformed pn-QRPA nuclear model. Detail description of deformed pn-QRPA theory can be seen in the next chapter.

Chapter 2

Nuclear models

2.1 Introduction

Many of the concepts and techniques we learned in studying atoms and their quantum behavior, carry over to nuclear physics. Though, in some significant ways, they are quite different scenario:

i) We do not exactly know what the nucleon-nucleon potential is, but we do know that it possess a central, V(r), and non-central portion, V($\vec{x}$). That is the first problem.

ii) The force on one nucleon not only depends on the position of the other nucleons, but also on the distances between the other nucleons. These are called many-body forces. That is the second difficulty.

Several theoretical nuclear models have been developed to explain the nuclear properties till date, nevertheless, an all-inclusive nuclear model has not been realized yet. It should also be noted that unlike the case of atomic physics, maximum of these theoretical models describe well only partial features of the experimental data. Every model has associated pros and cons. Researchers are working hard to estimate, in a microscopic fashion, the ground- and excited-states charge-changing transition strength distributions. Measurement of Gamow-Teller (GT) functions itself is a challenging task. Due to involvement of hundreds of nuclei in stellar matter and also in order to incorporate finite-temperature effects, theoretical predictions of GT distributions continue to be the affordable choice. Because of the significant implications of the weak-rates in astrophysical scenario, they were widely studied using various nuclear models. Let first discuss briefly some of the experimental approaches used for the observation of nuclear structure properties.

2.2 Experimental techniques

2.2.1 Charge-exchange reactions

Nuclear reactions that involve the exchange of a neutron into a proton, or vice versa, are known as change-exchange (CE) reactions. The simplest examples are (n, p) and (p, n) reactions, but more difficult probes can also be used such as (t, ^{3}He) and (^{7}Li, ^{7}Be) reactions. The experimental extraction of GT strength functions in (p, n) and (n, p) directions at intermediate energies for pf-shell nuclide was performed in 1980s. These CE reactions alter the value of third component of isospin (T_z), and therefore comprise purely isovector interactions. The isoscalar interaction which governs (p, p$'$) reactions is not allowed [42]. This makes the (p, n) and (n, p) reactions ideal probes for studying the isovector portion of the nucleons interaction. At low energies ($\leq$100 MeV), the main aspect of the zero degree (p, n) reactions is the isobaric analog resonance (IAR) which is connected to Fermi β-decay. The IAR corresponds to transitions between analog states in parent and daughter nuclei. At energies greater than the 100 MeV, the $\sigma\tau$ part of the N-nucleus interaction is greater than the τ component and the GT resonance controls the small angle spectra. The charge-exchange (p, n) reactions has the benefit over β decay in the logic that the GT strength properties can be examined over a wide portion of excitation energy in the residual nucleus and is not restricted by Q value limitations. It is presumed that for (p, n) CE reactions at higher energies the reaction mechanism is direct, i.e., the whole spectrum containing peaks and continuum is a result of one step process. Secondly, the only nuclear states contributing to the (p, n) background at higher energies are spin-flip (ΔS=1, ΔT=1) states and the non-spin-flip states get strongly reduced [43]. However, the (n, p) reactions (denoted as isospin raising reaction) is sizably more challenging. In these CE reactions, the ^{7}Li(p, n)^{7}Be reaction is used in order to yield mono-energetic neutrons beams. Conversely, the ^{7}Li(p, n) reaction would also leave the ^{7}Be nuclide at high excitation lacking complicated unfolding techniques when producing final spectra. As neutron beams can only be created as a secondary beam, so the counting rates are typically low. Consequently, the energy resolution is often poor usually 1 MeV or worse. This poor resolution make analysis of the measured data challenging [44].

The (d, ^{2}He) CE reaction is another possible and potentially influential tool to examine the spin-isospin transition in the GT$^+$ direction [45, 46]. These charge-changing reactions have resolution of the order of 140-150 keV as compared to the resolution 1.3 MeV of (n, p) reaction [47].

The intermediate CE reactions (^{3}He, t) and (t, ^{3}He) are also used to probe the GT strength in GT$^-$ and GT$^+$directions, respectively, over a wide range of excitation energy. The energy resolutions of the (p, n) reactions are limited to ΔE = 200-300 keV because of the difficulty of getting good resolutions in neutron time-of-flight systems [48]. The resolution in this direction is drastically improved up to 50 keV in (^{3}He, t) reactions. As each excited level of parent nuclide has its own GT resonance in the daughter nuclide and all of these resonances must be taken into account. Such CE reactions do not have the ability to measure these excited state resonances, therefore one has to rely on the theoretical nuclear models to obtain such information's.

2.3 Theoretical approaches

The basic milestone to examine correctly the nuclear structure properties is a suitable understanding of the nucleus in shape of nucleon-nucleon interaction. At its most basic level, this needs a depiction of the nucleon in terms of quarks and gluons; at present it is believed that the proper theory is quantum chromodynamics (QCD). The nucleon-nucleon interaction can, in principle, be fully determined within QCD but our knowledge of QCD is still too limited to produce an acceptable interaction that can be employed consequently as an input for the explanation of a many-nucleon system. Another barrier arises because the free nucleon-nucleon interaction is, for nucleons in a nucleus, modified to consider the effect of surrounding nuclear medium. The explanation of a nucleus cannot consider directly the picture of nucleons in terms of quarks interaction. The nucleus of an atom is a complex system, many-body system bound by the strong nuclear interaction, and one simplifies the issue by employing the idea of effective forces.

2.3.1 Liquid-drop model

Nuclear models to explain the nuclear structure properties have been developed ever since the discovery of the nucleus by E. Rutherford in 1907. One of the first efforts to model the nuclear system was done by N. Bohr just after the neutron discovery inside the nucleus. Liquid-drop model, in nuclear physics, suggest that the nucleons act like the molecules in a drop of liquid. Theory of fission reaction was described by N. Bohr and Wheeler in 1939 on the basis of this model. Bohr explained that the compound nucleus formed is like the liquid drop and with small applied force it gets into vibrations. When a neutron having kinetic energy is captured by the nucleus, then this additional energy causes disturbance in the shape of the compound nucleus and it break [49]. The success of this average explanation of the nuclear system means that we employ it as guidance for much more advanced nuclear models. The various shapes of the liquid-drop model can only be helpful in prediction of averaged properties of many-nucleon systems.

2.3.2 Gross theory

Before describing the global microscopic nuclear models, let first explain the gross model that is statistical in nature. For large scale stellar applications, the GT strength distribution have typically been calculated empirically. For the first time, Burbidge et al. [12] employed, an energy independent strength function and allowed transition approximation to compute large scale beta decay rates for neutron rich nuclide. Later, Cameron [50] used statistical arguments to justify a smooth dependence of the beta strength function taken to be proportional to the level density of low-lying states in the daughter nuclide. Takahashi et al. [51] have used first parametric model (the so-called gross theory) to determine weak interaction rates which adds the single particle and statistical arguments in a phenomenological way. Within gross theory model the beta strength function of extreme single particle model is folded over the Fermi gas level density corrected for the pairing and shell effects. On top of that, the smooth contributions of the giant GT and spin-dipole resonances are also involved in a purely parametric way. A Gaussian or Lorentz shape is adopted for these resonances with energy, position, strength, and width fitted to the existing measured data, the sum rules, and lastly to the experimental half-lives values. The improved version of the gross theory [52,53] used an updated mass formula and offered an improved account for the shell and pairing effects and has been used for practical applications because of accurate reproduction of measured data and available extrapolation to unknown nuclide. The limitations of the model are intrinsically connected to it micro-statistical origin. As far as nuclear structure is concerned, gross theory has a serious deficiency of neglecting the cooperative effects due to the effective nucleon-nucleon interaction. Thus the independent (single) particle model miscalculates the beta decay energies and strengths of the high energy beta transitions and accordingly gross theory's parameterizations underestimate the weak decay half-lives.

2.3.3 The interacting boson model

A model which has led to very remarkable improvements is the interacting boson model (IBM) for even-even nuclide. In this nuclear model it is consider that the nucleus is comprised of bosons. As the pairing force between nucleons is very strong so this approximation is effective for low excitations energy in even-even nuclide having numerous valence nucleons. One aspect which makes IBM model so attractive for theoretical studies is, that it can be analytically solved for certain symmetry cases. These are called the limits of the IBM and they appear by demanding certain dynamical symmetries of the Hamiltonian, namely U(5), O(6) and SU(3) [54]. Each limit predicts selection rules for transitions between excited levels. For example, in the U(5) limit, all E_0 transitions are forbidden. Whereas, in the SU(3) limit, transitions between the ground state band and the β or γ band are forbidden. Only few nuclide depict very closely the features of one specific limit. The limits themselves are still beneficial for study of nuclear system because they give a new symmetry classifications for nuclear structure phenomena. There are many versions of IBM models, simplest of them is sd-IBM1. The IBM model extended for the explanation of odd-A nuclide is known as interacting boson fermion model. It presents an extra fermion to be coupled to the bosons. The probable levels of this single fermion are calculated from the corresponding shell model single particle levels. Details can be seen in Ref. [55].

2.3.4 The relativistic mean field (RMF) model

In the RMF model, a nucleus consists of nucleons and these nucleons interact with each other in such a way that various mesons and photons are exchanged between nucleons [56]. Scalar σ meson, vector ω meson and isovector ρ meson are conventionally taken into account in the RMF model. The σ meson is responsible for the attractive part of the interaction of nucleons while ω meson is related with the repulsive part. The photon and ρ meson play key roles for correct description of electromagnetic interaction and isospin-dependent effects in nuclei, respectively. Initially interactions of mesons among themselves were not considered but the simplest version of RMF model did not account for a correct description of incompressibility for nuclear matter. For this reason Boguta and Bodmer [57] proposed to include a non-linear self interaction of the σ mesons in the RMF model. This version of RMF model is commonly known as the non-linear RMF model and has been used for the last thirty years for prediction of various nuclear properties of finite nuclei. Different types of RMF models may be found in literature. In these models, non-linear self interaction of the ω and ρ mesons [58] as well as density dependent meson-nucleon couplings [59] were considered.

2.3.5 Shell model

If we look at the nucleon separation energies, it is observed that these values changes smoothly in most region of the nuclear chart. Whereas, at particular nucleon numbers, known as magic numbers, one can observe discrete jumps. These are the fingerprints of the nuclear shell structure. This behavior for magic nuclide can be explained in term of nuclear shell structure and its associated shell gaps. The nucleus is a many-body problem and as nucleons (neutrons and protons) are made of quarks, therefore the force between two nucleons is a residual interaction with complex structures. The dimension of this challenge, even if only two-nucleon interactions are considered, is too large to be determined even with modern day means. In shell model the complex interactions can be approximated by a spherical mean potential for one particle $H_0(i)$, generated by all nuclei, and separable residual interactions V_{res}, which make up for effects like pairing:

$$H = \sum_i H_0(i) + V_{res} \tag{2.1}$$

This model was very effective since its early days, as it was capable to define many phenomena for example, magic numbers, the 0^+ ground state spin of even-even nuclide and nuclear masses [54]. The nuclear shell model is called microscopic, opposed to macroscopic models like the geometric models which describe nuclear excitations as collective excitations like vibrations or rotations. However, shell model becomes unfeasible when going to systems which are well deformed or which have large nucleon numbers because of the dimension explosion.

2.3.6 Monte Carlo shell model

The nuclear shell model provides the benchmark for understanding several properties of nuclide. However, conventional shell model diagonalization for a complete one-major shell has been possible only up to the sd-shell, since the dimension of the Hamiltonian matrix becomes too large to be diagonalized for larger shells. In order to remove this trouble, the Monte Carlo shell model (MCSM) [60] has been suggested based on the Quantum Monte-Carlo diagonalization (QMCD) [61] procedure. Shell model Monte Carlo approach [62] was employed for the detailed computation of weak reaction rates on *fp*-shell nuclide. The major benefit of this technique is that it considers the nuclear temperature exactly. However, the shell model diagonalization may not be performed beyond the *fp*-shell nuclei, because of the huge dimension of the model spaces.

2.3.7 The pn-QRPA model

The first considerable attempt to measure the astrophysical weak-rates over broad range of stellar densities and temperature domain was done by [2]. They used the independent particle model (IPM) and employed the Brink-Axel hypothesis [63] in their calculation to estimate the excited state GT strength functions. They further incorporated measured data available at that time in their calculation to improve the reliability of the results. Later, the Fuller et al. work ([2]) was expanded for neutron-rich nuclei having $A > 60$ by Aufderheide and collaborators [64].

The large-scale shell model (LSSM) [65] and the pn-QRPA theories [39, 40] are the two most effective and widely employed models that are used for the accurate and microscopic computations of weak interaction processes. The deformed pn-QRPA theory is a reliable approach, microscopic in nature, to generate the Gamow-Teller transition functions. These strength functions establish a non-trivial and primary influence to the decay and capture processes amongst the iron mass range nuclide. For the first time, Nabi and his collaborators, have employed the theory of pn-QRPA, for the estimations of the astrophysical weak reaction rates on a broad range of densities and temperature domains for *sd*- [39] and *fp/fpg*-shell isotopes [40] in stellar environment. These global calculations were later improved, on case-to-case basis, with the usage of further proficient algorithms, refinement of model parameters, integration of experimental values and newest data from mass compilations(e.g. for detail see [66, 67]). The reliability and accuracy of pn-QRPA model calculations is explained in Ref. [40]. Recently six different QRPA models were considered, for the calculation of allowed charge-changing transitions in chromium nuclide. It was concluded in Ref. [68] that the deformed pn-QRPA model (used in this work) reproduced well the existing experimental data and possessed the decent predictive power to estimate the half-lives for unknown nuclei, compared to other five pn-QRPA models discussed in the study. It should be mentioned that the pn-QRPA model do not rely on the Brink-Axel hypothesis. The detailed description of pn-QRPA model can be seen in the next sections.

2.4 Formalism of pn-QRPA model

For doubly magic nuclei the approach of mean field works very well. When studying the applications of Hartree- Fock-Bogoliubov (HBF) theory for nuclei with open shell, pairing correlation is considered between the nucleons. The production of long range field as well as short range pairing forces are dealt and the estimation of ground level wave function for a nuclei is also done. Short range pairing forces act as a vacuum for Bogoliubov quasi-particle (q.p) and are of deterministic structures. Basically these q.p are generalized fermions. The linear combination of particle states and holes completely specifies these fermions therefore one can build the QRPA wave-function. To learn the collective states of a nuclei with open shell the QRPA provides a very convenient procedure.

The Hamiltonian for pn-QRPA model is defined as:

$$H^{pn-QRPA} = H^{SP} + V^{pairing} + V^{ph}_{GT} + V^{pp}_{GT}, \tag{2.2}$$

In the above equation the H^{SP} and $V^{pairing}$ denote the single particle Hamiltonian and pairing force, respectively. The particle-hole (ph) GT force is given by V_{GT}^{ph} and V_{GT}^{pp} is used for the particle-particle (pp) GT force. The pp force in quasi-particle transitions produce the phonon-correlation terms. To calculate the wave-function for single particle and their associated energies the Nilsson model is considered which has one big advantage of considering the nuclear deformation [69] (see Ref. [70] for detail study). The equation of transformation from spherically ($\{c_{jm}^+,\ c_{jm}\}$) nucleon basis, to axially symmetric deformed ($\{d_{m\alpha}^+, d_{m\alpha}\}$) basis, is $d_{m\alpha}^+ = \sum_j D_j^{m\alpha} c_{jm}^+$. Where d^+ represents the particle creation operator using deformation basis, whereas in spherical basis c^+ represents the creation operator, angular momentum is specified as j with its z-component m. Transformation matrices are shown as $D_j^{m\alpha}$. These matrices represent the set of Nilsson eigen functions which are achieved through the diagonalization of Nilsson Hamiltonian. Apart from m which locates the Nilsson eigen-states, the α stands for additional quantum number [69].

In Nilsson basis the calculation of BCS is done individually for both neutron and proton systems. Pairing phenomena is taken into account through BCS theory where 'G' represent the interaction strength (G_n is used for neutron and G_p for protons) is considered.

$$V^{pair} = -G \sum_{jmj'm'} (-1)^{l+j-m} c_{jm}^+ c_{j-m}^+ (-1)^{l'+j'-m'} c_{j'-m'} c_{j'm'}, \tag{2.3}$$

here in the summation $m, m' > 0$ is considered and l show the the orbital angular momenta. BCS model is employed for the prediction of q.p energies ($\epsilon_{m\alpha}$).

The q.p basis is determined as:

$$a_{m\alpha}^+ = u_{m\alpha} d_{m\alpha}^+ - v_{m\alpha} d_{\bar{m}\alpha}, \tag{2.4}$$

$$a_{\bar{m}\alpha}^+ = u_{m\alpha} d_{\bar{m}\alpha}^+ - v_{m\alpha} d_{m\alpha}. \tag{2.5}$$

The time-reversed state of m is depicted by $\bar{m}$ and annihilation of creation operator is specified by $d_{m\alpha}^+(d_{m\alpha})$ using Nilsson basis. On the other hand same operators for q.p is denoted by $a^+(a)$ which is to be introduced in the RPA equation. Here u and v represent the occupation amplitudes fulfill the equation $u^2 + v^2 = 1$. For basis of nucleon the phase convention of Condon and Shortley is taken under consideration [71] whereas for Nilsson basis and so the q.p one can use BCS phases [72]. A comparison of nucleons scattering is shown in Fig. 2.1. This distribution is found between all those orbits which have or do not have pairing correlations.

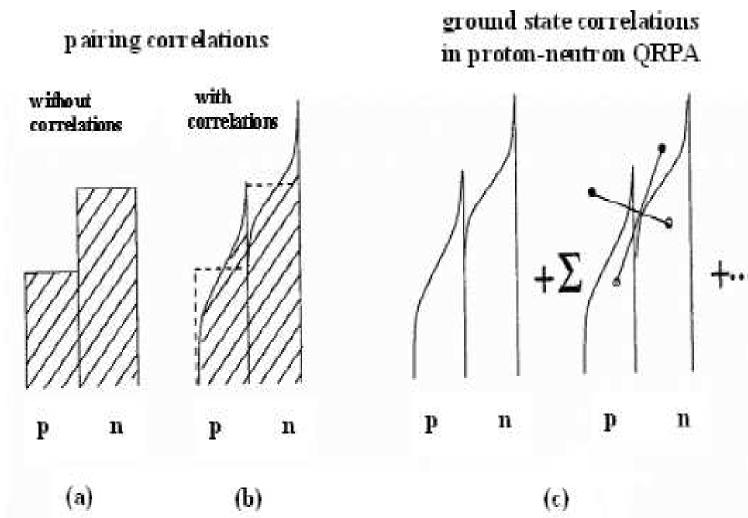

Figure 2.1: Distributions of nucleons among single particle orbits in a nucleus; **(a)** without pairing correlations (the simplest shell model), **(b)** with pairing correlations. **(c)** Ground state wave function in the proton-neutron quasi-particle RPA. The line connecting circles, which denotes quasi-particles, indicates angular momentum coupling of a proton-neutron pair. Both pairs have the same spin-parity J^{π} [73].

When there is no correlation (Fig. 2.1a), the lower shells are seen to be filled completely whereas the higher orbits are found empty. One orbit is however allowed to be partially filled which is nearest to the Fermi energy. Fig. 2.1b also depicts that whenever the interaction of pairing is considered the distribution of nucleon smears out. All of the nucleons are found paired for $J^{\pi}=0^{+}$. The wave function of ground level is shown in Fig. 1.4c. The main ingredient of the BCS ground level without q.p is depicted in the Fig. 2.1b.

In pn-QRPA model, the creation of phonon plays a key role in describing the charge-changing transitions. The operators used for phonon creation are denoted as:

$$A^{+}_{\omega}(\mu) = \sum_{pm}(X^{pm}_{\omega}(\mu)a^{+}_{p}a^{+}_{\bar{n}} - Y^{pm}_{\omega}(\mu)a^{+}_{n}a^{+}_{\bar{p}}), \tag{2.6}$$

The n and p in the subscript are used to indicate $m_n\alpha_n$ and $m_p\alpha_p$ respectively. In RPA equation the phonon excitation energy (ω) is obtained as an eigen-value. In Eq. 2.6 the sum run over the total proton-neutron pairs, having projection μ=m_p-m_n=-1,0,1. Third component of angular momentum is denoted here by $m_{p(n)}$. The creation operator used for the q.p state of proton and neutron are denoted as $a^{+}_{p(n)}$. In pn-QRPA theory the ground level is taken as vacuum for QRPA phonon, A$_{\omega}(\mu)|QRPA\rangle$. The famous RPA equation in matrix form is specified as:

$$\begin{pmatrix} A & B \\ -B^{*} & -A^{*} \end{pmatrix}\begin{pmatrix} X \\ Y \end{pmatrix} = \omega\begin{pmatrix} X \\ Y \end{pmatrix}, \tag{2.7}$$

here the excitation energy ω, is the eigenvalue of the QRPA state, X is the forward-going amplitude and Y represent the backward-going amplitude. The terms A and B are the matrix elements which are specified as:

$$\begin{aligned} A_{pn,p'n'} = \delta(pn,p'n')(\epsilon_p+\epsilon_n) + V^{pp}_{pn,p'n'}(u_pu_nu_{p'}u_{n'} + v_pv_nv_{p'}v_{n'}) \\ +V^{ph}_{pn',p'n'}(u_pv_nu_{p'}v_{n'} + v_pu_nv_{p'}u_{n'}), \end{aligned} \tag{2.8}$$

$$B_{pn,p'n'} = V^{pp}_{pn,p'n'}(u_pu_nv_{p'}v_{n'} + v_pv_nu_{p'}u'_{n}) - V^{ph}_{pn,p'n'}(u_pv_nv_{p'}u_{n'} + v_pu_nu_{p'}v_{n'}). \tag{2.9}$$

where the $\varepsilon_p(\varepsilon_n)$ indicates the quasi-particle energies of levels related to proton or neutron. Occupation/unoccupation amplitude is shown as v_k/u_k and are known to be calculated through BCS. The point to note here is that the backward-going amplitude Y is responsible for the correlations in ground level. In order to derive QRPA matrix only a small correction is needed in the correlation of ground state. It is prominent that, $|Y| << |X|$ did not show that the ground level correlations are of no importance. Because the product of uvY and

$u'v'X$ should be taken into account for calculation of beta matrix elements. However, as a particular problem, in β^+ weak reaction the product uv can be larger than $u'v'$. Details of this discussion can be found in [73]. The RPA eigenvalue equation can be solved by taking different projection values as $\mu = -1, 0,$ and $+1$. For μ equal to -1 and 1, the eigenvalue spectra are same, however two fold degeneracy is shown for $\mu = 0$, because of axial symmetry employed in the Nilsson potential.

The residual interactions among proton-neutron appear as *ph* and *pp* interactions, represented as χ and κ interaction constants, correspondingly. The χ and κ were selected in an optimal style. The κ has minor role in electron emission (β^-) interaction thus it can be neglected [32, 74–76], however in positron emission (β^+) this has significant role [77, 78].

The ph GT force is defined as

$$V_{GT}^{ph} = 2\chi \sum_{\mu} (-1)^{\mu} Y_{\mu} Y_{-\mu}^{+}, \tag{2.10}$$

here

$$Y_{\mu} = \sum_{j_p m_p j_n m_n} \langle j_p m_p | \, t_- \sigma_{\mu} \, | j_n m_n \rangle \, c_{j_p m_p}^{+} c_{j_n m_n}, \tag{2.11}$$

and the pp force is defined as

$$V_{GT}^{pp} = -2\kappa \sum_{\mu} (-1)^{\mu} P_{\mu}^{+} P_{-\mu}, \tag{2.12}$$

where

$$P_{\mu}^{+} = \sum_{j_p m_p j_n m_n} \langle j_n m_n | \, (t_- \sigma_{\mu})^{+} \, | j_p m_p \rangle \, (-1)^{l_n + j_n - m_n} c_{j_p m_p}^{+} c_{j_n - m_n}^{+}. \tag{2.13}$$

The values of χ and κ are considered to be positive in units of MeV. The negative sign in Eq. 2.12 indicate that of the *pp* force (V^{pp}) force is attractive, however *ph* force is considered repulsive. Thus in RPA equation (Eq. 2.7), separate matrix elements are taken for these forces and are specified as

$$V_{pn,p'n'}^{pp} = -2\kappa f_{pn}(\mu) f_{p'n'}(\mu), \tag{2.14}$$

$$V_{pn,p'n'}^{ph} = +2\chi f_{pn}(\mu) f_{p'n'}(\mu), \tag{2.15}$$

where

$$f_{pn}(\mu) = \sum_{j_p j_n} D_{j_p}^{m_p \alpha_p} D_{j_n}^{m_n \alpha_n} \left\langle j_p m_p \right| t_- \sigma_\mu \left| j_n m_n \right\rangle . \tag{2.16}$$

RPA equation (Eq. 2.7) in more explicit form, can be specified as

$$X_\omega^{pn} = \frac{1}{\omega - \epsilon_{pn}} [2\chi(q_{pn} Z_\omega^- + \tilde{q_{pn}} Z_\omega^+) - 2\kappa(q_{pn}^U Z_\omega^{--} + q_{pn}^V Z_\omega^{++})], \tag{2.17}$$

$$Y_\omega^{pn} = \frac{1}{\omega + \epsilon_{pn}} [2\chi(q_{pn} Z_\omega^+ + \tilde{q_{pn}} Z_\omega^-) + 2\kappa(q_{pn}^U Z_\omega^{++} + q_{pn}^V Z_\omega^{--})], \tag{2.18}$$

where $\epsilon_{pn} = \epsilon_p + \epsilon_n, \quad q_{pn} = f_{pn} u_p \upsilon_n, \quad q_{pn}^U = f_{pn} u_p u_n, \quad \tilde{q}_{pn} = f_{pn} \upsilon_p u_n, \quad q_{pn}^V = f_{pn} \upsilon_p \upsilon_n$

$$Z_\omega^+ = \sum_{pn} (X_\omega^{pn} \tilde{q}_{pn} - Y_\omega^{pn} q_{pn}), \tag{2.19}$$

$$Z_\omega^- = \sum_{pn} (X_\omega^{pn} q_{pn} - Y_\omega^{pn} \tilde{q}_{pn}), \tag{2.20}$$

$$Z_\omega^{++} = \sum_{pn} (X_\omega^{pn} q_{pn}^V + Y_\omega^{pn} q_{pn}^U), \tag{2.21}$$

$$Z_\omega^{--} = \sum_{pn} (X_\omega^{pn} q_{pn}^U + Y_\omega^{pn} q_{pn}^V). \tag{2.22}$$

Insertion of Eqs. (2.17) and (2.18), in Eqs.(2.20- 2.21), leads to elimination of X_ω^{pn} and Y_ω^{pn} which clearly rely on the q.p pairs of protons and neutrons individually. Therefore, a group of equations are obtained for each Z^+, Z^-, Z^{--}, and Z^{++}, which are similar to the Eq. (2.7),

$$Mz = 0, \tag{2.23}$$

where

$$M = \begin{bmatrix} \chi M_1 - 1 & \chi M_0 & -\kappa M_5 & -\kappa M_7 \\ \chi M_0 & \chi M_2 - 1 & -\kappa M_8 & -\kappa M_6 \\ \chi M_5 & \chi M_8 & -\kappa M_3 - 1 & -\kappa M_0 \\ \chi M_7 & \chi M_6 & -\kappa M_0 & -\kappa M_4 - 1 \end{bmatrix}, \tag{2.24}$$

$$z = \begin{bmatrix} Z_\omega^- \\ Z_\omega^+ \\ Z_\omega^{--} \\ Z_\omega^{++} \end{bmatrix}, \tag{2.25}$$

and

$$\begin{aligned}
M_0 &= 2\sum_{pn}\left(\frac{q_{pn}\tilde{q_{pn}}}{\omega-\epsilon_{pn}} - \frac{q_{pn}\tilde{q_{pn}}}{\omega+\epsilon_{pn}}\right) \\
&= 2\sum_{pn}\left(\frac{q_{pn}^U q_{pn}^V}{\omega-\epsilon_{pn}} - \frac{q_{pn}^U q_{pn}^V}{\omega+\epsilon_{pn}}\right), \\
M_1 &= 2\sum_{pn}\left(\frac{q_{pn}^2}{\omega-\epsilon_{pn}} - \frac{\tilde{q}_{pn}^2}{\omega+\epsilon_{pn}}\right), \\
M_2 &= 2\sum_{pn}\left(\frac{\tilde{q}_{pn}^2}{\omega-\epsilon_{pn}} - \frac{q_{pn}^2}{\omega+\epsilon_{pn}}\right), \\
M_3 &= 2\sum_{pn}\left(\frac{q_{pn}^{U^2}}{\omega-\epsilon_{pn}} - \frac{q_{pn}^{V^2}}{\omega+\epsilon_{pn}}\right), \\
M_4 &= 2\sum_{pn}\left(\frac{q_{pn}^{V^2}}{\omega-\epsilon_{pn}} - \frac{q_{pn}^{U^2}}{\omega+\epsilon_{pn}}\right), \\
M_5 &= 2\sum_{pn}\left(\frac{q_{pn}q_{pn}^U}{\omega-\epsilon_{pn}} - \frac{\tilde{q}_{pn}q_{pn}^V}{\omega+\epsilon_{pn}}\right), \\
M_6 &= 2\sum_{pn}\left(\frac{\tilde{q}_{pn}q_{pn}^V}{\omega-\epsilon_{pn}} - \frac{q_{pn}q_{pn}^U}{\omega+\epsilon_{pn}}\right), \\
M_7 &= 2\sum_{pn}\left(\frac{q_{pn}q_{pn}^V}{\omega-\epsilon_{pn}} - \frac{\tilde{q}_{pn}q_{pn}^U}{\omega+\epsilon_{pn}}\right), \\
M_8 &= 2\sum_{pn}\left(\frac{\tilde{q}_{pn}q_{pn}^U}{\omega-\epsilon_{pn}} - \frac{q_{pn}q_{pn}^V}{\omega+\epsilon_{pn}}\right).
\end{aligned} \tag{2.26}$$

Eq. 2.23 solution can be achieved by considering,

$$|M| = 0, \tag{2.27}$$

by concerning the M_k ($k = 0 - 8$) as functions of the energy (ω). For $\kappa \neq 0$, Eq. 2.27 is interpreted to second order equation in M_k's and with the addition of κ values it becomes fourth order equation. Solution of these equations in detailed can be found in [79]. For each ω value, the GT charge-changing transition amplitudes to RPA eigenfunctions, are determined as given below. N_ω^-, N_ω^+, N_ω^{--}, and N_ω^{++} are first four co-determinants of M that are evaluated at ω. The values of these co-determinants are found by expanding determinant M,

$$detM = \big(\chi M_1 - 1\big)N^- + \chi M_0 N^+ - \kappa M_5 N^{--} - \kappa M_7 N^{++}. \tag{2.28}$$

Then, Z_ω's ratios are evaluated as

$$\frac{Z_\omega^-}{N_\omega^-} = \frac{Z_\omega^+}{N_\omega^+} = \frac{Z_\omega^{--}}{N_\omega^{--}} = \frac{Z_\omega^{++}}{N_\omega^{++}}, \tag{2.29}$$

the absolute values can be determined, by using the normalization condition,

$$\sum_{pn}[\big(X_\omega^{pn}\big)^2 - \big(Y_\omega^{pn}\big)^2] = 1, \tag{2.30}$$

by inserting the values of Z_ω's in equations (2.17) and (2.18). The amplitudes of the GT transitions strength from the QRPA ground state, $|-\rangle$ (QRPA vacuum; $A_\omega(\mu)\,|-\rangle = 0$) to one phonon states $|\omega,\mu\rangle = A_\omega^+(\mu)\,|-\rangle$ are easily determined as:

$$\langle\omega,\mu|\, t_\pm\sigma(\mu)\,|-\rangle = \mp Z_\omega^\pm. \tag{2.31}$$

The energies of excitation for one phonon states is specified as $\omega - (\epsilon_p + \epsilon_n)$, where ϵ_n (ϵ_p) represent the neutron (proton) single q.p states energies.

2.5 Quasi-particle transitions

RPA was formulated for excitations of even-even nuclide from the ground level ($J^\pi = 0^+$). For the parent nuclide consist of odd number of protons and neutrons, the ground level can be defined as a one quasi-particle state, in which the odd q.p fills the single q.p shell with the lowest energy. In these odd-odd nuclei two kinds of transitions may exist. One is the phonon excitations and the other is quasi-particle transitions [29]. The phonon-correlated one q.p levels are specified as;

$$\begin{aligned}|p_{corr}\rangle &= a_p^+ \left|-\right\rangle + \sum_{n,\omega} a_n^+ A_\omega^+(\mu) \left|-\right\rangle \left\langle-\right| [a_n^+ A_\omega^+(\mu)]^+ H_{31} a_p^+ \left|-\right\rangle E_p(n,\omega) \\ |n_{corr}\rangle &= a_n^+ \left|-\right\rangle + \sum_{p,\omega} a_p^+ A_\omega^+(-\mu) \left|-\right\rangle \left\langle-\right| [a_p^+ A_\omega^+(-\mu)]^+ H_{31} a_n^+ \left|-\right\rangle E_n(p,\omega),\end{aligned} \tag{2.32}$$

and

$$E_a(b,\omega) = \frac{1}{\epsilon_a - \epsilon_b - \omega}. \tag{2.33}$$

Eq. 2.32 consist of two parts, first part depicts the neutron(proton) quasi-particle level, however the second part illustrates the admixture of correlated RPA phonons with phonon quasi-particle coupling Hamiltonian H_{31}, chosen from the *ph* and *pp* separable forces by using the Bogoliubov transformation [80]. The summation in the Eq. 2.32 run over all the levels of phonon and neutron(proton) q.p levels that fulfill the $m_p - m_n = \mu$ and $\pi_p.\pi_n = 1$. The derivation of the quasi-particle transition amplitudes for correlated states are shown in [80]. The final expression for the charge-changing GT transitions amplitudes are represented as:

$$\begin{aligned}\langle p_{corr}| t_-\sigma_\mu |n_{corr}\rangle &= q_{pn}^U + 2\chi[q_{pn}^U \sum_\omega (Z_\omega^{-2} E_p(n,\omega) + Z_\omega^{+2} E_n(p,\omega)) \\ -q_{pn}^V \sum_\omega Z_\omega^- Z_\omega^+ (E_p(n,\omega) + E_n(p,\omega))] &+ 2\kappa[q_{pn} \sum_\omega (Z_\omega^- Z_\omega^{--} E_p(n,\omega) - Z_\omega^+ Z_\omega^{++} E_n(p,\omega)) \\ &- \tilde{q}_{pn} \sum_\omega Z_\omega^- Z_\omega^{++} (E_p(n,\omega) - Z_\omega^+ Z_\omega^{++} E_n(p,\omega))],\end{aligned} \tag{2.34}$$

$$\begin{aligned}\langle p_{corr}| t_+\sigma_\mu |n_{corr}\rangle &= q_{pn}^V + 2\chi[q_{pn}^V \sum_\omega (Z_\omega^{+2} E_p(n,\omega) + Z_\omega^{-2} E_n(p,\omega)) \\ &-q_{pn}^U \sum_\omega Z_\omega^- Z_\omega^+ (E_p(n,\omega) + E_n(p,\omega))] + 2\kappa[\tilde{q}_{pn} \sum_\omega (Z_\omega^+ Z_\omega^{++} E_p(n,\omega) \\ &-Z_\omega^- Z_\omega^{--} E_n(p,\omega)) - q_{pn} \sum_\omega Z_\omega^+ Z_\omega^{--} E_p(n,\omega)) - Z_\omega^- Z_\omega^{++} E_n(p,\omega))],\end{aligned} \tag{2.35}$$

and

$$\langle n_{corr}| t_\pm\sigma_{-\mu} |p_{corr}\rangle = (-1)^\mu \langle p_{corr}| t_\mp\sigma_\mu |n_{corr}\rangle. \tag{2.36}$$

The q.p and phonons transitions for parent nuclide having odd-neutrons are depicted in figure (2.2a).

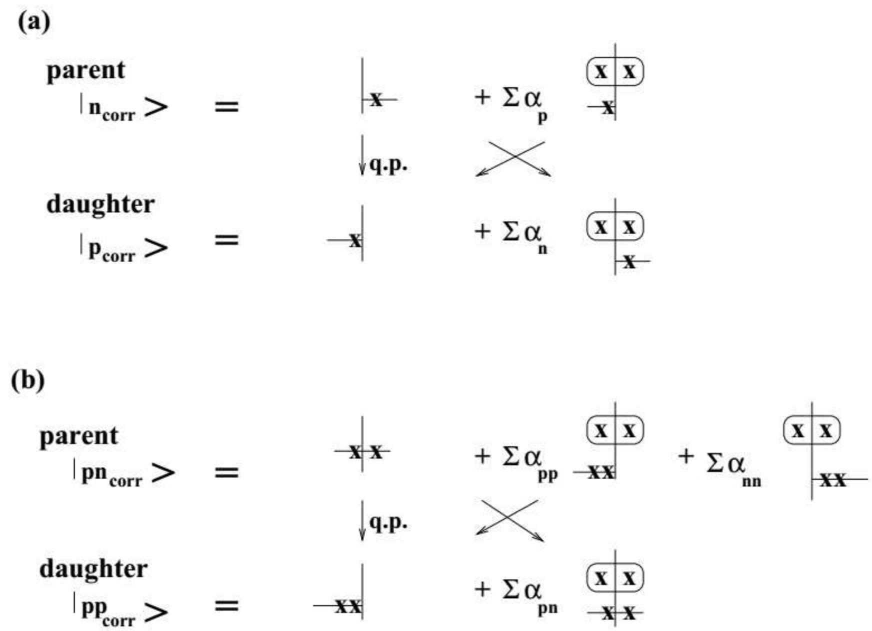

Figure 2.2: Examples of quasi-particle and QRPA phonon transitions for a parent nucleus with an odd nucleon. Quasi-particles are denoted by a cross and phonons by an oval with two crosses in it. (a) Transitions from an even-proton odd-neutron parent nucleus to the odd-proton even-neutron daughter nucleus. (b) Transitions from the ground state of an odd-odd nucleus, which is described by a proton-neutron quasi-particle pair state, to a two-proton quasi-particle state in the even-even daughter nucleus [73].

The idea of quasi-particle transitions having 1st order correlation can be extended for the odd-odd parent nuclide [75, 80]. Schematically it is represented in the Fig.(2.2b). The ground level is considered to be a neutron-proton q.p pair level of lowest energy. The GT transitions of the q.p proceed to two-neutron or two-proton q.p levels in the daughter nuclide having even number of protons and neutrons. The two quasi-particle levels are generated via phonon correlations in first order perturbation,

$$|pn_{corr}\rangle = a_p^+ a_n^+ |-\rangle + \frac{1}{2}\sum_{p_1' p_2' \omega} a_{p_1'}^+ a_{p_2'}^+ A_\omega^+(-\mu) |-\rangle \langle -| [a_{p_1'}^+ a_{p_2'}^+ A_\omega^+(-\mu)]^+$$
$$H_{31} a_p^+ a_n^+ |-\rangle E_{pn}(p_1' p_2', \omega) + \frac{1}{2}\sum_{n_1' n_2' \omega} a_{n_1'}^+ a_{n_2'}^+ A_\omega^+(\mu) |-\rangle \langle -| [a_{n_1'}^+ a_{n_2'}^+ A_\omega^+(\mu)]^+ \tag{2.37}$$
$$H_{31} a_p^+ a_n^+ |-\rangle E_{pn}(n_1' n_2', \omega),$$

$$|p_1 p_{2corr}\rangle = a_{p1}^+ a_{p2}^+ |-\rangle + \sum_{p' n' \omega} a_{p'}^+ a_{n'}^+ A_\omega^+(\mu) |-\rangle \langle -| [a_{p'}^+ a_{n'}^+ A_\omega^+(\mu)]^+ \tag{2.38}$$
$$H_{31} a_{p1}^+ a_{p2}^+ |-\rangle E_{p1p2}(p' n', \omega),$$

$$|n_1 n_{2corr}\rangle = a_{n1}^+ a_{n2}^+ |-\rangle + \sum_{p' n' \omega} a_{p'}^+ a_{n'}^+ A_\omega^+(-\mu) |-\rangle \langle -| [a_{p'}^+ a_{n'}^+ A_\omega^+(-\mu)]^+ \tag{2.39}$$
$$H_{31} a_{n1}^+ a_{n2}^+ |-\rangle E_{n1n2}(p' n', \omega),$$

where

$$E_{ab}(cd, \omega) = \frac{1}{(\epsilon_a + \epsilon_b) - (\epsilon_c + \epsilon_d + \omega)}. \tag{2.40}$$

The charge-changing GT strength amplitudes among these levels are reduced to those of one q.p levels,

$$\langle p_1 p_{2corr}| t_\pm \sigma_\mu |pn_{corr}\rangle = \delta(p_1, p) \langle p_{2corr}| t_\pm \sigma_\mu |n_{corr}\rangle - \delta(p_2, p) \tag{2.41}$$
$$\langle p_{1corr}| t_\pm \sigma_\mu |n_{corr}\rangle ,$$

$$\langle n_1 n_{2corr}| t_\pm \sigma_{-\mu} |pn_{corr}\rangle = \delta(n_2, n) \langle n_{1corr}| t_\pm \sigma_{-\mu} |p_{corr}\rangle - \delta(n_1, n) \tag{2.42}$$
$$\langle n_{2corr}| t_\pm \sigma_{-\mu} |p_{corr}\rangle ,$$

by ignoring terms of second order in the correlated phonons, the amplitudes of q.p transitions are represented by the Eqs.(2.34-2.36). For parent nuclide consist of odd protons and odd neutrons, the phonon excitation of QRPA are also probable, and then the q.p pair remains in the similar shell of single quasi-particle as a spectators.

Due to the perturbative behavior of the phonon correlations, an unreasonable increase may occur in the quasi-particle transition strength, when the denominator of Eq. 2.33 become vanish. This is avoided by adding an imaginary quantity to the denominator.

$$E_a(b,\omega) = \frac{\epsilon_a - \epsilon_b - \omega}{(\epsilon_a - \epsilon_b - \omega)^2 + \Gamma^2}, \tag{2.43}$$

this shifts the pole from the real axis of the energy variable ω.

2.6 Extended model of pn-QRPA (transitions from excited states)

As the strength of GT is scattered over a broad range of initial and final states therefore the understanding of final and initial structure of nuclear level is very important. An extension in pn-QRPA model is essential for an in depth study of weak interaction rates calculation. The excited levels of parent nuclide can be developed as the phonon correlated multi-q.p levels.

By one neutron and/or proton excitations, the low lying excited levels of a nuclide can be obtained. In q.p description, they can be explained by adding two-neutrons (two-protons) quasi-particles to the ground level [79]. The transition amplitudes among the multi quasi-particle levels could be expressed in form of single quasi-particle levels by using the procedure noted below.

2.6.1 Even-even nuclide

In case of even-even nuclide the excited levels are expressed as two-proton q.p levels and two-neutron q.p levels shown by Eq. 2.38 and 2.39, respectively. In the odd-odd daughter nuclide transitions from these initial levels to final proton-neutron quasi-particle pair levels are only possible. The amplitudes for transitions and their conversion to correlated (c) one quasi-particle level is denoted as:

$$\langle p^f n_c^f |\, t_\pm \sigma_{-\mu} \,| p_1^i p_{2c}^i \rangle = -\delta(p^f, p_2^i) \langle n_c^f |\, t_\pm \sigma_{-\mu} \,| p_{1c}^i \rangle + \delta(p^f, p_1^i) \langle n_c^f |\, t_\pm \sigma_{-\mu} \,| p_{2c}^i \rangle \,, \tag{2.44}$$

$$\langle p^f n_c^f |\, t_\pm \sigma_{\mu} \,| n_1^i n_{2c}^i \rangle = +\delta(n^f, n_2^i) \langle p_c^f |\, t_\pm \sigma_{\mu} \,| n_{1c}^i \rangle - \delta(n^f, n_1^i) \langle p_c^f |\, t_\pm \sigma_{\mu} \,| n_{2c}^i \rangle \,, \tag{2.45}$$

where $\mu = -1, 0, 1$ represent the spherical components of spin operator.

2.6.2 Odd-even nuclide

When a nuclide have odd number of protons and even number of neutrons, low-lying levels are obtained, when the quasi-particles are lifted from lowest energy orbits to higher orbits. There states are expressed by 1p-2n states or 3p states, related to a proton or neutron excitation.

$$\begin{aligned}|p_1p_2p_{3corr}\rangle = a^+_{p_1}a^+_{p_2}a^+_{p_3}\,|-\rangle + \frac{1}{2}\sum_{p'_1p'_2n'\omega} a^+_{p'_1}a^+_{p'_2}a^+_{n'}A^+_\omega(\mu)\,|-\rangle \\ \langle -|\,[a^+_{p'_1}a^+_{p'_2}a^+_{n'}A^+_\omega(\mu)]^+H_{31}a^+_{p_1}a^+_{p_2}a^+_{p3}\,|-\rangle\, E_{p_1p_2p_3}(p'_1p'_2n',\omega),\end{aligned} \tag{2.46}$$

$$\begin{aligned}|p_1n_1n_{2corr}\rangle = a^+_{p_1}a^+_{n_1}a^+_{n_2}\,|-\rangle + \frac{1}{2}\sum_{p'_1p'_2n'\omega} a^+_{p'_1}a^+_{p'_2}a^+_{n'}A^+_\omega(-\mu)\,|-\rangle \\ \langle -|\,[a^+_{p'_1}a^+_{p'_2}a^+_{n'}A^+_\omega(-\mu)]^+H_{31}a^+_{p_1}a^+_{n_1}a^+_{n_2}\,|-\rangle\, E_{p_1n_1n_1}(p'_1p'_2n',\omega) + \frac{1}{6} \\ \sum_{n'_1n'_2n'_3\omega} a^+_{n'_1}a^+_{n'_2}a^+_{n'_3}A^+_\omega(\mu)\,|-\rangle\,\langle -|\,[a^+_{n'_1}a^+_{n'_2}a^+_{n'_3}A^+_\omega(\mu)]^+ \\ H_{31}a^+_{p_1}a^+_{n_1}a^+_{n_2}\,|-\rangle\, E_{p_1n_1n_2}(n'_1n'_2n'_3,\omega),\end{aligned} \tag{2.47}$$

having the energy denominators of first order perturbation.

$$E_{abc}(def,\omega) = \frac{1}{(\epsilon_a+\epsilon_b+\epsilon_c)-(\epsilon_d+\epsilon_e+\epsilon_f+\omega)}. \tag{2.48}$$

The three q.p levels for nuclide consist of even protons and odd neutrons are obtained from Eqs. (2.46 and 2.47) by the exchange of $n \longleftrightarrow p$ levels as well as $A^+_\omega(-\mu) \longleftrightarrow A^+_\omega(\mu)$. The excited levels for a nucleus having odd number of neutrons and protons number, are established as

(1) when the odd neutrons from the ground level are lifted up to excited levels (one q.p state),

(2) 3n levels, relating to neutron excitation or,

(3) 1n and 2n levels, associated to proton excitation.

The equations that denote the transitions of multi-q.p and their conversion to correlated

(c) one-q.p levels are shown below:

$$\begin{aligned}
\langle p_1^f n_1^f n_{2c}^f | \, t_{\pm}\sigma_{\mu} \, | n_1^i n_2^i n_{3c}^i \rangle = {} & \delta(n_1^f, n_2^i)\delta(n_2^f, n_3^i) \, \langle p_{1c}^f | \, t_{\pm}\sigma_{\mu} \, | n_{1c}^i \rangle \\
& - \delta(n_1^f, n_1^i)\delta(n_2^f, n_3^i) \, \langle p_{1c}^f | \, t_{\pm}\sigma_{\mu} \, | n_{2c}^i \rangle \\
& + \delta(n_1^f, n_1^i)\delta(n_2^f, n_2^i) \, \langle p_{1c}^f | \, t_{\pm}\sigma_{\mu} \, | 3_{3c}^i \rangle \, ,
\end{aligned} \tag{2.49}$$

$$\begin{aligned}
\langle p_1^f n_1^f n_{2c}^f | \, t_{\pm}\sigma_{-\mu} \, | p_1^i p_2^i n_{1c}^i \rangle = {} & \delta(p_1^f, p_2^i)[\delta(n_1^f, n_1^i) \, \langle n_{2c}^f | \, t_{\pm}\sigma_{-\mu} \, | p_{1c}^i \rangle \\
& - \delta(n_2^f, n_1^i) \, \langle n_{1c}^f | \, t_{\pm}\sigma_{-\mu} \, | p_{1c}^i \rangle] \\
& - \delta(p_1^f, p_1^i)[\delta(n_1^f, n_1^i) \, \langle n_{2c}^f | \, t_{\pm}\sigma_{-\mu} \, | p_{2c}^i \rangle \\
& - \delta(n_2^f, n_1^i) \, \langle n_{1c}^f | \, t_{\pm}\sigma_{-\mu} \, | p_{2c}^i \rangle],
\end{aligned} \tag{2.50}$$

$$\begin{aligned}
\langle p_1^f p_2^f p_{3c}^f | \, t_{\pm}\sigma_{\mu} \, | p_1^i p_2^i n_{1c}^i \rangle = {} & \delta(p_2^f, p_1^i)\delta(p_3^f, p_2^i) \, \langle p_{1c}^f | \, t_{\pm}\sigma_{\mu} \, | n_{1c}^i \rangle \\
& - \delta(p_1^f, p_1^i)\delta(p_3^f, p_2^i) \, \langle p_{2c}^f | \, t_{\pm}\sigma_{\mu} \, | n_{1c}^i \rangle \\
& + \delta(p_1^f, p_1^i)\delta(p_2^f, p_2^i) \, \langle p_{3c}^f | \, t_{\pm}\sigma_{\mu} \, | n_{1c}^i \rangle \, .
\end{aligned} \tag{2.51}$$

In same fashion, the construction of excited levels for nuclei having odd number of protons and even number of neutrons, are given as;

(1) when the odd protons from the ground level are lifted up to excited levels (one q.p state),

(2) 3n levels, relating to neutron excitation or,

(3) 1p and 2n levels, related to excitation of neutron.

The equations that denote the transitions of multi-q.p and their conversion to correlated (c) one-q.p levels are specified below:

$$\begin{aligned}
\langle p_1^f p_2^f n_{1c}^f | \, t_{\pm}\sigma_{-\mu} \, | p_1^i p_2^i p_{3c}^i \rangle = {} & \delta(p_1^f, p_2^i)\delta(p_2^f, p_3^i) \, \langle n_{1c}^f | \, t_{\pm}\sigma_{-\mu} \, | p_{1c}^i \rangle \\
& - \delta(p_1^f, p_1^i)\delta(p_2^f, p_3^i) \, \langle n_{1c}^f | \, t_{\pm}\sigma_{-\mu} \, | p_{2c}^i \rangle \\
& + \delta(p_1^f, p_1^i)\delta(p_2^f, p_2^i) \, \langle n_{1c}^f | \, t_{\pm}\sigma_{-\mu} \, | p_{3c}^i \rangle \, ,
\end{aligned} \tag{2.52}$$

$$\begin{aligned}\langle p_1^f p_2^f n_{1c}^f | \, t_\pm \sigma_\mu \, | p_1^i n_1^i n_{2c}^i \rangle = \delta(n_1^f, n_2^i)[\delta(p_1^f, p_1^i) \, \langle p_{2c}^f | \, t_\pm \sigma_\mu \, | n_{1c}^i \rangle \\ -\delta(p_2^f, p_1^i) \, \langle p_{1c}^f | \, t_\pm \sigma_\mu \, | n_{1c}^i \rangle] \\ -\delta(n_1^f, n_1^i)[\delta(p_1^f, p_1^i) \, \langle p_{2c}^f | \, t_\pm \sigma_\mu \, | n_{2c}^i \rangle \\ -\delta(p_2^f, p_1^i) \, \langle p_{1c}^f | \, t_\pm \sigma_\mu \, | n_{2c}^i \rangle],\end{aligned} \tag{2.53}$$

$$\begin{aligned}\langle n_1^f n_2^f n_{3c}^f | \, t_\pm \sigma_{-\mu} \, | p_1^i n_1^i n_{2c}^i \rangle = \delta(n_2^f, n_1^i)\delta(n_3^f, n_2^i) \, \langle n_{1c}^f | \, t_\pm \sigma_{-\mu} \, | p_{1c}^i \rangle \\ -\delta(n_1^f, n_1^i)\delta(n_3^f, n_2^i) \, \langle n_{2c}^f | \, t_\pm \sigma_{-\mu} \, | p_{1c}^i \rangle \\ +\delta(n_1^f, n_1^i)\delta(n_2^f, n_2^i) \, \langle n_{3c}^f | \, t_\pm \sigma_{-\mu} \, | p_{1c}^i \rangle \, .\end{aligned} \tag{2.54}$$

2.6.3 Odd-odd nuclei

The states for nuclide consist of odd number of protons as well as neutrons are expressed in terms of quasi-particle transformation i.e. by proton-neutron pair states (two-q.p states) or by four quasi-particles levels, having two protons or two neutrons quasi-particles levels. Two quasi-particles levels are reduced into correlated (c) one quasi-particle states are specified as

$$\langle p_1^f p_{2c}^f | \, t_\pm \sigma_\mu \, | p^i n_c^i \rangle = \delta(p_1^f, p^i) \, \langle p_{2c}^f | \, t_\pm \sigma_\mu \, | n_c^i \rangle - \delta(p_2^f, p^i) \, \langle p_{1c}^f | \, t_\pm \sigma_\mu \, | n_c^i \rangle \, , \tag{2.55}$$

$$\langle n_1^f n_{2c}^f | \, t_\pm \sigma_{-\mu} \, | p^i n_c^i \rangle = \delta(n_2^f, n^i) \, \langle n_{1c}^f | \, t_\pm \sigma_{-\mu} \, | p_c^i \rangle - \delta(n_1^f, n^i) \, \langle n_{2c}^f | \, t_\pm \sigma_{-\mu} \, | p_c^i \rangle \, , \tag{2.56}$$

where the four q.p levels are simplified as following

$$\begin{aligned}\langle p_1^f p_2^f n_1^f n_{2c}^f | \, t_\pm \sigma_{-\mu} \, | p_1^i p_2^i p_3^i n_{1c}^i \rangle = \delta(n_2^f, n_1^i)[\delta(p_1^f, p_2^i)\delta(p_2^f, p_3^i) \, \langle n_{1c}^f | \, t_\pm \sigma_{-\mu} \, | p_{1c}^i \rangle \\ -\delta(p_1^f, p_1^i)\delta(p_2^f, p_3^i) \, \langle n_{1c}^f | \, t_\pm \sigma_{-\mu} \, | p_{2c}^i \rangle + \delta(p_1^f, p_1^i)\delta(p_2^f, p_2^i) \, \langle n_{1c}^f | \, t_\pm \sigma_{-\mu} \, | p_{3c}^i \rangle] \\ -\delta(n_1^f, n_1^i)[\delta(p_1^f, p_2^i)\delta(p_2^f, p_3^i) \, \langle n_{2c}^f | \, t_\pm \sigma_{-\mu} \, | p_{1c}^i \rangle - \delta(p_1^f, p_1^i)\delta(p_2^f, p_3^i) \, \langle n_{2c}^f | \, t_\pm \sigma_{-\mu} \, | p_{2c}^i \rangle \\ +\delta(p_1^f, p_1^i)\delta(p_2^f, p_2^i) \, \langle n_{2c}^f | \, t_\pm \sigma_{-\mu} \, | p_{3c}^i \rangle],\end{aligned} \tag{2.57}$$

$$\begin{aligned}\langle p_1^f p_2^f p_3^f p_{4c}^f | \, t_{\pm}\sigma_{\mu} \, | p_1^i p_2^i p_3^i n_{1c}^i \rangle = -\delta(p_2^f, p_1^i)\delta(p_3^f, p_2^i)\delta(p_4^f, p_3^i) \, \langle p_{1c}^f | \, t_{\pm}\sigma_{\mu} \, | n_{1c}^i \rangle \\ +\delta(p_1^f, p_1^i)\delta(p_3^f, p_2^i)\delta(p_4^f, p_3^i) \, \langle p_{2c}^f | \, t_{\pm}\sigma_{\mu} \, | n_{1c}^i \rangle - \delta(p_1^f, p_1^i)\delta(p_2^f, p_2^i)\delta(p_4^f, p_3^i) \, \langle p_{3c}^f | \, t_{\pm}\sigma_{\mu} \, | n_{1c}^i \rangle \\ +\delta(p_1^f, p_1^i)\delta(p_2^f, p_2^i)\delta(p_3^f, p_3^i) \, \langle p_{4c}^f | \, t_{\pm}\sigma_{\mu} \, | n_{1c}^i \rangle \, ,\end{aligned} \tag{2.58}$$

$$\begin{aligned}\langle p_1^f p_2^f n_1^f n_{2c}^f | \, t_{\pm}\sigma_{\mu} \, | p_1^i n_1^i n_2^i n_{3c}^i \rangle = \delta(p_1^f, p_1^i)[\delta(n_1^f, n_2^i)\delta(n_2^f, n_3^i) \, \langle p_{2c}^f | \, t_{\pm}\sigma_{\mu} \, | n_{1c}^i \rangle \\ -\delta(n_1^f, n_1^i)\delta(n_2^f, n_3^i) \, \langle p_{2c}^f | \, t_{\pm}\sigma_{\mu} \, | n_{2c}^i \rangle + \delta(n_1^f, n_1^i)\delta(n_2^f, n_2^i) \, \langle p_{2c}^f | \, t_{\pm}\sigma_{\mu} \, | n_{3c}^i \rangle] \\ -\delta(p_2^f, p_1^i)[\delta(n_1^f, n_2^i)\delta(n_2^f, n_3^i) \, \langle p_{1c}^f | \, t_{\pm}\sigma_{\mu} \, | n_{1c}^i \rangle - \delta(n_1^f, n_1^i)\delta(n_2^f, n_2^i) \, \langle p_{1c}^f | \, t_{\pm}\sigma_{\mu} \, | n_{2c}^i \rangle \\ +\delta(n_1^f, n_1^i)\delta(n_2^f, n_2^i) \, \langle p_{1c}^f | \, t_{\pm}\sigma_{\mu} \, | n_{3c}^i \rangle],\end{aligned} \tag{2.59}$$

$$\begin{aligned}\langle n_1^f n_2^f n_3^f n_{4c}^f | \, t_{\pm}\sigma_{-\mu} \, | p_1^i n_1^i n_2^i n_{3c}^i \rangle = +\delta(n_2^f, n_1^i)\delta(n_3^f, n_2^i)\delta(n_4^f, n_3^i) \, \langle n_{1c}^f | \, t_{\pm}\sigma_{-\mu} \, | p_{1c}^i \rangle \\ -\delta(n_1^f, n_1^i)\delta(n_3^f, n_2^i)\delta(n_4^f, n_3^i) \, \langle n_{2c}^f | \, t_{\pm}\sigma_{-\mu} \, | p_{1c}^i \rangle \\ +\delta(n_1^f, n_1^i)\delta(n_2^f, n_2^i)\delta(n_4^f, n_3^i) \, \langle n_{3c}^f | \, t_{\pm}\sigma_{-\mu} \, | p_{1c}^i \rangle \\ -\delta(n_1^f, n_1^i)\delta(n_2^f, n_2^i)\delta(n_3^f, n_3^i) \, \langle n_{4c}^f | \, t_{\pm}\sigma_{-\mu} \, | p_{1c}^i \rangle \, ,\end{aligned} \tag{2.60}$$

for all the given amplitudes of quasi-particle transitions the anti-symmetrization of the single q.p levels are considered:

$$\begin{aligned}p_1^f < p_2^f < p_3^f < p_4^f, \\ n_1^f < n_2^f < n_3^f < n_4^f, \\ p_1^i < p_2^i < p_3^i < p_4^i, \\ n_1^i < n_2^i < n_3^i < n_4^i.\end{aligned}$$

Gamow-Teller strength of phonon excitations for each excited level is considered. Where it is supposed that the q.p in the parent nuclide stayed in the same quasi-particle shells.

This extended model of pn-QRPA provides a proper way to calculate the allowed GT strength distribution for any nuclide. These GT strength are considered to have a decisive role in weak interaction reactions, which are then employed as key parameters in the stellar simulations codes.

2.7 Unique first-forbidden (U1F) transitions

The probabilities of the U1F ($|\Delta \mathrm{J}| = 2$) transitions strength are obtained in the same manner as that of GT transitions discussed in previous sections, only the nuclear matrix elements (NME) of ph and pp interactions are replaced. For U1F weak-rates calculations, NME of the separable forces which exist in RPA equation are specified as

$$V^{ph}_{pn,p'n'} = +2\chi f_{pn}(\mu) f_{p'n'}(\mu), \tag{2.61}$$

$$V^{pp}_{pn,p'n'} = -2\kappa f_{pn}(\mu) f_{p'n'}(\mu), \tag{2.62}$$

where

$$f_{pn}(\mu) = < j_p m_p | t_- r [\sigma Y_1]_{2\mu} | j_n m_n >, \tag{2.63}$$

represent the single-particle U1F transition amplitude. It should be noted that μ can take the values of 0,$\pm$1, and $\pm$2, and the neutron and proton states have opposite parities, (however for allowed weak-rates μ only takes the values 0 and $\pm$1).

2.8 Stellar weak-rates formalism

The stellar weak interaction rates from the *ith* state of parent nuclide to the daughter nuclide *jth* state is specified by

$$\lambda_{ij} = \ln 2 \frac{f_{ij}(T, \rho, E_f)}{(ft)_{ij}}, \tag{2.64}$$

where $(ft)_{ij}$ is connected to the reduced transition probability (B_{ij}) by

$$(ft)_{ij} = D/B_{ij}, \tag{2.65}$$

where D is given as

$$D = \frac{2 \ln 2 \hbar^7 \pi^3}{g_v^2 m_e^5 c^4}, \tag{2.66}$$

and B_{ij} is specified by

$$B_{ij} = B(F)_{ij} + ((g_A/g_V)^2 B(GT)_{ij}. \tag{2.67}$$

In this work we have considered the value of D = 6295 s [35] and g_A/g_V as -1.254. The reduced transition probabilities B(F) and B(GT) are specified by

$$B(F)_{ij} = \frac{1}{2J_i+1}\langle j \parallel \sum_k t_{\pm}^k \parallel i\rangle|^2, \tag{2.68}$$

$$B(GT)_{ij} = \frac{1}{2J_i+1}\langle j \parallel \sum_k t_{\pm}^k \overrightarrow{\sigma}^k \parallel i\rangle|^2, \tag{2.69}$$

here $\overrightarrow{\sigma}(k)$ is the spin operator and $t_{\pm}^k$ represent the isospin raising and lowering operator. For parent as well as daughter excited levels construction and calculation of NME we refer to [39]. The phase space (f) integral was taken over total energy. Adopting natural units ($\hbar = c = m_e = 1$), for positron capture (PC) lower sign is used while in case of electron capture (EC) upper sign is used, it is specified by

$$f_{ij} = \int_{w_1}^{\infty} w\sqrt{w^2-1}(w_m+w)^2 F(\pm Z, w) G_{\mp} dw, \tag{2.70}$$

and the f_{nm} for positron (lower sign) or electron (upper sign) emission it is given by

$$f_{ij} = \int_{1}^{w_m} w\sqrt{w^2-1}(w_m-w)^2 F(\pm Z, w)(1-G_{\mp}) dw. \tag{2.71}$$

In case of first-forbidden transitions the phase space integrals are written as

$$\begin{aligned} f = \int_{1}^{w_m} & w\sqrt{w^2-1}(w_m-w)^2[(w_m-w)^2 F_1(\pm Z, w) \\ & +(w^2-1)F_2(\pm Z, w)](1-G\mp)dw, \end{aligned} \tag{2.72}$$

for electron (upper signs) or positron (lower signs) emission, or

$$\begin{aligned} f = \int_{w_1}^{\infty} & w\sqrt{w^2-1}(w_m-w)^2[(w_m-w)^2 F_1(\pm Z, w) \\ & +(w^2-1)F_2(\pm Z, w)](1-G\mp)dw, \end{aligned} \tag{2.73}$$

for continuum electron (upper signs) or positron (lower signs) capture.

In above phase space integrals the total energy of electrons is represented by w, and w_l denotes the total capture threshold energy for EC. Where the electron (positron) distribution functions are represented as $G_{-}(G_{+})$.

$$G_{-} = \left[\exp\left(\frac{E - E_f}{kT}\right) + 1\right]^{-1}, \tag{2.74}$$

$$G_{+} = \left[\exp\left(\frac{E + 2 + E_f}{kT}\right) + 1\right]^{-1}. \tag{2.75}$$

Where $E = (w - 1)$ and E_f depict the K.E and Fermi energy of the electrons, respectively. The Fermi functions ($F(Z, w)$), are determined by using the technique of [81]. If the associated leptons emission total energy (w_m) is larger than -1, then $w_l = 1$, and if it is ≤ 1, then in this case $w_l = |w_m|$, where w_m show the total β-decay energy,

$$w_m = m_p - m_d + E_i - E_j, \tag{2.76}$$

m_p and m_d represent the mass of parent and daughter nuclide, respectively. Whereas, E_i is the energy of excitation of parent nuclide and E_j represent the excitation energy of daughter nuclide. The electrons number density linked with protons and nuclei is $\rho Y_e N_A$ (ρ and N_A is the density of baryon and Avogadro number, respectively).

$$\rho Y_e = \frac{1}{\pi^2 N_A}(\frac{m_e c}{\hbar})^3 \int_0^{\infty} (G_{-} - G_{+}) p^2 dp, \tag{2.77}$$

where $p = (w^2 - 1)^{1/2}$ represent the momentum of electron. Eq. 2.77 was employed for an iterative computation of Fermi energies at given temperature and Y_e values. As a result of very huge temperatures inside the stellar medium, there is always a finite probability to charge-changing reaction rates from the parent excited levels. By considering the thermal equilibrium assumption, one can find the occupation probability of a level (i) as

$$P_i = \frac{exp(-E_i/kT)}{\sum_{i=1} exp(-E_i/kT)}, \tag{2.78}$$

where E_i represent the energy of excitation for the level i. Finally, for any weak processes the weak-rates per unit time per nuclide is achieved as

$$\lambda = \sum_{ij} P_i \lambda_{ij}, \tag{2.79}$$

where P_i obeys the normal Boltzmann distribution. In equation 2.79, the summation is taken on the entire levels (initial and final) until reasonable convergence is obtained in the computed weak-rates.

Chapter 3

Allowed stellar weak interaction rates for *fp*-shell nuclei

3.1 Introduction

The Gamow-Teller ($GT_{\pm}$) transitions are the most significant charge-changing reactions of the spin-isospin ($\sigma\tau_{\pm}$) form. These charge-changing transitions play a decisive role in nucleosynthesis and in supernova explosions [7]. The weak interactions strongly effect the late evolution stages of high mass stars. Their operation controls the ratio of electron to baryon (Y_e) of stellar matter and thus its Chandrasekhar mass that is proportional to ${Y_e}^2$ [82]. The capturing of positron increases electron numbers present for pressure support, however, electron capture proceeds in the reverse direction. (Anti)neutrinos are produced in both processes, and escape from the stars having densities less than 10^{11} g/cm^3 thereby carrying out entropy and energy away from the core. The electron capture (EC) and β-decay rates are governed by Fermi and GT charge-changing strength. The accurate investigation of GT transition is a complex phenomena. Nuclei are completely ionized in the astrophysical domain due to which continuum EC from the degenerate electron plasma occurs. In stellar matter the electrons are able to start transitions to GT resonance, because of their high energies. The EC as well as β-decay take place during the time of hydrostatic burning phases. Furthermore, during final astrophysical evolutionary phases, the importance of these processes increases when the temperature and density of the core become huge and the capture becomes favorable due to the rise in Fermi energy of the electrons [2].

For *fp*-shell nuclide the GT transitions are considered extremely essential for supernova physics [2]. In this chapter we would discuss the GT transitions properties of chromium and odd-A isotopes. GT transitions on these selected isotopes have a special mention as per simulation results of presupernova evolution of high mass stars (e.g. [64, 83]). In the literature, there are few available experimental data on charge-changing GT transitions of chromium isotopes. Zioni et al. (1972) first studied the decay of ^{46}Cr, by using the ^{32}S(^{16}O, 2n) reaction to produce ^{46}Cr [84]. Onishi and collaborators (2005) examined the beta decay of ^{46}Cr. This measurement was done at RIKEN accelerator research facility. In Ref. [85], ^{50}Cr(^{3}He,t)^{50}Mn reaction experiment was performed and made measurements up to 5 MeV in daughter nuclei. But it was Adachi and collaborators (2007) who performed a high resolution measurement of ^{50}Cr(^{3}He,t)^{50}Mn at 0° and at 140 MeV per nucleon incident energies, in order to study GT transitions precisely. In this experiment the authors have measured the charge-changing transitions up to 12 MeV in ^{50}Mn [86].

There is a need to obtain more experimental data on GT strength in *fp*-shell nuclide. It is also necessary to investigate the charge-changing transition strength for exotic nuclide close to proton and neutron drip lines. Simulation of stellar events require GT strength distributions, preferably for hundreds of nuclei. Because of scarcity of experimental data, one is compelled to calculate the charge-changing transition functions for *fp*-shell nuclide by using microscopic nuclear theories [87]. It is also essential to note that in the *fp*-shell nuclide, the GT strength is distributed over several discrete states (i.e. strength is fragmented) and in presupernova models the information of these low-lying strengths is very significant for a precise time evolution of Y_e [2, 64]. The knowledge of measured GT strength should be broadened and theoretical attempts should be done to reproduce them and calculate strengths of nuclide far from the stability line [66].

The first extensive attempt for the investigation of weak reactions rates at high densities and temperatures was made by Fuller et al. [2]. The experimental results available at that time were also incorporated. The Fuller et al. work for *fp*-shell nuclei was later extended by [64]. In this chapter the microscopic calculation of charge-changing GT transitions and EC rates for chromium isotopes (^{42}Cr - ^{65}Cr) and odd-A fp-shell nuclei (^{45}Sc and ^{55}Mn) are presented by using the deformed pn-QRPA model. This microscopic model [29, 76, 80] is proven to be a very decent model for the determination of nuclear beta deacy half-lives for nuclide posses far away from the line of stability [80, 88]. In the past this model was adequately used for the computation of terrestrial half-lives and was found to be in excellent agreement with the measurements [35]. This microscopic model was changed later in order to consider the transitions from excited levels [79]. For the first time, this model was employed to compute the weak-decay rates and cooling/heating rates in stellar content for sd-shell nuclide [39] and later for fp/fpg-shell nuclide [40].
In a recent study by Cole et al. [89] on odd-A nuclei (^{45}Sc and ^{55}Mn), it was concluded that QRPA calculations show larger deviations and overestimate the total experimental Gamow-Teller strength. It was also concluded that QRPA calculated electron capture rates exhibit larger deviation than those derived from the measured GT strength. This study gives useful information on the performance of QRPA-based nuclear models and has probed the findings of the Cole et al. study.

3.2 Theoretical assumptions and model parameters

We have made the following assumptions in the calculations of stellar weak-rates:

(i) Only super-allowed Fermi and GT charge-changing transitions were investigated. The forbidden transitions contributions to total rates were assumed comparatively negligible.

(ii) The stellar interior temperature was supposed high enough so that the electrons were not bound to the nucleus anymore and obeyed the Fermi-Dirac distribution. Positrons are created at kT > 1 MeV, and took the same distribution function as that of electrons.

(iv) (Anti)neutrinos are produced during weak-decay reactions and escaped from the stellar content freely.

For the stellar weak-rates calculation different model parameters are to be carefully selected. As discussed in previous chapter, the Hamiltonian for pn-QRPA model is;

$$H^{pn-QRPA} = H^{sp} + V^{pairing} + V^{ph}_{GT} + V^{pp}_{GT}, \tag{3.1}$$

where H^{sp} represents the single-particle Hamiltonian, $V^{pairing}$ denotes the pairing force, V^{ph}_{GT} represents the particle-hole (*ph*) GT force and V^{pp}_{GT} is the particle particle (*pp*) GT force. Single particle energies and wave functions were calculated in the Nilsson model [69], in which the nuclear deformations was considered. Pairing among nucleons was incorporated within the BCS approximation. The proton-neutron residual interactions appear in two different forms, i.e. *ph* and *pp* interactions, characterized by two interaction constants χ and κ, respectively. The selections of these two constants were done in an optimal fashion to reproduce available experimental data and fulfilment of model independent Ikeda sum rule [90]. In this work, we choose the value of χ to be 4.2/A, showing a $1/A$ dependence [36] and κ equal to 0.10. Other parameters necessary for electron capture calculations are the nuclear deformations, Nilsson potential parameters (NPP), the pairing gaps, and the Q-values. NPP were chosen from [91] and the Nilsson oscillator constant was taken as $\hbar\omega = 41A^{-1/3}(MeV)$. The computed half-lives depend just weakly on the pairing gaps values [92]. Therefore, the conventional values of

$$\Delta_p = \Delta_n = 12/\sqrt{A}(MeV)$$

were applied in this work. For these even-even ^{48,50,52,54}Cr isotopes the experimentally calculated values were taken from [93]. For other nuclide (odd-A) the deformation parameter was calculated as

$$\delta = \frac{125(Q_2)}{1.44(Z)(A)^{2/3}}, \tag{3.2}$$

where Z and A are the charge and nucleon numbers, respectively, and Q_2 is the electric quadrupole moment taken from Ref. [94]. Q-values were taken from the Ref. [95].

3.3 Weak-rates on chromium (Cr) isotopes

3.3.1 β-decay half-lives of Cr isotopes

The deformed pn-QRPA model was used for the computation of nuclear β-decay half-lives ($T_{1/2}$) and astrophysical electron capture (EC) rates. We consider 24 isotopes of chromium, in mass range $^{42-65}$Cr, for the estimations of EC rates. These nuclide include both stable (^{50}Cr, $^{52-54}$Cr) and unstable isotopes of chromium, including neutron deficient and neutron rich cases. We quenched our pn-QRPA results by a factor of $f_q^2 = (0.6)^2$ [42,96] in calculation of EC rates (akin to other microscopic calculations including shell model calculations).
Fig. 3.1 shows that our calculated β-decay $T_{1/2}$ values for isotopes of chromium agree quite well with the measured values. The measured $T_{1/2}$ values were taken from [95]. As mentioned earlier, ^{50}Cr, ^{52}Cr, ^{53}Cr and ^{54}Cr are stable isotopes of chromium.

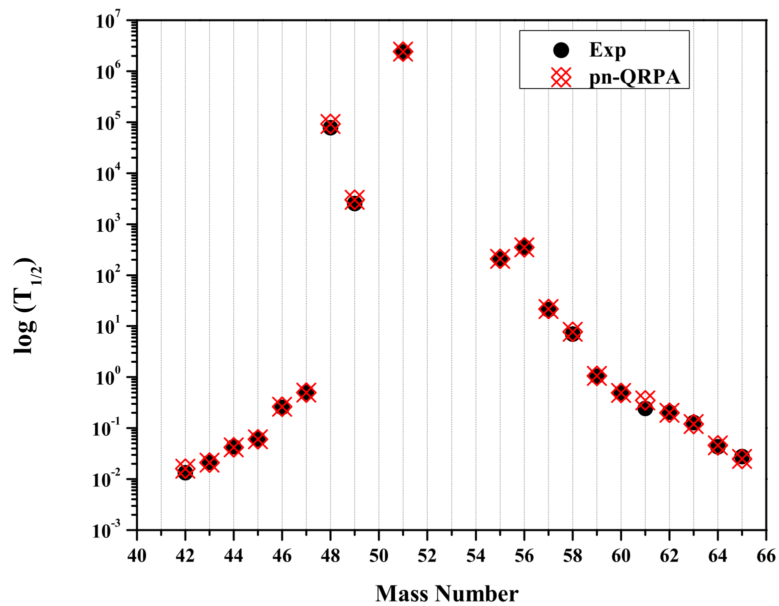

Figure 3.1: Total β-decay half-lives for Cr isotopes calculated from the pn-QRPA model (this work) in comparison with the experimental data [95]. $^{50,52-54}$Cr are stable.

3.3.2 Ikeda Sum Rule (ISR)

The total GT$_+$ and GT$_-$ strengths are connected to the re-normalized Ikeda sum rule (ISR$_{re-norm}$) [90] as

$$ISR_{re-norm} = \sum B(GT_-) - \sum B(GT_+) \cong 3f_q^2(N-Z). \tag{3.3}$$

where Z denote the numbers of protons and N denote the numbers of neutrons. Figure 3.2 depicts the comparison of calculated $ISR_{re-norm}$ with the model-independent theoretical predictions. It is clear from Fig. 3.2 that the $ISR_{re-norm}$ is satisfied well in our calculations (deviates at the maximum by only a few percent). Thus the deformed pn-QRPA model results fulfilled well the ISR for selected Cr isotopes.

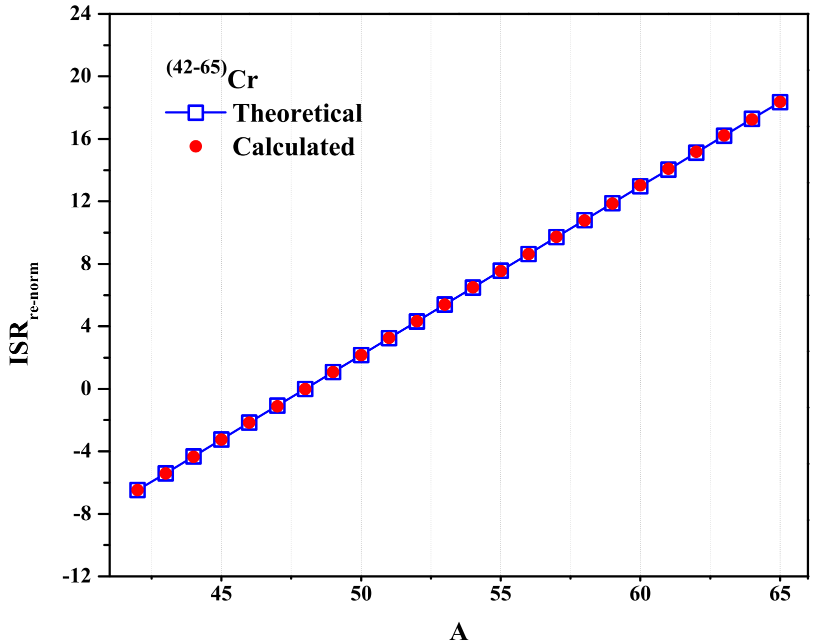

Figure 3.2: Comparison of calculated and theoretical re-normalized Ikeda Sum Rule.

3.3.3 Electron capture rates on chromium nuclide

The deformed pn-QRPA computed electron capture (EC) rates on Cr nuclide are depicted in Table 3.1. These capture rates are presented for temperatures (1, 3, 10 and 30)$\times 10^9 K$ and at selected densities (10^3, 10^7 and $10^{11} gcm^{-3}$). It is to be kept in mind that the computed EC weak-rates are shown in log to base 10 values (in units of s^{-1}). The EC rates rises, as the temperature of the core and stellar density increases. This is because that the possibility of occupation of parent excited levels increases as the temperature rises and hence at high temperatures the EC rates contribute effectively. The Fermi energy of electrons increases with increasing stellar densities. This leads to substantial increment of EC rates at high density. However at high densities the rate of change of EC decreases with temperature.

Table 3.1: Calculated EC rates in stellar region on chromium ($^{42-65}$Cr) isotopes at various densities and temperatures. The first column shows the stellar densities (ρY_e) (in units of g/cm^3), where ρ is the baryon density and Y_e is the ratio of the electron number to the baryon number. T_9 are given in units of 10^9 K. The calculated EC rates are tabulated in log to base 10 scale and given in units of s^{-1}.

$\log \rho Y_e$	T_9	^{42}Cr	^{43}Cr	^{44}Cr	^{45}Cr	^{46}Cr	^{47}Cr	^{48}Cr	^{49}Cr	^{50}Cr	^{51}Cr	^{52}Cr	^{53}Cr
3	1	-3.239	-3.396	-3.428	-3.383	-3.935	-4.294	-5.917	-5.674	-13.029	-5.104	-26.535	-23.539
3	3	-0.941	-1.057	-1.119	-1.090	-1.609	-1.848	-3.314	-3.062	-5.872	-2.401	-10.061	-8.695
3	10	0.990	0.946	0.860	0.848	0.489	0.252	-0.571	-0.501	-1.341	0.141	-2.246	-2.010
3	30	3.054	3.343	3.158	3.215	2.803	2.466	2.274	2.373	1.999	2.934	1.802	2.021
7	1	0.463	0.305	0.283	0.327	-0.209	-0.576	-1.954	-1.818	-7.209	-0.924	-20.724	-17.736
7	3	0.474	0.358	0.301	0.331	-0.180	-0.425	-1.789	-1.572	-4.159	-0.833	-8.358	-6.984
7	10	1.082	1.038	0.953	0.940	0.582	0.344	-0.475	-0.405	-1.244	0.238	-2.148	-1.911
7	30	3.058	3.347	3.161	2.806	3.218	2.470	2.278	2.377	2.003	2.938	1.806	2.024
11	1	5.360	5.263	5.338	5.375	5.098	4.860	4.811	4.688	4.611	5.625	4.510	4.394
11	3	5.361	5.273	5.338	5.389	5.099	4.910	4.812	4.726	4.611	5.627	4.511	4.396
11	10	5.385	5.338	5.364	5.395	5.153	5.081	4.832	4.774	4.631	5.630	4.539	4.498
11	30	5.633	5.905	5.775	5.478	5.862	5.202	5.120	5.254	4.949	5.762	4.889	5.112

$\log \rho Y_e$	T_9	^{54}Cr	^{55}Cr	^{56}Cr	^{57}Cr	^{58}Cr	^{59}Cr	^{60}Cr	^{61}Cr	^{62}Cr	^{63}Cr	^{64}Cr	^{65}Cr
3	1	-40.534	-34.933	-51.155	-45.571	-62.707	-55.426	-73.862	-68.342	-86.371	-75.944	-95.139	-81.490
3	3	-13.788	-11.869	-17.515	-15.417	-20.408	-18.451	-23.950	-23.113	-28.681	-26.338	-30.957	-27.670
3	10	-2.952	-2.403	-3.647	-3.386	-3.992	-3.894	-4.995	-5.746	-7.168	-7.703	-7.066	-7.735
3	30	1.634	1.895	1.540	1.485	1.491	1.392	1.263	0.449	-0.212	-0.712	0.593	-0.523
7	1	-34.714	-29.113	-45.335	-39.751	-56.887	-49.606	-68.042	-62.522	-80.552	-70.124	-89.319	-75.670
7	3	-12.073	-10.153	-15.799	-13.702	-18.693	-16.736	-22.235	-21.398	-26.965	-24.622	-29.241	-25.955
7	10	-2.854	-2.304	-3.548	-3.288	-3.893	-3.795	-4.897	-5.647	-7.069	-7.604	-6.967	-7.636
7	30	1.638	1.898	1.543	1.489	1.495	1.395	1.266	0.453	-0.209	-0.708	0.596	-0.520
11	1	4.423	4.394	3.829	4.080	2.985	3.449	2.578	3.000	2.403	2.210	1.766	2.516
11	3	4.424	4.483	3.831	4.180	2.988	3.396	2.583	3.297	2.413	2.313	1.787	2.512
11	10	4.458	4.667	4.137	4.283	3.791	3.715	3.161	3.692	3.013	2.843	3.054	2.655
11	30	4.819	5.062	4.753	4.691	4.696	4.619	4.585	3.982	3.422	3.009	4.212	3.215

The calculated EC rates on selected chromium isotopes ^{50}Cr, ^{51}Cr, ^{53}Cr, ^{56}Cr and ^{57}Cr of astrophysical importance are shown in Fig. 3.3. Isotopes of chromium, namely ^{51,53,56,57}Cr, were included in the Aufderheide's list of key nuclei for electron capture rates [64]. In addition, ^{50}Cr, ^{51}Cr, and ^{53}Cr were considered amongst the most important nuclei for modeling of presupernova evolution of massive stars that decrease Y_e of stellar matter (for detail see [83]). Graphs in Fig. 3.3 illustrate that the EC rates remain, more or less, constant in low density regions. In these regions the beta-decay compete well with capture rates before core collapse. As the stellar core stiffens to high values ($10^8 gcm^{-3} - 10^{11} gcm^{-3}$), the electron Fermi energy also increases thereby increasing the EC rates. At later stages of the core-collapse supernova, β-decay becomes unimportant as an increased in electron chemical potential, noticeably, decreases the phase space. These high EC rates make the stellar matter heavier. Thus in the final state of the collapse phase the β-decay is relatively trivial due to Pauli-blocking of the electron phase space [97].

3.3.4 Comparison of electron capture rates with LSSM and FFN

Large scale shell model (LSSM) was used to compute the EC rates on $^{45-58}$Cr [98]. Fuller, Fowler, and Newman (FFN) [2], on the other hand, used their model to calculate EC rates on $^{45-60}$Cr isotopes. The FFN calculations have been employed in several simulation codes, while LSSM rates were employed in recent simulation of presupernova evolution of massive stars in the mass range 11-40 M$_\odot$ [83]. The comparison of calculated weak reaction rates with the previous results of FFN [2] and LSSM calculation [98] are shown in Figs. 3.4 and 3.5. In these figures, for each isotope, we depict three panels. In each case the upper panel shows comparison of calculated EC rates at temperature $1 \times 10^9 K$, whereas the middle and lower panels show comparison at temperatures $10 \times 10^9 K$ and $30 \times 10^9 K$, respectively. The selected values of densities are 10^3 gcm^{-3}, 10^7gcm^{-3} and 10^{11}gcm^{-3} (corresponding to low, medium and high densities). Comparison of the capture rates with previous calculations can be divided into two categories. In first category our rates are enhanced at all temperatures and densities compared to previous calculations by as much as two orders of magnitude. The results are shown in Fig. 3.4.

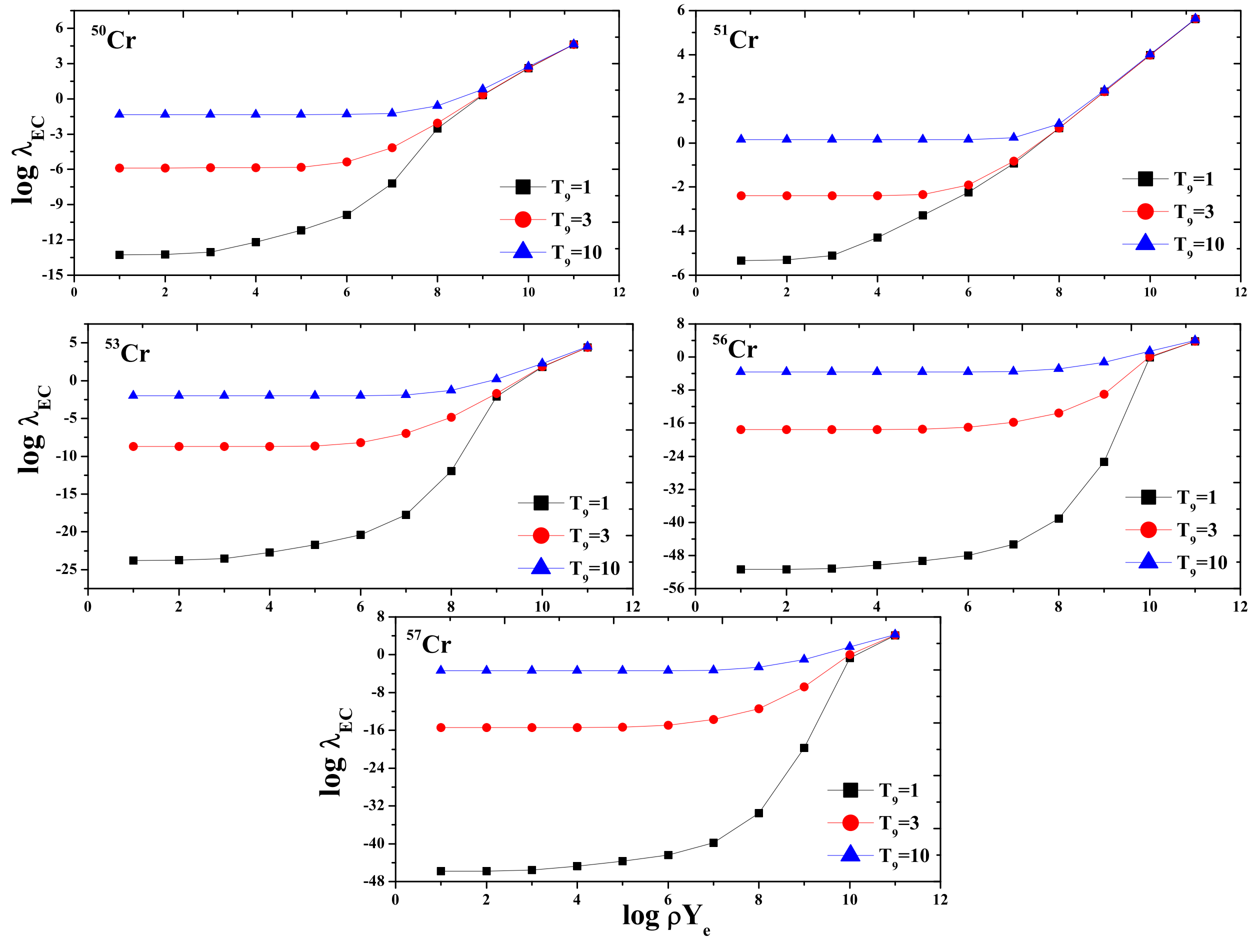

Figure 3.3: Electron capture rates on (^{50,51,53,56,57}Cr) isotopes as function of stellar densities (ρY_e) having units of g/cm^3 at different selected temperatures. Temperatures (T_9) are given in units of 10^9 K and $\log \lambda_{EC}$ represents the log (to base 10) of EC rates in units of s^{-1}.

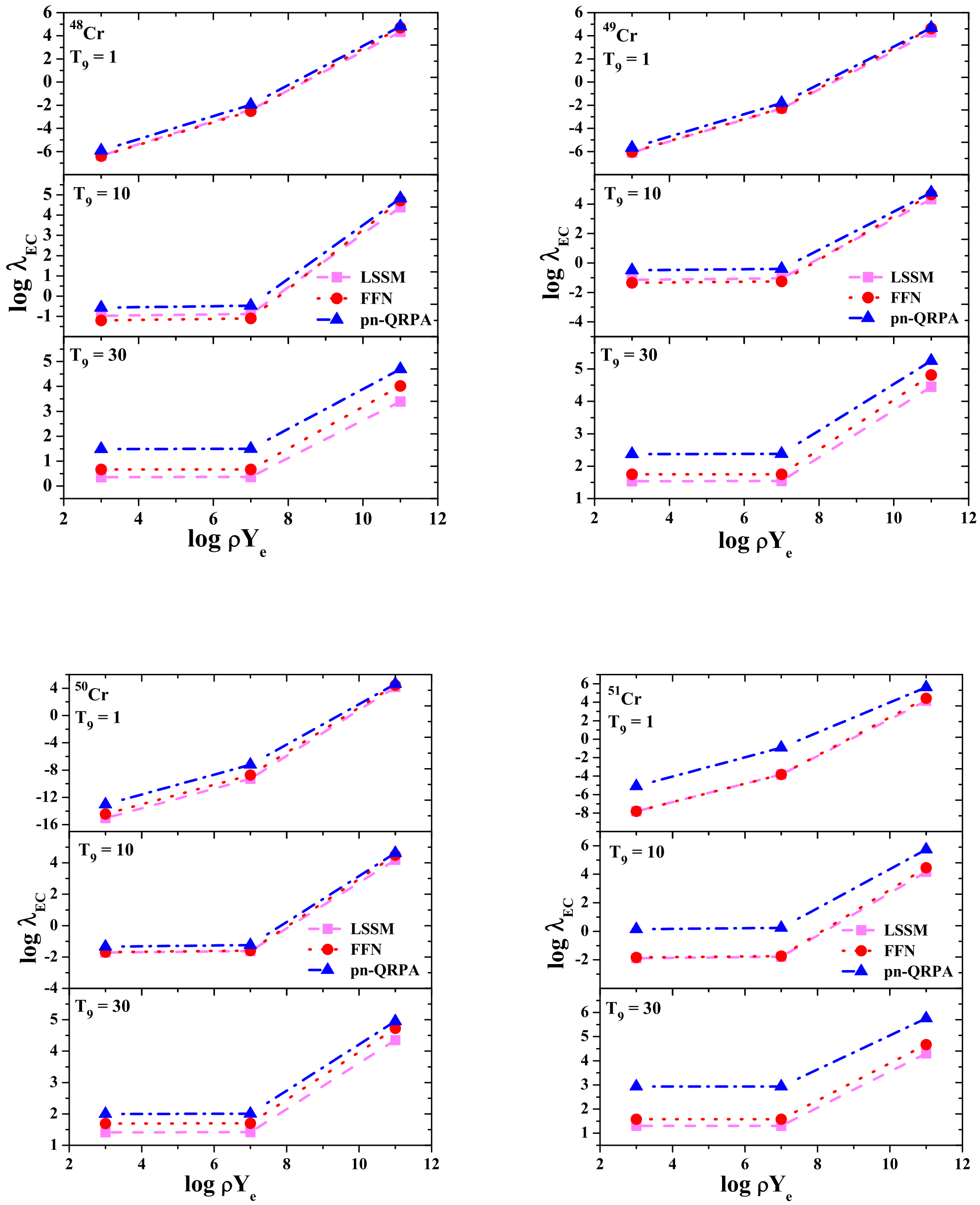

Figure 3.4: Comparison of EC rates of pn-QRPA (this work) with those of FFN [2] and large scale shell model (LSSM) [98] as function of stellar densities (ρY_e) having units of g/cm^3 at different selected temperatures. Temperatures (T_9) are given in units of 10^9 K and $\log \lambda_{EC}$ represents the log (to base 10) of EC rates in units of s^{-1}.

The total charge-changing transitions strength, calculated centroids and widths of GT strength can be seen in Table 3.2. Both EC and positron-decay rates are very sensitive to the position of the GT_+ centroid. The (n,p) reaction experiment on a nuclei (Z, A) depicts the position where in (Z-1, A) the GT_+ centroid analogous to the ground level of (Z, A) resides. The EC/β^+-decay are sensitive to the position of GT_+ resonance exponentially, whereas the total transitions probabilities affect the stellar weak-decay rates in a more or less linear style [99]. The widths of charge-changing transitions strength give an idea that how much the individual Gamow-Teller levels are scattered around the given centroid. The total $B(GT_+)$ strength decreases monotonically as the mass number increases. For both even and odd mass nuclei, the GT resonance energy for FFN cluster around 2, 4, and 6 MeV. The LSSM calculated centroid energies are scattered as the residual interaction fragment the charge-changing GT strength (see Fig. 6 of [65]). Table 3.2 clearly shows that the deformed pn-QRPA computed centroid values of charge-changing GT strength are also scattered due to fragmentation of the GT strength. Compared to the LSSM centroids, FFN place the GT resonance energy usually at higher excitation energies for even-even nuclide and often at too low excitation energies for odd-odd nuclide. FFN place the GT resonance energy at around 6 MeV for odd-A nuclide having odd number of neutrons. Compared to the deformed pn-QRPA and LSSM computed GT centroids, the FFN estimate for these nuclide are too high. The EC rates calculated by the pn-QRPA model are bigger than those calculated by FFN and LSSM due to lower placement of centroids in our model.

Table 3.2: The pn-QRPA calculated total B(GT) strengths, centroids and widths of Cr isotopes in electron capture direction.

Nuclei	$\sum$ B(GT$_+$)	$\bar{E}_+$ (MeV)	Width$_+$ (MeV)
^{42}Cr	7.08	6.80	3.25
^{43}Cr	5.95	9.74	3.10
^{44}Cr	5.33	7.96	5.55
^{45}Cr	4.24	7.95	3.09
^{46}Cr	4.31	4.76	3.31
^{47}Cr	3.24	8.81	3.26
^{48}Cr	3.33	4.19	2.56
^{49}Cr	2.23	7.90	2.04
^{50}Cr	2.49	4.03	2.41
^{51}Cr	1.87	7.96	2.41
^{52}Cr	2.21	3.23	2.01
^{53}Cr	0.51	6.21	2.71
^{54}Cr	1.95	2.11	3.68
^{55}Cr	0.39	4.06	3.47
^{56}Cr	1.31	1.77	2.14
^{57}Cr	0.25	5.21	2.84
^{58}Cr	0.82	1.57	2.49
^{59}Cr	0.24	1.26	2.24
^{60}Cr	0.39	3.03	4.99
^{61}Cr	0.21	3.79	3.41
^{62}Cr	0.23	3.22	5.51
^{63}Cr	0.17	1.83	2.69
^{64}Cr	0.16	2.63	5.06
^{65}Cr	0.12	2.87	3.31

In the other category at lower stellar temperatures our results are in reasonable accordance with LSSM results. However in case of ^{56,58}Cr isotopes at low density and low temperature domain, deformed pn-QRPA and shell model EC rates are greater by around seven orders of magnitude as compared to FFN. At high density and low temperature domain the matching between all calculations is decent. Fig. 3.5 shows the mutual comparison of EC rates for this category. At high temperatures and density region the situation is more interested if we compare the results of LSSM and FFN. At high temperature and density region, the LSSM EC rates are very small as compared to FFN and pn-QRPA rates. The Lanczos-based technique used by LSSM and pointed by [100] gives the reason for this discrepancy. The calculated LSSM weak-decay rates is a function of the number of Lanczos iterations important for convergence and this behavior of partition functions can affect their estimates of high temperature weak-rates. Accordingly at high temperatures the LSSM capture rates are too smaller. The pn-QRPA computation did not posses such type of issues as it is not Lanczos-based. At higher temperatures, where the probability of parent excited levels is higher, our capture rates for all selected nuclide are enhanced by an order of magnitude as compared to LSSM rates. There are numerous other reasons which causes the enhancement of our computed weak-rates. The deformed pn-QRPA model provides reasonable model space which adequately handle all the excited states in parent as well as in daughter nuclei. We also did not take the Brink-Axel hypothesis in our estimations to approximate the contribution from parent excited levels. This approximation was employed by FFN as well as LSSM. Brink's hypothesis states that GT strength distribution on excited states is *identical* to that from ground state, shifted *only* by the excitation energy of the state. We carried out a state-by-state calculation of these capturing rates from parent to daughter states in a microscopic way and added them at the end to get the total EC rates (Eq. 2.79). It is further to be noted that both LSSM as well as pn-QRPA model performed a microscopic calculation of all energy eigenvalues and GT matrix elements for ground level of parent nuclide. Thats why, whenever the ground level weak-rates effect the total decay-rates, then both the results are found to be in decent comparison. However, for nuclei where excited state partial rates command the total weak-rates, dissimilarities are found between the two calculated results.

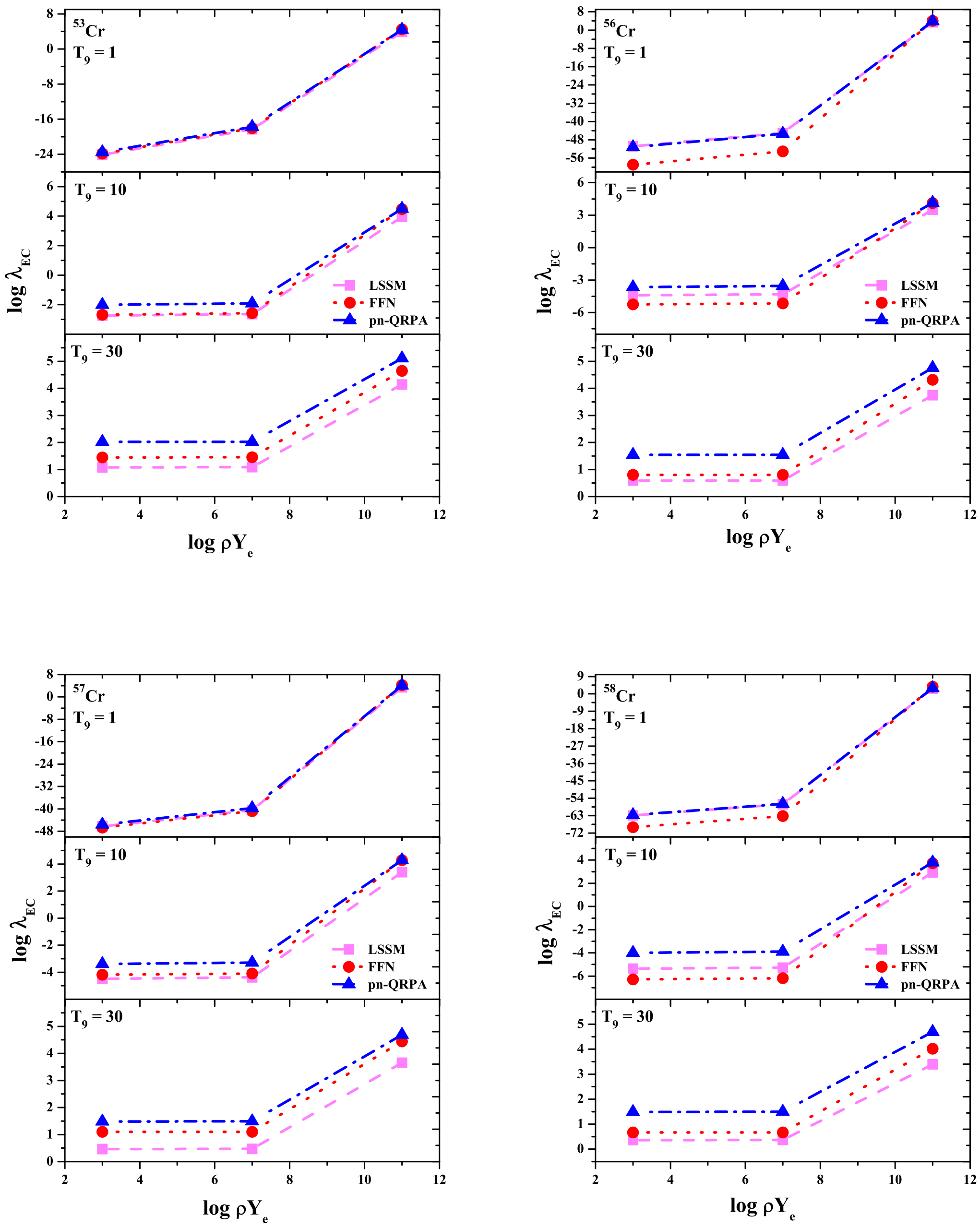

Figure 3.5: Same as Fig. 3.4, but for $^{53,56-58}$Cr isotopes.

3.3.5 Electron capture rates versus β^+-decay rates

One important question could be to know how the EC weak-rates compete with the β^+-decay rates for these isotopes of chromium during presupernova evolution of high mass stars. Table 3.3 demonstrates the ratio of calculated EC to β^+-decay rates at selected temperatures (1, 5, 10 and 30)$\times 10^9 K$ and densities (10^7, 10^9 and $10^{11} gcm^{-3}$). It is observed that in $^{42-47}$Cr nuclide at stellar temperatures (1, 5, and 10)$\times 10^9 K$ and density 10^7 gcm^{-3}, β^+ weak-rates are greater than the EC rates by 1-2 orders of magnitude and must be taken into account in simulation codes. At high densities $(10^9 - 10^{11})$ g/cm^3 the EC rates are bigger than the competing β^+ rates by 1-4 orders of magnitude. As discussed earlier the electron Fermi energy increases at high densities which in turn lead to significant enhancement in calculated electron capture rates. As $N \geq Z$, it is clear from Table 3.3 that the EC rates exceed the competing β^+ rates both in low and high temperature and density region. The β^+-decay values decrease as the neutron number (N) increases. As N $\geq$ 31, calculated β^+-decay rates become less than 10^{-100} and are not shown in Table 3.3. For all these isotopes the β^+-decay rates can safely be ignored in comparison with the EC rates.

Table 3.3: Ratio of calculated electron capture (EC) rates to β^{+}-decay for different selected densities and temperatures. The second column shows the stellar densities (ρY_e) (in units of g/cm^3). T_9 are given in units of 10^9 K.

Nucleus	ρY_e	$R(EC/\beta^{+})$			
		T_9=01	T_9=05	T_9=10	T_9=30
^{42}Cr	10^7	6.6E-02	7.5E-02	2.2E-01	4.4E+00
	10^9	1.0E+01	1.1E+01	1.0E+01	8.6E+00
	10^{11}	5.2E+03	5.2E+03	4.4E+03	1.5E+03
^{43}Cr	10^7	4.2E-02	4.0E-02	8.9E-02	2.5E+00
	10^9	6.8E+00	5.7E+00	3.9E+00	4.8E+00
	10^{11}	3.8E+03	2.9E+03	1.8E+03	8.4E+02
^{44}Cr	10^7	1.2E-01	1.4E-01	4.3E-01	1.2E+01
	10^9	2.1E+01	2.2E+01	2.1E+01	2.3E+01
	10^{11}	1.3E+04	1.3E+04	1.1E+04	4.4E+03
^{45}Cr	10^7	1.8E-01	2.1E-01	7.3E-01	2.3E+01
	10^9	3.4E+01	3.4E+01	3.5E+01	4.3E+01
	10^{11}	2.2E+04	2.1E+04	2.0E+04	8.7E+03
^{46}Cr	10^7	2.3E-01	2.9E-01	9.1E-01	4.4E+01
	10^9	5.4E+01	5.6E+01	4.7E+01	8.2E+01
	10^{11}	4.7E+04	4.7E+04	3.3E+04	1.7E+04
^{47}Cr	10^7	2.5E-01	3.0E-01	1.2E+00	9.1E+01
	10^9	5.4E+01	5.3E+01	5.9E+01	1.7E+02
	10^{11}	6.9E+04	5.3E+04	5.0E+04	3.9E+04
^{48}Cr	10^7	1.5E+03	4.6E+02	2.0E+01	3.5E+02
	10^9	2.1E+06	2.8E+05	1.7E+03	6.5E+02
	10^{11}	8.6E+09	1.0E+09	3.9E+06	1.9E+05
^{49}Cr	10^7	2.9E+01	3.3E+01	6.1E+01	2.0E+03
	10^9	2.6E+04	1.4E+04	4.2E+03	3.6E+03
	10^{11}	9.2E+07	3.8E+07	8.5E+06	1.1E+06
^{50}Cr	10^7	2.9E+14	8.8E+02	7.9E+01	1.8E+03
	10^9	9.6E+21	2.8E+06	8.3E+03	3.3E+03
	10^{11}	1.9E+26	4.1E+10	5.4E+07	1.2E+06
^{51}Cr	10^7	6.5E+07	9.0E+04	6.7E+03	2.3E+04
	10^9	1.1E+11	5.0E+07	4.9E+05	4.2E+04
	10^{11}	2.3E+14	9.4E+10	1.5E+09	1.2E+07
^{52}Cr	10^7	5.2E+11	5.1E+03	6.5E+02	8.8E+03
	10^9	2.2E+30	7.7E+07	8.1E+04	1.6E+04
	10^{11}	8.9E+36	4.2E+13	2.9E+09	8.1E+06
^{53}Cr	10^7	1.2E+23	1.2E+06	3.7E+04	2.1E+06
	10^9	5.2E+38	4.6E+09	4.1E+06	3.6E+06
	10^{11}	1.6E+45	1.0E+15	8.4E+10	1.7E+09
^{54}Cr	10^7	9.5E+14	1.2E+06	3.3E+05	3.2E+07
	10^9	1.0E+35	2.7E+10	4.7E+07	5.3E+07
	10^{11}	1.3E+54	5.2E+17	5.5E+12	2.9E+10

3.4 Weak-rates on odd-A nuclei in stellar matter

3.4.1 Comparison of GT strength with measured and earlier theoretical work

The charge-changing transitions from the ground level of ^{45}Sc (parent nuclide) to ^{45}Ca (daughter nucleus) levels is shown in Fig. 3.6. The transition strength linking the ground level of ^{55}Mn to ^{55}Cr in the GT$_{+}$ direction is shown in Fig. 3.7. The comparison of pn-QRPA computed GT distribution strength with experiment and previous theoretical calculations are also presented in Figs. 3.6 and 3.7. There are six panels in each figure. Panel (a) shows the (n,p) GT data of the experiment performed by Alford and collaborators [101]. Data were only presented in energy bins (E$_{ex}$) of 1 MeV due to the limited resolution of charge-changing (n,p) reaction in the experiment. It was further noted by the authors in Ref. [101] that the upper limit of the extracted charge-changing strength in daughter nuclei (^{45}Ca, ^{55}Cr) was up to E$_{ex}$ of 2 MeV possibly due to the contamination on hydrogen in the target. Panel (b) depicts the GT distribution computed by employing the current pn-QRPA approach. The quenching factor (f$_{q}$) value considered in our results is 0.6. Panel (c) shows the QRPA calculation of GT distribution employing the Skyrme interactions [102] (shown as QRPA(S)). Sarriguren used a f$_{q}$ value of 0.7 and the Skyrme force SLy4 [103] for this calculation. Panel (d) depicts the theoretical GT transition strength using QRPA formalism of Ref. [32] (shown as QRPA(M)) employing the deformation and masses achieved from the FRDM [104]. Results of QRPA(M) are divided by a factor of 3. Panels (e) and (f) show the spin-isospin transitions using shell-model employing the interactions KB3G [105] and GXPF1a [106], accordingly.

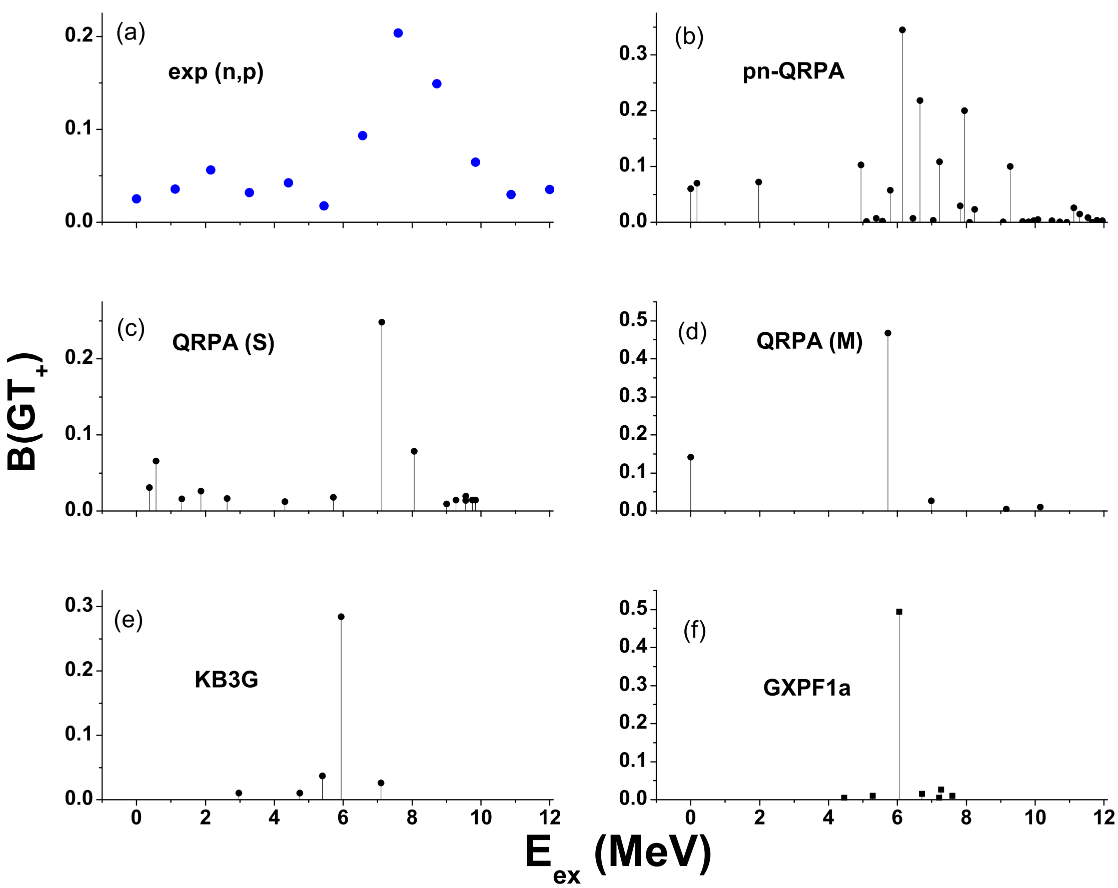

Figure 3.6: Comparison of calculated B(GT$_+$) strength distributions for ^{45}Sc with measured data and previous calculations.

The shell model (SM) results used a f$_q$ value of 0.74 in their calculation. It is noted from figure 3.6 that our calculated strength distribution is well fragmented and, unlike previous theoretical estimates, do not put bulk of strength in one single transition. For the case of ^{55}Mn, Fig. 3.7 shows that the QRPA models calculate bigger GT transitions as compared to SM calculation.

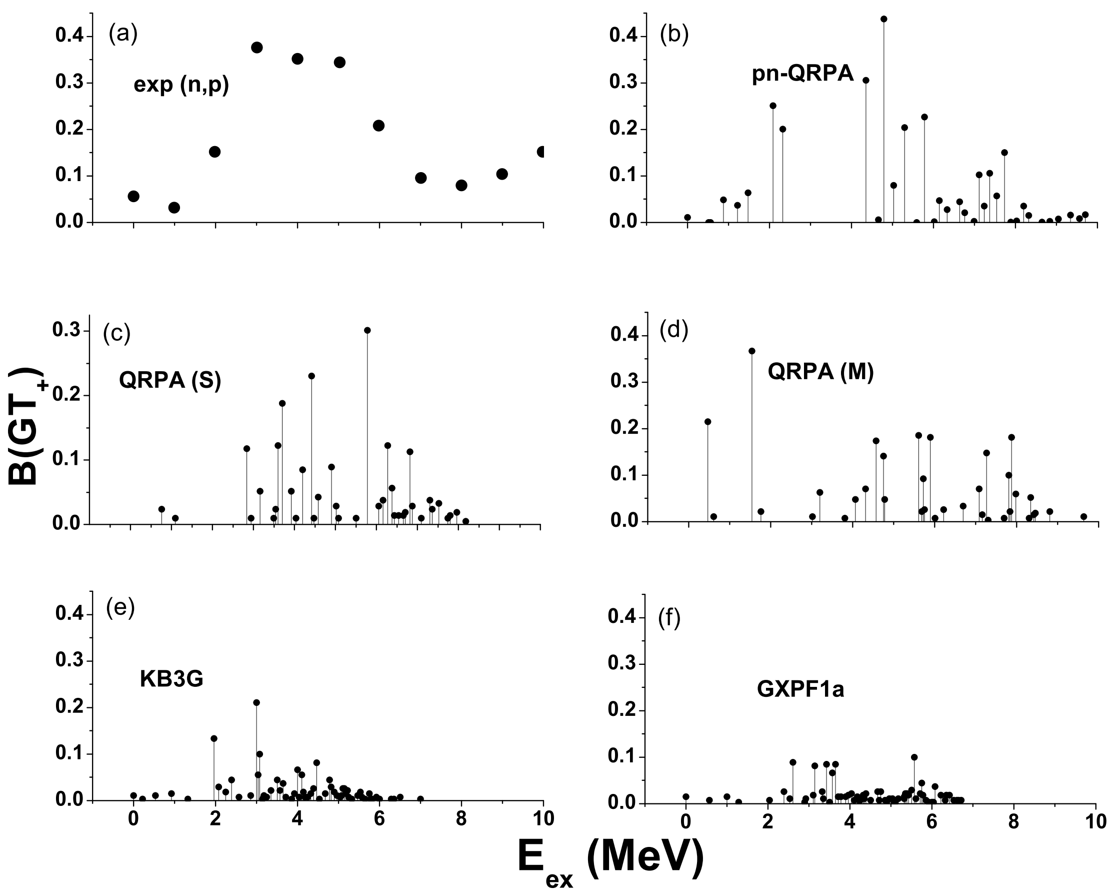

Figure 3.7: Comparison of calculated B(GT$_+$) strength distributions for ^{55}Mn with measured data and previous calculations.

3.4.2 Electron capture and positron emission weak-rates for ^{45}Sc and ^{55}Mn

The deformed pn-QRPA computed EC and positron emission (PE) weak-rates for ^{45}Sc and ^{55}Mn, at selected stellar density and temperature values, are shown in Tables 3.4 and 3.5, respectively. The weak-rates are presented for stellar temperature range (0.7–30)$\times 10^9$ K at stellar densities (10^2, 10^5, 10^8 and 10^{11}) gcm^{-3}. The calculated EC and PE rates (Eq. 15) are stated in $\log_{10}$ values (in units of s^{-1}). The weak-rates increase as the stellar temperature rises. This increase is due to the fact that the occupation probability of parent excited states increase with rising of stellar core temperature. As the core stiffens, the electron Fermi energy level rises. This leads to sizeable increase of EC rates at high stellar density. The PE rates remains more or less constant as the stellar core stiffens. In our calculation it is assumed that positrons generate via electron–positron pair creation, at high stellar temperatures ($kT > 1$ MeV). It is noted that at low temperatures and high stellar density regions the PE weak-rates are orders of magnitude smaller than the EC rates and may be safely omitted in simulation codes.

Table 3.4: Calculated electron capture (EC) and positron emission (PE) rates in stellar matter for ^{45}Sc as a function of stellar density and temperature. ρY_e show the stellar density (in units of g/cm^3) and temperature (T_9) is given in units of 10^9 K. The calculated rates are tabulated in log to base 10 scale and given in units of s^{-1}.

ρY_e	T_9	EC	PE	ρY_e	T_9	EC	PE
10^2	0.7	-13.999	-18.130	10^8	0.7	-7.342	-18.130
10^2	1	-11.228	-14.699	10^8	1	-5.504	-14.699
10^2	1.5	-8.587	-12.053	10^8	1.5	-4.070	-12.049
10^2	2	-7.130	-10.754	10^8	2	-3.345	-10.742
10^2	3	-5.472	-9.491	10^8	3	-2.598	-9.454
10^2	5	-3.808	-6.785	10^8	5	-1.945	-6.777
10^2	10	-1.788	-3.322	10^8	10	-1.080	-3.305
10^2	15	-0.308	-2.198	10^8	15	-0.043	-2.178
10^2	20	0.746	-1.681	10^8	20	0.861	-1.665
10^2	25	1.502	-1.402	10^8	25	1.561	-1.391
10^2	30	2.075	-1.236	10^8	30	2.109	-1.228
10^5	0.7	-11.060	-18.130	10^{11}	0.7	3.794	-18.130
10^5	1	-9.207	-14.699	10^{11}	1	3.794	-14.699
10^5	1.5	-7.711	-12.050	10^{11}	1.5	3.796	-12.049
10^5	2	-6.812	-10.748	10^{11}	2	3.802	-10.742
10^5	3	-5.414	-9.487	10^{11}	3	3.832	-9.454
10^5	5	-3.799	-6.785	10^{11}	5	3.907	-6.777
10^5	10	-1.787	-3.322	10^{11}	10	4.060	-3.300
10^5	15	-0.308	-2.198	10^{11}	15	4.319	-2.152
10^5	20	0.746	-1.681	10^{11}	20	4.600	-1.609
10^5	25	1.502	-1.402	10^{11}	25	4.819	-1.307
10^5	30	2.075	-1.236	10^{11}	30	4.981	-1.121

Table 3.5: Same as Table 3.4, but for ^{55}Mn.

ρY_e	T_9	EC	PE	ρY_e	T_9	EC	PE
10^2	0.7	-29.155	-36.954	10^8	0.7	-12.599	-36.954
10^2	1	-22.355	-28.101	10^8	1	-10.607	-28.101
10^2	1.5	-16.413	-21.208	10^8	1.5	-8.580	-21.206
10^2	2	-13.186	-17.668	10^8	2	-7.307	-17.661
10^2	3	-9.684	-13.436	10^8	3	-5.814	-13.427
10^2	5	-6.438	-9.331	10^8	5	-4.272	-9.314
10^2	10	-2.440	-5.911	10^8	10	-1.697	-5.868
10^2	15	-0.280	-4.798	10^8	15	-0.008	-4.759
10^2	20	1.034	-4.285	10^8	20	1.152	-4.260
10^2	25	1.922	-4.010	10^8	25	1.982	-3.993
10^2	30	2.571	-3.847	10^8	30	2.606	-3.836
10^5	0.7	-26.135	-36.954	10^{11}	0.7	4.010	-36.954
10^5	1	-20.296	-28.101	10^{11}	1	4.010	-28.101
10^5	1.5	-15.523	-21.206	10^{11}	1.5	4.010	-21.206
10^5	2	-12.863	-17.665	10^{11}	2	4.010	-17.661
10^5	3	-9.624	-13.434	10^{11}	3	4.014	-13.427
10^5	5	-6.428	-9.331	10^{11}	5	4.029	-9.314
10^5	10	-2.439	-5.911	10^{11}	10	4.152	-5.858
10^5	15	-0.279	-4.798	10^{11}	15	4.579	-4.707
10^5	20	1.035	-4.285	10^{11}	20	5.021	-4.163
10^5	25	1.922	-4.010	10^{11}	25	5.328	-3.862
10^5	30	2.571	-3.847	10^{11}	30	5.538	-3.681

3.4.3 Comparison of calculated EC rates with measured and previous theoretical results

The comparison of our computed stellar EC rates with *ground-state* EC reaction rates are displayed in Figs. 3.8 and 3.9. Fig. 3.8 shows the result of ^{45}Sc at stellar densities (10^7 and 10^9) gcm^{-3}, while similar results are depicted for ^{55}Mn in Fig. 3.9. In both figures we show the pn-QRPA calculated EC rates due to (i) 200 excited state GT distributions calculated by our pn-QRPA model and *ground state* (ii) measured GT strength distribution, (iii)

QRPA(M) computed transitions strength distribution, (iv) shell model (SM) (KB3G interaction) calculated GT strength distribution and (v) SM (GXPF1a interaction) calculated GT strength distribution. The corresponding references were stated earlier. Apart from the pn-QRPA data (where we microscopically calculate excited levels GT strength distributions), all EC rates were computed using only the ground state GT strength distributions and were adopted from Ref. [89]. The EC rates are plotted in $\log_{10}$ values (in units of s^{-1}) as a function of stellar temperature ($T_9 = 10^9$ K). On abscissa the range of temperature varies from (T_9 = 2–10). These regions of density and stellar temperature are important for stellar scenarios associated with silicon burning phases ($T_9 \sim 3$, $\rho\, Y_e \sim 10^7$ gcm^{-3}), for phenomena related to type-Ia supernova, up to pre-collapse of the core ($T_9 \sim 10$, $\rho\, Y_e \sim 10^9$ gcm^{-3}). For the case of ^{45}Sc, our computed weak-rates are in decent comparison with measured data. The enhancement comes because our calculation also takes into consideration GT transitions from parent excited states that show their effect at high T_9 values. The QRPA(M) rates are biggest because of calculation of big GT strength distribution (see Fig. 3.6). Shell model (SM) weak interaction rates are much smaller. It was reported in Ref. [89] that for the case of ^{45}Sc, largest discrepancy was noted between experimental data and shell model results.

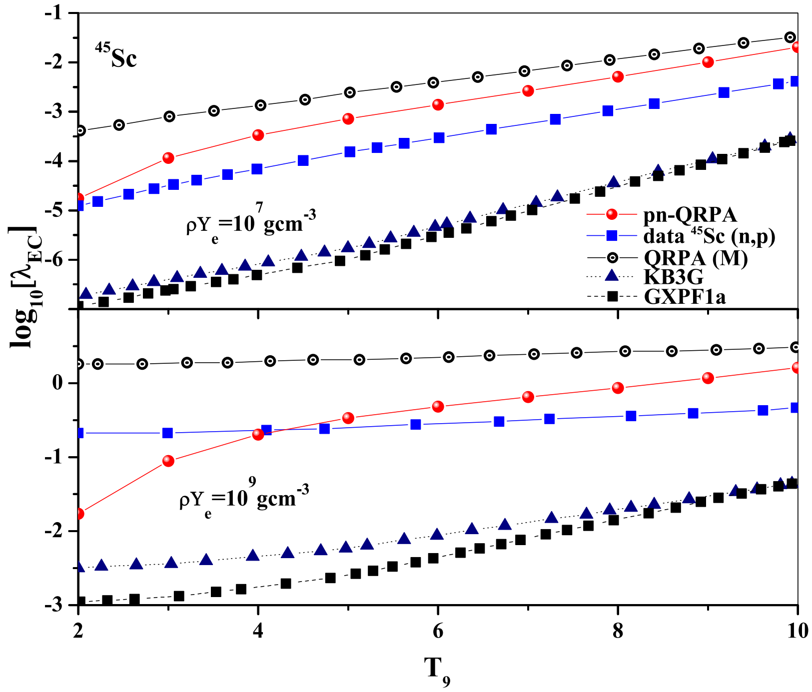

Figure 3.8: Comparison of pn-QRPA calculated electron capture rates on ^{45}Sc with measured and previously calculated rates. ρY_e show the stellar density, temperature (T_9) is given in units of 10^9 K and λ_{EC} represents the EC rates in units of s^{-1}. For references see text.

For the case of ^{55}Mn the theoretical estimates match rather well with experimental data (Fig. 3.9) at $\rho\ Y_e = 10^7$ gcm^{-3}. Only at high stellar temperature region our calculated weak-rates exceed experimental EC rates because of reason already stated. In high density regions once again the shell model rates are suppressed compared to experimental data. This is attributed to the calculation of smaller total Gamow-Teller strength values computed in the SM as compared to experimental transitions strength.

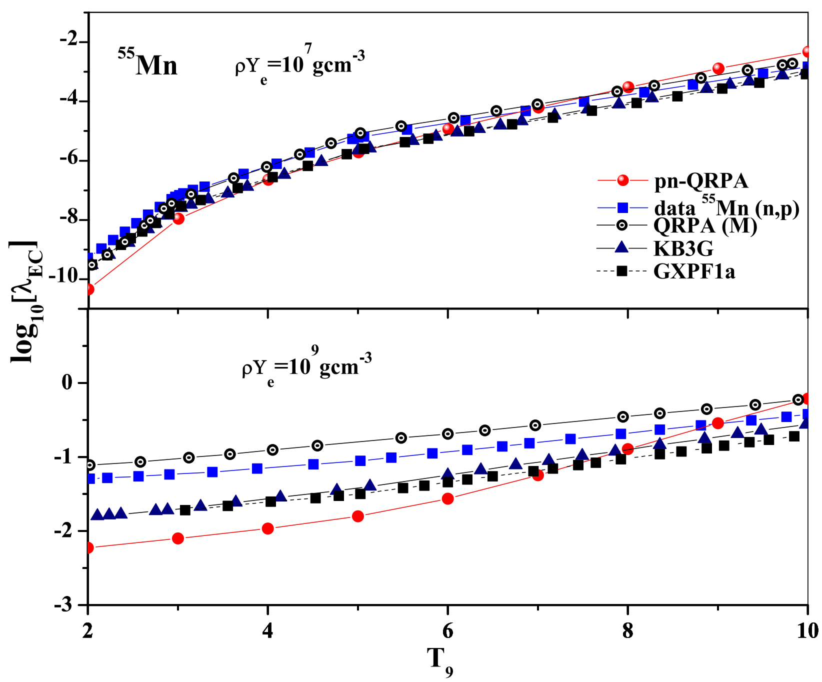

Figure 3.9: Same as Fig. 3.8, but for ^{55}Mn.

Next we compare the pn-QRPA calculated stellar EC rates with previous calculations of stellar EC rates. Excited parent states contribution were taken into consideration by the large scale shell model (LSSM) [98] and Independent Particle Model (IPM) [2] calculations. The IPM calculation was supplemented with measured transitions strength from β-decay reaction experiments. The mutual comparison is shown in Figs. 3.10 and 3.11. Both figures show three panels. The top panel depicts the comparison of calculated EC rates at stellar density $(\rho Y_e) = 10^4$ gcm^{-3} corresponding to low density region. The middle and bottom panels depict the comparison at stellar densities 10^8 gcm^{-3} and 10^{11} gcm^{-3}, respectively. These correspond, respectively, to medium and high density regions of the core. As discussed earlier that the results of pn-QRPA and LSSM models are microscopic in nature and show a more realistic image of the phenomena occurring in the astrophysical situations. The overall mutual comparisons show that at low temperatures pn-QRPA computed EC weak reaction rates are in decent accordance with LSSM computed weak-rates. However as the core temperatures rises, as the occupation possibility of excited levels are significant, our calculated EC weak-rates are bigger. In stellar matter these enhanced EC rates may have substantial impact during the late evolutionary stages of high mass stars. At high temperatures, the LSSM calculated values are too small as compared to other calculations. The Lanczos-based approach was used by LSSM, which is the main cause for this discrepancy and this was also pointed by Ref. [100].

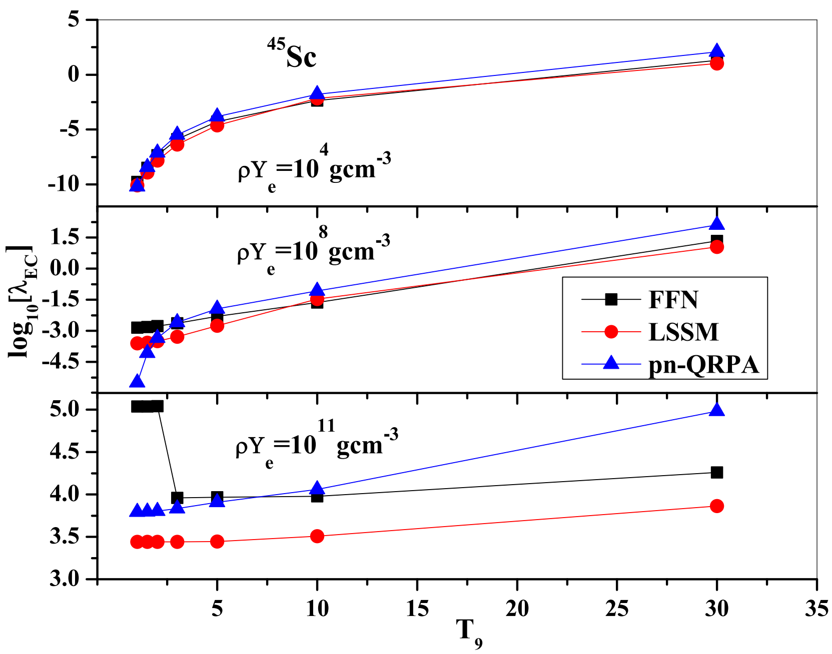

Figure 3.10: Comparison of pn-QRPA calculated electron capture (EC) rates on ^{45}Sc, with LSSM [98] and IPM [2] calculations. ρY_e show the stellar density, temperature (T_9) is given in units of 10^9 K and λ_{EC} represents the EC rates in units of s^{-1}.

Our pn-QRPA model incorporates a large model space of $5\hbar\omega$, which can efficiently handle all parent and daughter excited levels considered in this calculation. Another distinguishing feature of the current calculation is that we did not consider the Brink-Axel hypothesis (BAH) in our calculation of EC rates, used by IPM and LSSM calculations. We performed a state-by-state computation for EC rates from all parent to daughter levels in a microscopic way. It is suggested that core-collapse simulators may check the effect of our enhanced EC weak-rates. For the isotope of ^{55}Mn (Fig. 3.11), the shell model and pn-QRPA weak-rates are in decent agreement till T_9 = 10. This is due to the fact that ground-state rate commands the total EC rates for ^{55}Mn and both LSSM and pn-QRPA models performed a microscopic calculation of ground-state EC rates.

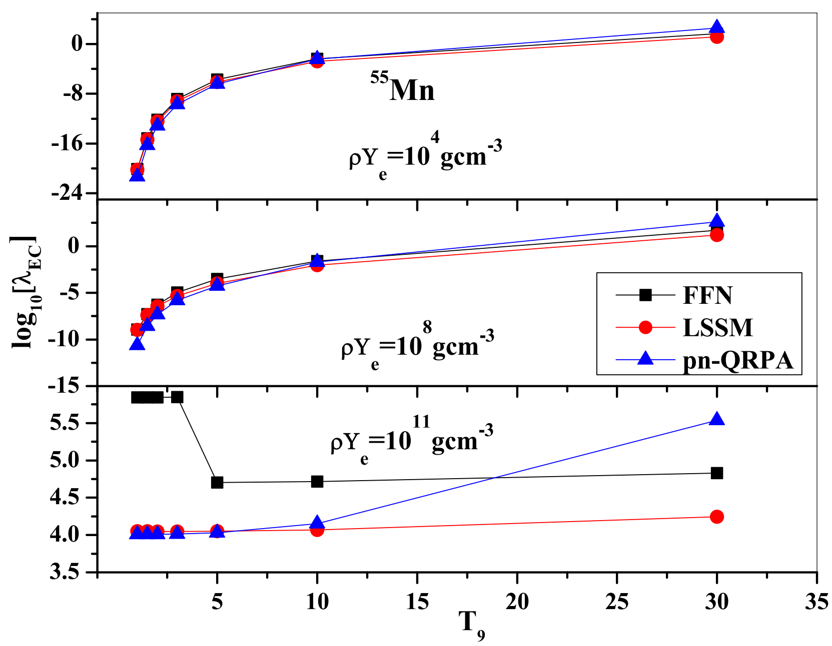

Figure 3.11: Same as Fig 3.10, but for ^{55}Mn.

3.5 Conclusions

Chromium isotopes are considered to play a crucial role thereby controlling the dynamics of stellar evolution of high mass stars. The EC weak reaction rates on Cr isotopes may be employed as a key input parameter in simulation codes. The stellar EC rates on chromium and odd-A isotopes are calculated. We considered a total of 100 parent and daughter excited levels (covered energy range was in excess of 10 MeV) for the microscopic prediction of these weak decay rates. Our model calculation reproduced well the measured half-life values and also fulfilled the Ikeda Sum Rule. Later we performed the calculation for weak-decay rates of chromium isotopes. We compared our results with the previous calculations of FFN and LSSM. Our calculated EC rates are enhanced in the presupernova era as compared to previous calculations and this is an interesting finding. From astral viewpoint these enhanced EC rates may have substantial impact on the late evolutionary stages of high mass stars and on the shock waves energetics. We urge supernova simulators may test run our calculated EC rates in their codes to search for probable interesting outcomes. β^+ decay rates are only important for $N \leq Z$ chromium isotopes up to stellar density of $10^7 gcm^{-3}$. For remaining chromium isotopes and higher temperature-density regions, the β^+ decay rates can safely be ignored.

Cole et al. [89] have presented a systematic evaluation of the capability of theoretical nuclear models to reproduce the measured GT strength of charge-exchange reactions in case of odd-A nuclei (^{45}Sc and ^{55}Mn) at intermediate energies. The authors have concluded that the GT charge-changing transitions calculated in the SM reproduce well the measured data, however the QRPA calculations [32] show larger deviations and overestimate the total experimental GT strength. It was also concluded that the SM calculated EC rates are in good agreement to the rates obtained from the measured GT strengths as compared to the QRPA approaches. The current study probes the conclusion of the Cole et al. study and provide useful information on the performance of QRPA-based models and refines the conclusions in Ref. [89]. Our findings show that this is not the case for all kind QRPA calculations.

Chapter 4

Lepton captures rates on nickel isotopes in stellar matter

4.1 Introduction

Majority of stellar processes posses a large number of exotic nuclide. Weak-decay transitions of these nuclei play a decisive part in astrophysical phenomena. Most of these exotic nuclei cannot be synthesized experimentally and theoretical estimates of weak-decay properties become more demanding to help us understand these stellar processes. The weak-rates are the crucial constituents to be identified in essentially all astrophysical processes [22]. The stellar evolutions and the associated nucleosynthesis have been the attention of much calculation [107]. At the later stage of burning cycles of massive stars, the iron core is developed by these stars and then no further nuclear fuel is available for ignition of a new cycle (any change of the tightly bound iron nuclide are endothermic). The stellar core gradually becomes unbalanced and collapses due to the capture of free electrons and photodisintegration. This collapse is much sensitive to the electron to-baryon fraction, and to the core entropy [7]. These parameters are governed by charge-changing transitions processes, i.e. β-decay and electron (positron) captures. The core collapse simulation greatly depends on the electron capture (EC) of heavier nuclei [6]. The nuclide which are situated in the Ni atomic mass range capture the electrons due to which the Y_e is reduced in the initial phase of collapse. The massive stars late evolutionary phases are intensely affected by charge-changing transition processes [82]. In these weak-decay reactions neutrinos are produced which, for stellar density ($\rho \leq 10^{11}$ gcm^{-3}), outflow from the stars carrying away entropy and energy from the core. At high density and temperature, heavy nuclei capture the electrons inside the stars thereby reducing the degeneracy pressure, and lead to the neutronization of stars. The EC importance for the collapse of presupernova stars were discussed in [108]. The positron captures (PC) are of crucial significance in astrophysical core, particularly in low density and high temperature regions. In these circumstances, a slightly higher positrons (e^+) concentration are produced via $e^-+e^+ \leftrightarrow \gamma + \gamma$ equilibrium state that favors the electron(positron) pairs. The race (and possibly the equilibrium) among PC and EC is a central constituent for the Type-II supernovae modeling (see e.g. [109]).

During the final evolution processes of high masses stars, EC (PC) and stellar β-weak-rates are controlled by Fermi and more significantly by GT transitions. The PC(EC) weak-rates are much related to the distributions of $GT_-(GT_+)$ transition strength. Protons are transformed into neutrons in the GT_+ transitions while conversely the GT_- strengths are accountable for transforming neutrons into protons. The total GT_+ charge-changing strengths are related to the EC strengths [110]. For *fp*-shell nuclei, the GT transitions strength are of fundamental importance for supernova physics [2]. In the stellar environment the nuclide are totally ionized so from the degenerate electron plasma the continuum EC occur. GT_+ strength on nuclei with ($A = 50 - 65$) were measured primarily through reactions of (n,p) at forward angles [42, 110, 111]. In contrast the GT_- transition functions were measured using the (p,n) reactions [112, 113]. Consequences of these experiments demonstrated that, as compared to the results of independent particle theory, the overall Gamow-Teller transitions are quenched and in the daughter nuclide split over several final levels. The residual interaction initiate these effects amongst the valence nucleons and the exact explanation of such correlations are necessary for the authentic evaluation of the astrophysical interaction processes because of the intense phase space energy dependence. Aufderheide and collaborators [64] have shown the intense stress on the significance of weak interaction rates in the Fe stellar core and the results of FFN are extended for heavier isotopes with mass greater than sixty. Later experimental data [111–113] showed the GT centroid misplacement used in the parametrization of FFN work [2] and afterward employed in the results of [64]. This triggered the efforts for the microscopic and precise prediction of astrophysical weak reactions rates. The shell model [65] and the pn-QRPA theories [39, 40] are the two most effective and widely employed models that are used for the accurate and microscopic computations of weak interaction processes. During the evolution of cores of high mass stars, weak-rates on nickel (Ni) isotopes are considered to play a consequential role in the evolutionary process. Several simulation results of massive stars displayed that EC and β-decay rates due to Ni isotopes alter significantly the ratio of Y_e of the stellar core (for detail refer to Refs. [64, 83]). The GT strength distribution and EC on ^{56}Ni, employing the deformed pn-QRPA model was first reported in Ref. [97]. The calculations were later extended to heavier isotopes of nickel $^{57-65}$Ni [114]. The situations where GT transitions are not favored, the first-forbidden (FF) strength become essential particularly in medium mass range and heavier nuclide. Mostly for heavier (neutron-rich) isotopes, the FF transitions phase-phase is amplified due to which these transitions are favored primarily. The GT and FF β-decay rates for heavier nickel isotopes with mass range 72 to 78, employing the same nuclear model, was later calculated by [41]. Further first-forbidden transitions (including rank 0, rank 1 and rank 2 contributions) for even-even nickel isotopes ^{72,74,76,78}Ni using different QRPA methods and related β-decay properties were recently reported [115]. However it was required to determine the GT charge-changing transitions and the associated stellar weak-interaction rates for remaining neutron-rich nickel isotopes $^{66-71}$Ni. In this chapter, we would like to discuss the GT distribution functions and the related lepton capture rates on neutron-rich Ni nuclide with mass range A = 66 – 71, using the deformed pn-QRPA model.

Capture rates on $^{66-71}$Ni isotopes were calculated for the following two processes:

i. Electron capture (EC)

$$^{66-71}Ni + e^{-} \longrightarrow ^{66-71} Co + \nu \tag{4.1}$$

ii. Positron capture (PC)

$$^{66-71}Ni + e^{+} \longrightarrow ^{66-71} Cu + \bar{\nu}. \tag{4.2}$$

4.2 GT strength distribution and ISR

The GT charge-changing strength distribution for the ground level of selected $^{66-71}$Ni isotopes are shown in Figs. 4.1 and 4.2. The charge-changing transitions for excited states are not presented because of space considerations. We considered around 100 states in daughter nuclei, up to excitation energy $\sim$ 45 MeV both for positron capture (PC) and electron capture (EC), respectively. GT transitions are central mode of excitation for the capture rates and β-decay throughout the presupernova evolution. Figs. 4.1 and 4.2 show the B(GT$_{\pm}$) strength functions for the selected $^{66-71}$Ni in GT$_{-}$ and GT$_{+}$ direction respectively. In Fig. 4.1 the abscissa shows the energy in the daughter $^{66-71}$Cu nuclide, while in Fig. 4.2 the abscissa denotes the energy in the daughter $^{66-71}$Co nuclide. The charge-changing transition are shown up to energy of 15 MeV in daughter nuclide. Experimental data was inserted in the calculation whenever probable. When the computed excitation energies were in the range of 0.5 MeV of one another then they were substituted with the experimental levels. The missing experimental levels were also introduced. The energy levels for which measured data had no particular parity and/or spin allocation, and beyond, were not substituted with the theoretical ones. It is to be noted that in this project forbidden transitions were not considered. We hope to calculate these forbidden transitions in near future. It is clear from Figs. 4.1 and 4.2 that the charge-changing transitions in daughter nuclide are well fragmented. It was observed that the calculated excited states transitions were much changed from the ground-level strength, which further suggest that the Brink-Axel hypothesis is not a good estimation to be used in the computations of astrophysical weak-decay processes of Ni nuclide. For nickel isotopes these excited states contribute mainly in the stellar weak-decay rates during the core contraction and collapse stages of high mass stars.

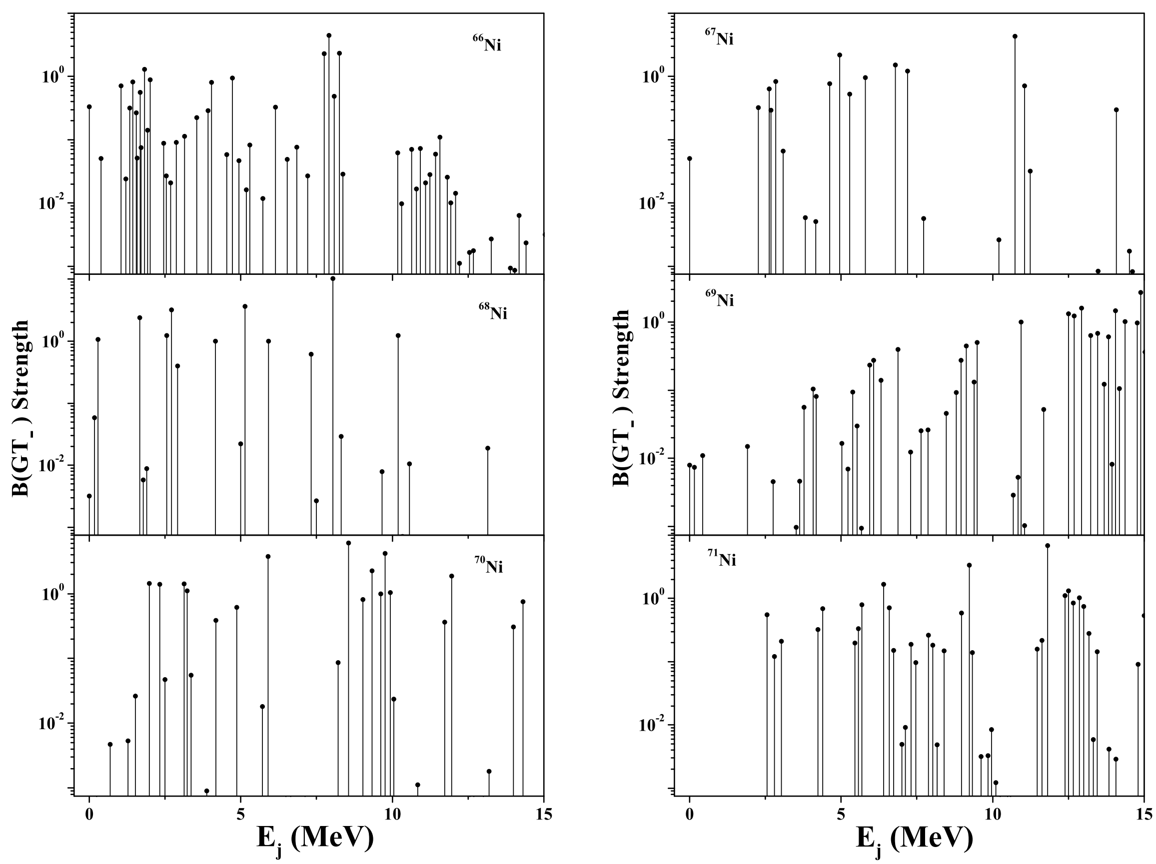

Figure 4.1: Calculated Gamow-Teller transitions as a function of daughter excitation energy (E_j) in positron capture direction using the pn-QRPA model.

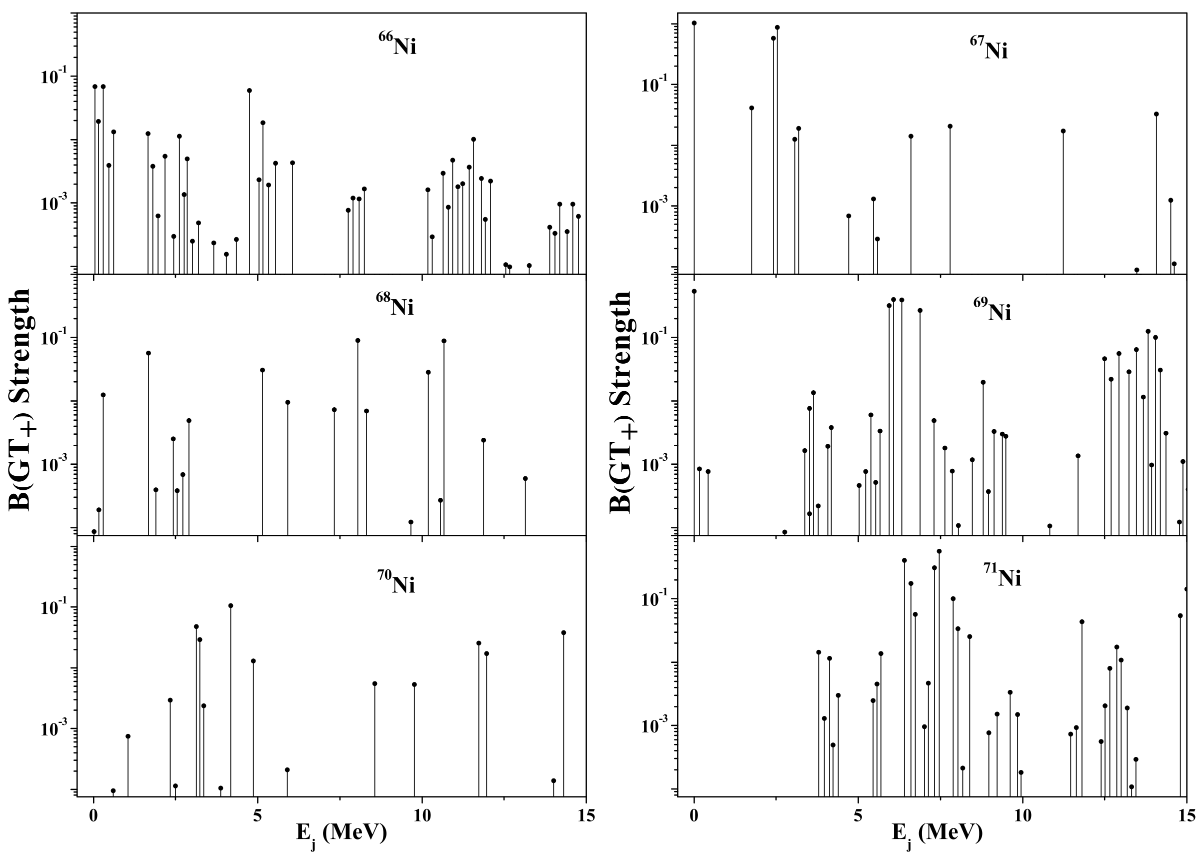

Figure 4.2: Calculated Gamow-Teller transitions as a function of daughter excitation energy (E_j) in electron capture direction using the pn-QRPA model.

The total GT$_\pm$ strengths are linked to the re-normalized Ikeda sum rule (ISR$_{re-norm}$) as

$$ISR_{re-norm} = \sum B(GT_-) - \sum B(GT_+) \cong 3f_q^2(N-Z). \tag{4.3}$$

Table 4.1 show that our calculated ISR$_{re-norm}$ values are in excellent accordance with the theoretical predictions. Thus the deformed pn-QRPA model well satisfied the model independent ISR.

Table 4.1: Comparison of (re-normalized) calculated and theoretical Ikeda sum rule of $^{66-71}$Ni.

A	N	$\sum$B(GT$_-$)	$\sum$B(GT$_+$)	Re-ISR$_{cal}$	Re-ISR$_{th}$	Cutoff energy in daughter (MeV)
66	38	11.11	0.31	10.80	10.80	7.76
67	39	14.45	2.59	11.87	11.88	13.59
68	40	13.09	0.13	12.96	12.96	7.32
69	41	16.52	2.49	14.02	14.04	14.88
70	42	15.32	0.21	15.12	15.12	8.56
71	43	17.98	1.78	16.19	16.20	11.81

4.3 Centroid and width

The energy dependence of Gamow-Teller strength is not known for several nuclide of potential importance in presupernova and core-collapse supernova. As discussed in previous chapter that the weak interaction rates are sensitive exponentially to the position of Gamow-Teller resonance, whereas the Gamow-Teller transitions change the astrophysical weak-rates in comparatively direct style [99]. Table 4.2 shows our calculated centroid ($\bar{E}$) and width for the calculated GT distributions along both β-decay and EC directions. These computed results are presented up to cutoff energy (E$_{cut}$) equal to 15 MeV in daughter nuclide. The values of $\bar{E}$ and widths are displayed in units of MeV.

Table 4.2: Calculated centroid ($\bar{E}_{\pm}$) and width$_{\pm}$ of Ni isotopes. The cutoff energy in daughter nuclei is 15 MeV.

Nuclei	$\bar{E}_{-}$ (MeV)	$\bar{E}_{+}$ (MeV)	Width$_{-}$ (MeV)	Width$_{+}$ (MeV)
^{66}Ni	5.56	2.90	3.01	3.48
^{67}Ni	7.21	1.77	3.15	2.09
^{68}Ni	5.57	7.13	2.91	3.47
^{69}Ni	12.50	6.35	2.70	4.39
^{70}Ni	7.80	6.53	3.18	4.20
^{71}Ni	9.95	8.03	3.04	2.62

4.4 Calculated β-decay half-lives

The deformed pn-QRPA computed beta decay half-lives ($T_{1/2}$) for heavier nickel nuclide were also compared with the measured $T_{1/2}$ values [95]. Table 4.3 shows the excellent comparison of our calculated and measured terrestrial $T_{1/2}$ values. The last column in Tab. 4.3 shows the nuclear deformation (β_2) values used in this work.

Table 4.3: The pn-QRPA calculated β-decay half-lives compared with the measured ones [95]. The last column shows the nuclear deformation (β_2) values used in this work.

Nuclei	$T_{1/2}$(cal) (s)	$T_{1/2}$(exp) (s)	β_2
^{66}Ni	210778.1	196560.0	-0.034
^{67}Ni	21.9	21.0	0.004
^{68}Ni	30.6	29.0	-0.004
^{69}Ni	11.5	11.5	-0.028
^{70}Ni	6.1	6.0	-0.004
^{71}Ni	2.7	2.6	0.016

4.5 pn-QRPA calculated lepton capture rates for $^{66-71}$Ni isotopes

The calculated EC and PC rates for $^{66-71}$Ni isotopes, as a function of astrophysical temperature, are depicted in Figs. 4.3 and 4.4, respectively. We present these captures rates at selected densities of 10^3 g/cm^3, 10^7 g/cm^3 and 10^{11} g/cm^3, corresponding to low, medium and high densities, respectively. The EC rates are on the rise as the stellar core density and temperature increase as can be seen from Fig. 4.3. This is because the increase in the stellar core density, rise the Fermi energy of the electrons, due to which enhancement in EC rates occur. In addition, as the stellar temperature soars the occupation probability of parent excited levels increases and contribute effectively to the total stellar weak-decay rates (Eq. 2.79). For all these neutron-rich nickel isotopes, the calculated positron emission rates are negligible and in the simulation codes these rates might be ignored when matched with the corresponding EC rates. The effects of PC for the stars having masses in the range ($10 \leq M_\odot \leq 40$) are estimated to be smaller and calculated to be bigger for more massive stars [83]. PC are considered to play an influential role in the evolutionary stages of stars. These rates decrease the pressure support of the electrons available in the astral core. The calculated PC rates are greater than the competing EE rates at high temperatures for all Ni isotopes. The PC rates for the selected Ni isotopes are shown in Fig. 4.4. It is observed that the PC rates increases as the stellar core temperature rises. The PC rates are similar for the densities in the range ($10 - 10^6$) gcm^{-3}. When the densities of the core increases beyond this range, decrement in the PC rate starts. In contrast to the EC rates, the PC rates reduce as the density of the core increases. As temperature increases or density decreases (at this stage for positrons the degeneracy parameter become negative), progressively positrons having very high-energy are generated which results in enhancement of PC rates.

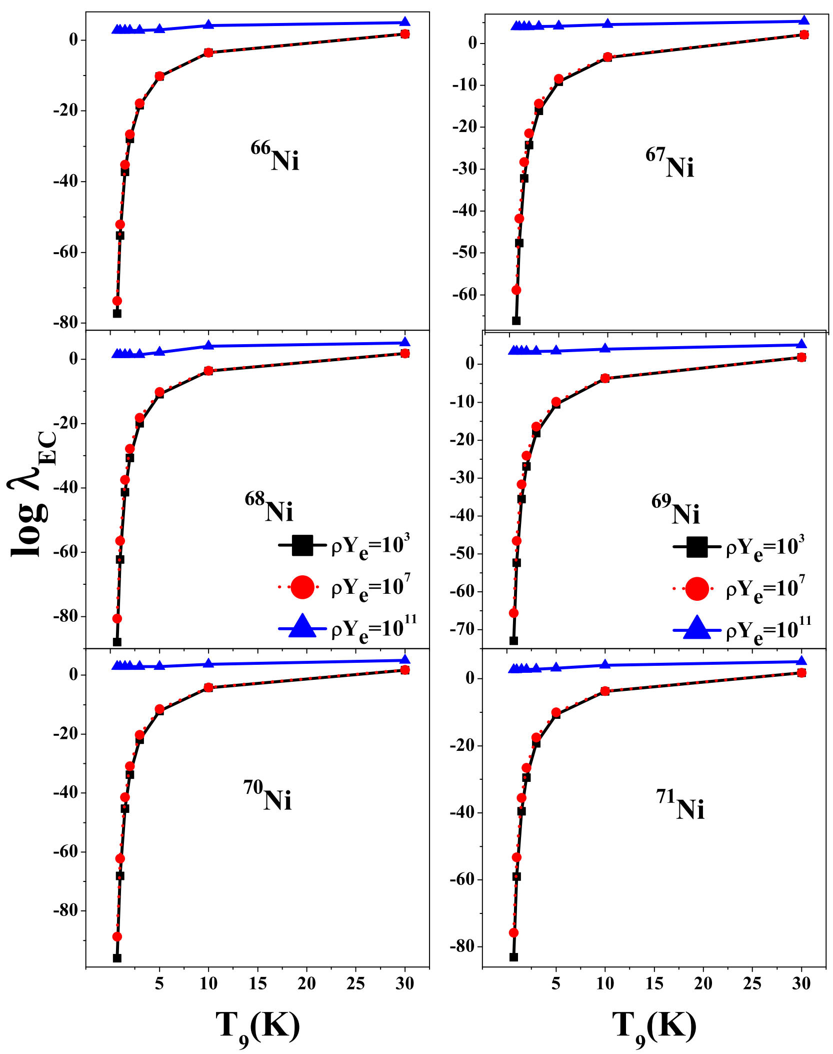

Figure 4.3: The pn-QRPA calculated EC rates on ($^{66-71}$Ni), as a function of stellar temperatures, for different selected densities. Temperatures (T_9) are given in units of 10^9 K. Stellar densities (ρY_e) are given in units of g/cm^3 and $\log \lambda_{EC}$ represents the log (to base 10) of EC rates in units of s^{-1}.

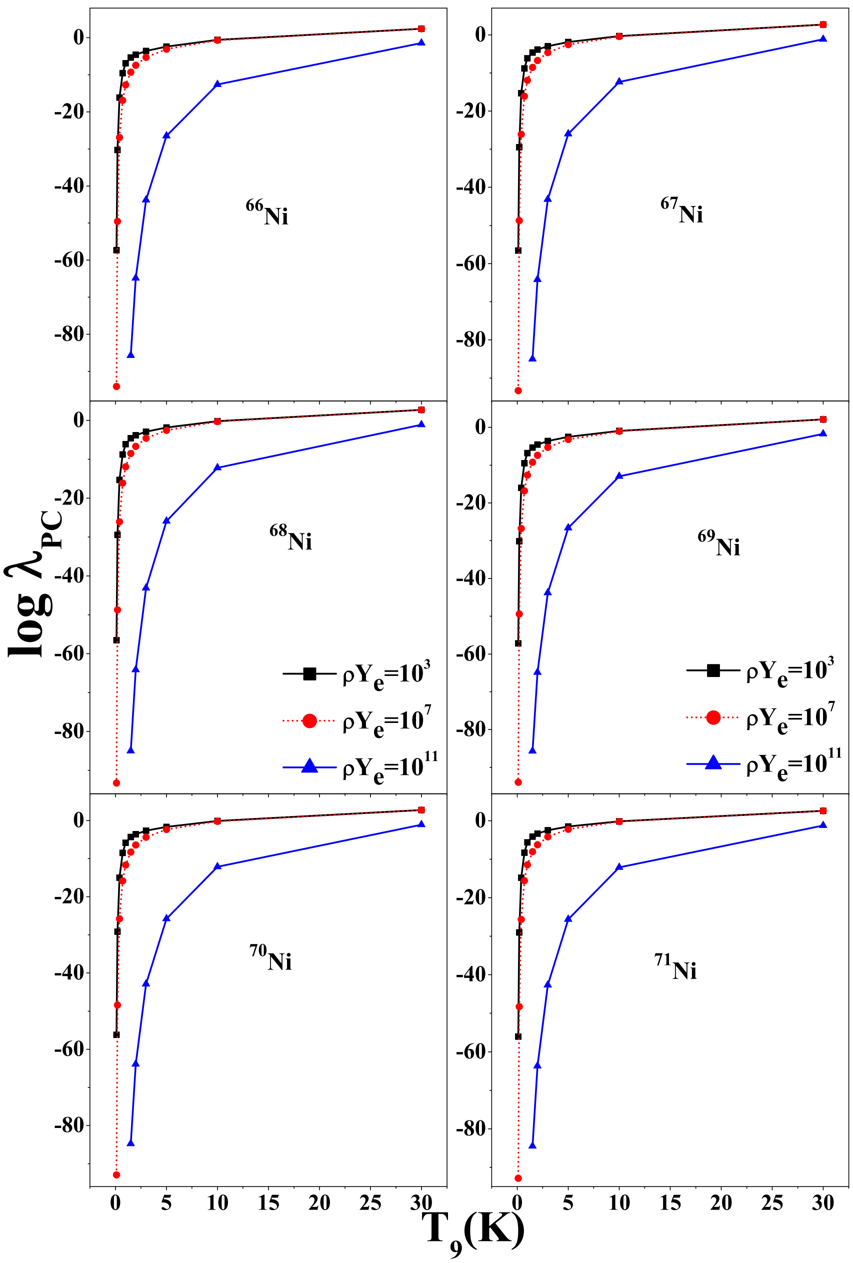

Figure 4.4: The pn-QRPA calculated PC rates on ($^{66-71}$Ni), as a function of stellar temperatures, for different selected densities. Temperatures (T$_9$) are given in units of 10^9 K. Stellar densities (ρY$_e$) are given in units of g/cm^3 and log λ_{PC} represents the log (to base 10) of PC rates in units of s^{-1}.

The deformed pn-QRPA computed EC and PC rates on $^{66-71}$Ni isotopes are presented on selected density-temperature scale in Tables 4.4 and 4.5. We present these capture rates for temperatures in the range $T_9 = 1 - 30$ and at selected densities (10^2, 10^5, 10^8 and 10^{11})g/cm^3. The calculated capture rates (Eq. 2.79) are displayed in log scale to the base 10. Tables 4.4 and 4.5 show that the capture rates increase as stellar temperature rises. At lower stellar temperature and density the EC rates are much smaller as compared to PC rates and can safely be neglected. But in high temperature and low density regions, EC rates compete rather well with the PC rates. It can also be seen from Tables 4.4 and 4.5 that in high stellar densities domain the PC rates are negligible as compared to EC rates, specially at low T_9.

Table 4.4: Calculated electron capture (EC) and positron capture (PC) rates on ^{66,67,68}Ni isotopes in stellar matter. The first column shows the stellar density (ρY_e) (in units of gcm^{-3}). T_9 states stellar temperature in units of 10^9 K. The calculated EC and PC rates are tabulated in logarithmic (to base 10) scale in units of s^{-1}. In the table, -100.00 means that the rate is smaller than 10^{-100}.

ρY_e	T_9	^{66}Ni		^{67}Ni		^{68}Ni	
		EC	PC	EC	PC	EC	PC
10^2	1	-55.47	-6.69	-47.82	-5.93	-62.51	-5.92
10^2	1.5	-37.21	-5.34	-32.25	-4.62	-41.43	-4.59
10^2	2	-27.91	-4.56	-24.28	-3.88	-30.75	-3.83
10^2	3	-18.37	-3.58	-16.06	-2.96	-19.90	-2.90
10^2	5	-10.30	-2.41	-9.15	-1.90	-10.92	-1.84
10^2	10	-3.53	-0.59	-3.34	-0.35	-3.69	-0.21
10^2	30	1.72	2.42	2.07	2.68	1.82	2.71
10^5	1	-53.41	-8.75	-45.76	-7.99	-60.43	-7.98
10^5	1.5	-36.32	-6.23	-31.36	-5.51	-40.54	-5.48
10^5	2	-27.59	-4.88	-23.96	-4.20	-30.43	-4.15
10^5	3	-18.31	-3.64	-16.00	-3.02	-19.84	-2.96
10^5	5	-10.29	-2.42	-9.14	-1.90	-10.91	-1.84
10^5	10	-3.53	-0.59	-3.34	-0.35	-3.69	-0.21
10^5	30	1.72	2.42	2.07	2.68	1.82	2.71
10^8	1	-43.25	-18.95	-35.57	-18.19	-50.23	-18.17
10^8	1.5	-29.09	-13.48	-24.11	-12.76	-33.28	-12.73
10^8	2	-21.86	-10.62	-18.22	-9.93	-24.69	-9.89
10^8	3	-14.42	-7.53	-12.10	-6.91	-15.94	-6.85
10^8	5	-8.09	-4.61	-6.94	-4.09	-8.71	-4.03
10^8	10	-2.78	-1.33	-2.59	-1.09	-2.94	-0.95
10^8	30	1.76	2.39	2.10	2.65	1.86	2.68
10^{11}	1	2.77	-100.00	3.97	-100.00	1.36	-100.00
10^{11}	1.5	2.77	-85.75	3.97	-85.03	1.36	-85.00
10^{11}	2	2.77	-64.86	3.97	-64.18	1.36	-64.13
10^{11}	3	2.77	-43.77	4.00	-43.15	1.37	-43.08
10^{11}	5	2.90	-26.50	4.13	-25.98	2.10	-25.92
10^{11}	10	4.11	-12.59	4.47	-12.35	4.03	-12.21
10^{11}	30	4.95	-1.44	5.32	-1.18	5.06	-1.15

Table 4.5: Same as Table 4.4, but for ^{69,70,71}Ni

ρY_e	T_9	^{69}Ni		^{70}Ni		^{71}Ni	
		EC	PC	EC	PC	EC	PC
10^2	1	-52.59	-6.63	-68.25	-5.64	-59.25	-5.41
10^2	1.5	-35.59	-5.30	-45.35	-4.33	-39.49	-4.11
10^2	2	-26.96	-4.53	-33.74	-3.59	-29.47	-3.37
10^2	3	-18.14	-3.59	-21.93	-2.69	-19.23	-2.49
10^2	5	-10.55	-2.51	-12.16	-1.69	-10.70	-1.51
10^2	10	-3.76	-0.96	-4.25	-0.14	-3.74	-0.14
10^2	30	1.86	2.13	1.74	2.75	1.82	2.59
10^5	1	-50.53	-7.66	-66.19	-7.70	-57.19	-7.47
10^5	1.5	-34.70	-5.46	-44.46	-5.22	-38.60	-5.00
10^5	2	-26.64	-4.57	-33.41	-3.91	-29.14	-3.69
10^5	3	-18.08	-3.59	-21.87	-2.75	-19.17	-2.55
10^5	5	-10.54	-2.51	-12.15	-1.70	-10.69	-1.52
10^5	10	-3.76	-0.96	-4.25	-0.15	-3.74	-0.14
10^5	30	1.86	2.13	1.74	2.75	1.82	2.59
10^8	1	-40.33	-18.89	-55.99	-17.90	-46.99	-17.67
10^8	1.5	-27.45	-13.45	-37.20	-12.47	-31.35	-12.25
10^8	2	-20.90	-10.59	-27.68	-9.65	-23.40	-9.43
10^8	3	-14.18	-7.54	-17.97	-6.64	-15.28	-6.44
10^8	5	-8.34	-4.70	-9.95	-3.88	-8.49	-3.71
10^8	10	-3.01	-1.70	-3.50	-0.88	-2.99	-0.88
10^8	30	1.90	2.09	1.78	2.72	1.86	2.56
10^{11}	1	3.40	-100.00	2.92	-100.00	2.68	-100.00
10^{11}	1.5	3.41	-85.71	2.92	-84.74	2.72	-84.51
10^{11}	2	3.42	-64.83	2.92	-63.89	2.78	-63.67
10^{11}	3	3.42	-43.77	2.92	-42.88	2.91	-42.67
10^{11}	5	3.45	-26.59	2.95	-25.77	3.12	-25.60
10^{11}	10	4.02	-12.95	3.64	-12.14	3.98	-12.13
10^{11}	30	5.11	-1.73	5.00	-1.10	5.06	-1.26

4.6 Comparison of lepton capture rates with previous calculation

We finally present the comparison of our computed EC and PC weak-rates on $^{66-71}$Ni with the earlier work of Pruet and Fuller (hereafter PF) [100]. The strategy adopted by PF for calculation of lepton capture rates was essentially the same as adopted by FFN (they also used independent particle model). The weak rates were split into two portions: a lower portion involving of discrete transitions amongst individual states whiles the high portion containing the Fermi and Gamow-Teller (GT) resonances. PF further attempted to remedy the misplacement of the GT centroid position by FFN and used a sophisticated treatment of nuclear partition functions in their calculation.

The comparisons presented here possibly will be of superior attention for core-collapse simulators. Figs. 4.5 and 4.6 show the comparison of our estimated EC rates results with those computed by PF. In comparing the EC rates, we illustrate three panels for each isotope of Ni. The upper panel is at stellar density 10 gcm^{-3}, the middle at 10^6 gcm^{-3} and bottom panel at 10^{11} gcm^{-3}, respectively. These stellar densities roughly resemble low, medium and high values. Figs. 4.5 and 4.6 display the comparison for ^{66,67}Ni and $^{68-71}$Ni, respectively. It is observed that at low as well as at medium densities and high temperatures, our EC rates values are larger than the corresponding PF calculated rates by maximum of two orders of magnitude. In high density and low temperature regions our calculated lepton capturing rates are in decent matching with PF, excluding the case of ^{68}Ni where PF calculated EC values are are larger than the deformed pn-QRPA values by an order of magnitude. At T_9 = 30, where the probability of parent excited levels increases considerably, our EC rates are greater by an order of magnitude from the corresponding rates values of PF.

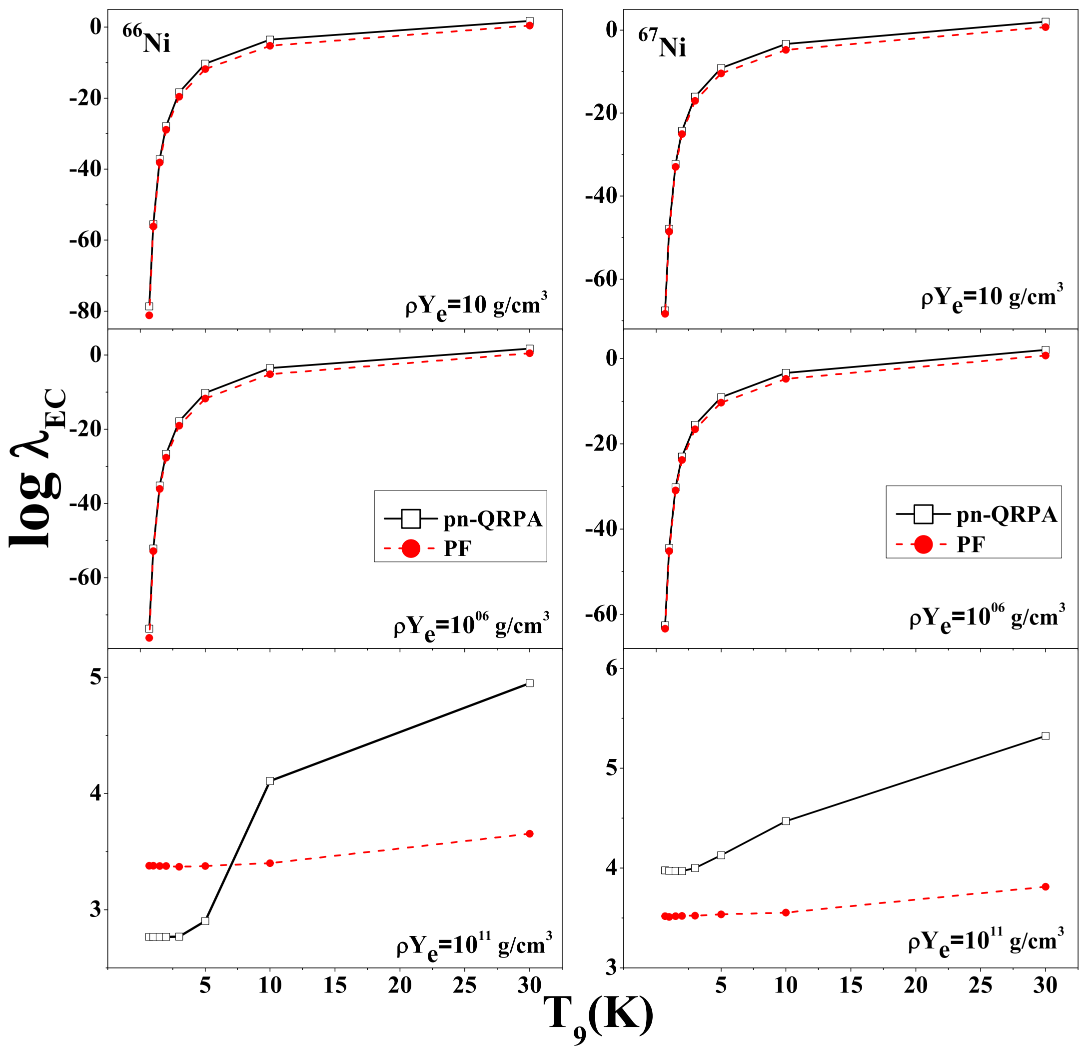

Figure 4.5: Comparison of pn-QRPA calculated EC rates (this work) with those calculated by PF [100]. Temperatures (T_9) are given in units of 10^9 K. Stellar densities (ρY_e) are given in units of g/cm^3 and $\log \lambda_{EC}$ represents the log (to base 10) of EC rates in units of s^{-1}.

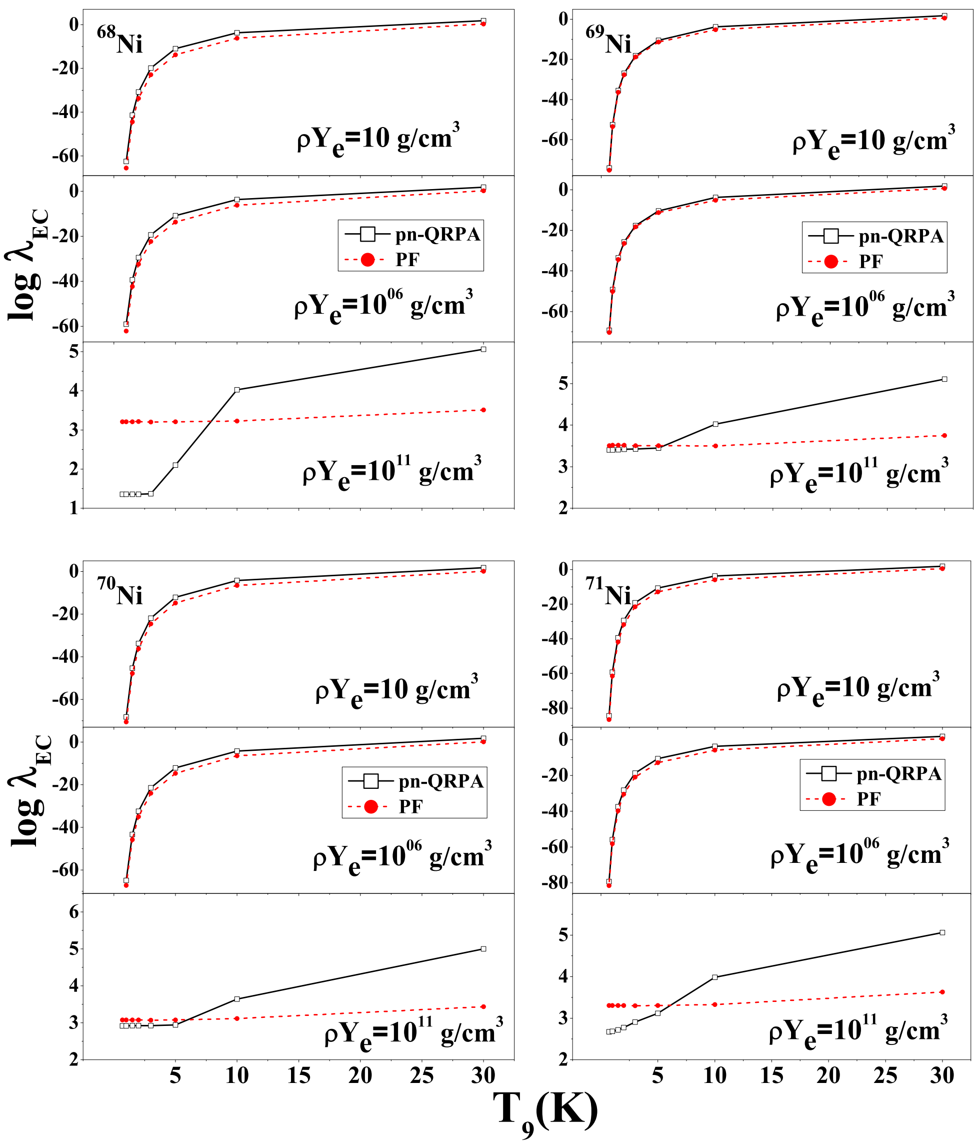

Figure 4.6: Same as Fig. 4.5, but for $^{68-71}$Ni.

The comparison between calculated PC and PF rates is also shown. But in order to save space, Fig. 4.7 displays the ratio of pn-QRPA computed PC rates to those computed by PF, R_{PC}(pn-QRPA/PF). It is noted that for $^{66-70}$Ni, in low temperature domains our rates are in good matching with PF calculations, whereas at high temperatures our computed rates are larger by more than an order of magnitude. For ^{71}Ni, even in low temperature regions, our calculated PC rates are greater by almost an order of magnitude. The enhancement of our lepton capture rates have many reasons. Primarily, the large model space was used in our calculations. In astrophysical environment the occupation of parent excited levels are likely probable and the transitions from such levels have predictable contributions to the lepton capture rates. As discussed previously, that the deformed pn-QRPA model has an extra benefit that it determined all the excited states charge-changing transition functions in a microscopic way. This means that the back resonances/and or Brink-Axel hypothesis, employed in the PF calculation, was not assumed in this work. Recent pn-QRPA calculations [114, 116] have shown that particularly at high stellar density and temperature the Brink-Axel hypothesis is poor estimation to be employed in the weak-decay rates calculation. The core-collapse simulators should take note of our bigger lepton capture rates on neutron-rich nickel isotopes.

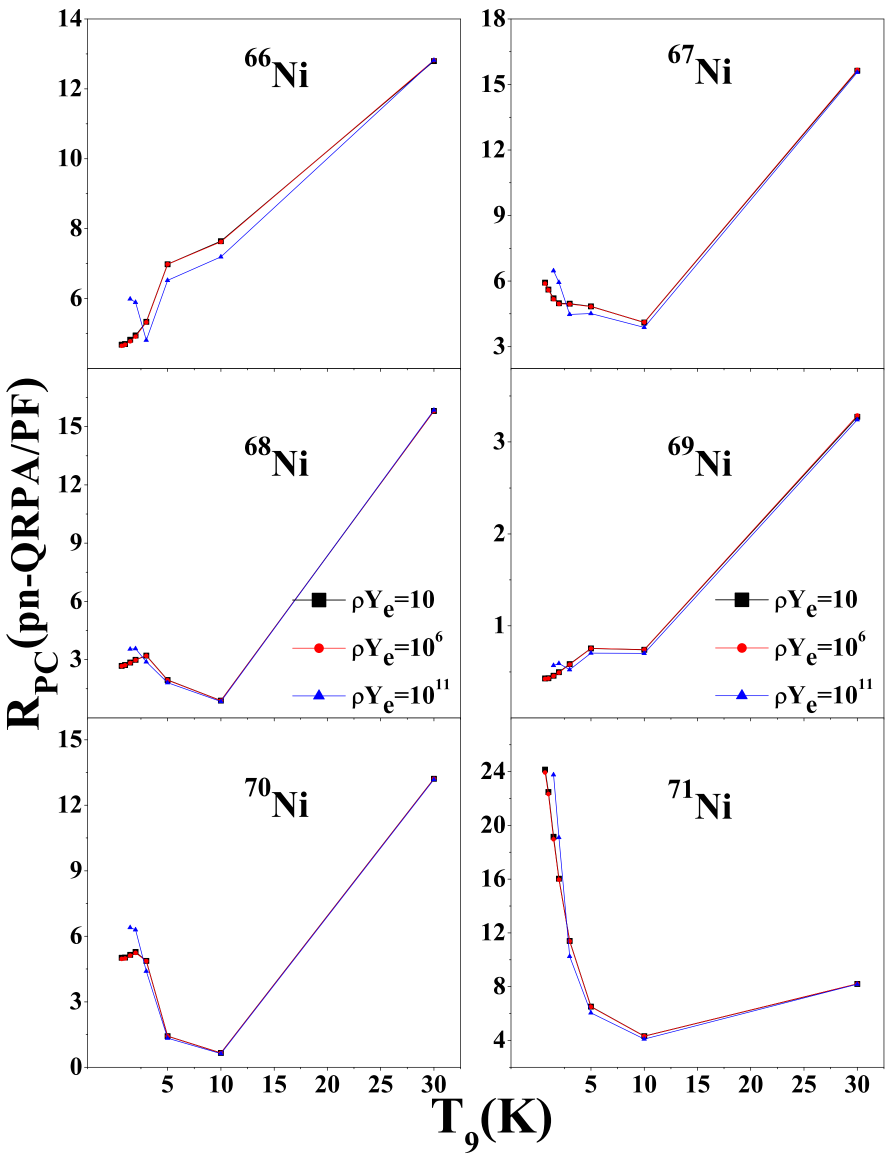

Figure 4.7: Ratio of reported PC rates to those calculated by PF [100] as a function of stellar temperature, for different selected densities. Temperatures (T_9) are given in units of 10^9 K and stellar densities (ρY_e) are given in units of g/cm^3.

4.7 Positron capture rates versus electron emission rates

Since both the PC and electron emission (EE) rates tend to increase the Y_e of stellar matter, one interesting query could be: how PC rates compete with the corresponding EE rates for these selected nickel isotopes (neutron-rich) in stellar core. Fig. 4.8 shows the percentage contribution of PC and EE to total weak-rates. The upper two bar graphs (a) and (b) are shown at low $T_9 = 2$ and high $T_9 = 30$, respectively, keeping the stellar density fixed at $\rho Y_e = 10^6$ g/cm^3. The bar graphs (c) and (d) are shown for low stellar density 10 g/cm^3 and high density 10^{11} g/cm^3, respectively, keeping the stellar temperature constant at $T_9 = 10$. From Fig. 4.8 it is clear that the contribution of PC to total rates is negligible at high density and low temperature domains. The contribution of PC rate to total weak rate is very large in high temperature regions. At T_9=10 and $\rho Y_e = 10$ g/cm^3, both the PC and EE rates compete with each other. One may conclude that in high density and low temperature regions, the contribution of PC values are much smaller as compared to EE values and may be neglected. However at high temperatures (late phases of massive stars evolution) the PC rates are the dominant mode for the stellar weak-rates.

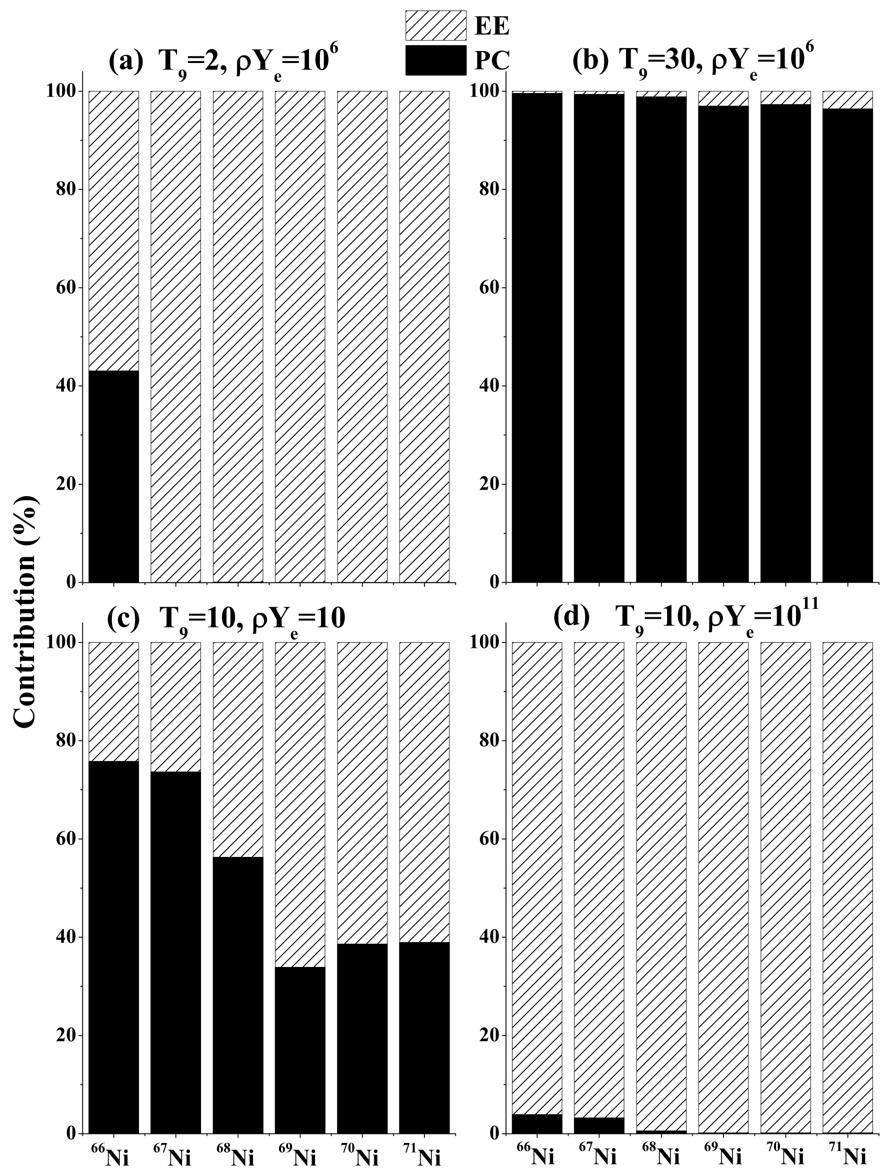

Figure 4.8: Percentage contribution of PC and electron emission (EE) rates to total weak-rates. Temperatures (T_9) are given in units of 10^9 K. Stellar densities (ρY_e) are given in units of g/cm^3.

4.8 Conclusions

The deformed pn-QRPA theory having the good track record of computing global half-lives values was employed to estimate the lepton (electron/positron) captures rates on cosmologically significant neutron-rich isotopes of Ni in stellar environment. The Ikeda sum rule which is consider to be model independent was fulfilled well in our calculation. The GT transitions, centroids and widths for all nickel isotopes, in both β-decay and EC directions, were also computed. The calculated ground and excited levels charge-changing transitions were then used for the computation of total weak reaction rates over wide-ranging stellar temperatures($T_9 = 0.01 - 30$)and densities ($10 - 10^{11}$ gcm^3) domain. We have noted that for these neutron-rich Ni isotopes, the EC rates are negligible as compared to PC rates in the domains of low temperatures and densities values, while in high density regions (10^{11} g/cm^3) the PC rates may safely be neglected. In low to medium stellar density and high temperature regions the EC rates compete well with the calculated PC rates.

The pn-QRPA calculated capture rates were also compared with previous calculation of Pruet and Fuller (PF). At high temperature and low density our EC rates were enhanced by as much as two orders of magnitude. In low temperature and high density regions the pn-QRPA calculated rates were in decent matching with the corresponding PF results (except for the case of ^{68}Ni). The possibility of parent excited levels increases as the stellar temperature rises, in these high temperature regions our calculated lepton captures rates values are greater than the PF rates. Supernova simulators may pay attention to our boosted lepton capture rates. One of the main reasons for the big differences in calculated lepton capture rates is that we compute excited states charge-changing transitions in a microscopic style without assuming the Brink-Axel hypothesis (used by PF). The deformed pn-QRPA model having a schematic and separable interaction offered the liberty of having a large model space equal to 7 $\hbar\omega$ suitable for the treatment of excited levels in heavier nuclei inside the stellar matter. Another reason could be the placement of centroids in PF and reported calculations. From astral viewpoint our enhanced lepton capture rates may have impact on the stellar evolution late stages and the shock waves energetics. Consequences of simulations illustrate that the lepton captures rates have a solid effect on the core collapse path as well as on the features of the core at bounce. It was also noted that in high density and low temperature regions, the PC rate contributions were much smaller as compared to electron emission (EE) rates. However at elevated temperatures the EE rates contribution to total rates can safely be neglected.

Chapter 5

Allowed and unique first-forbidden stellar weak-rates on heavy isotopes

5.1 Introduction

A precise understanding of the β-decay properties of heavy heavy nuclide is significant towards the understanding of supernova explosion, especially for the comprehension of the r-process mechanism. The elemental distribution on the r-process path are sensitive to the electron/positron emission characteristics, particularly for heavier isotopes (neutron-rich) taking part in these processes [117, 118]. Thousands of nuclei are present between the neutron drip line and the line of stability. In terrestrial laboratories majority of these nuclei cannot be synthesized and necessitates the theoretical calculation of nuclear structure and associated weak interaction properties for these unstable nuclei. The availability of electron-neutrino captures in the neutron-rich scenario greatly improves and amplifies the β-decay effects. The successive neutrino-induced neutron reactions also contribute by modifying the distribution shape of r-abundance pattern [119].

The nuclear weak interaction calculations of iron-regime and heavy nuclei are believed to be the key inputs and play a critical role in investigating several astrophysical phenomena.

These include, but are not limited to, the massive stars hydrostatic burning phases, the presupernova evolution process of high mass stars and nucleosynthesis processes like the r, s, p and rp -processes [12, 120]. It is well known that the weak-decay stellar reactions are governed by the Gamow-Teller (GT) and, to a lesser extent, by the Fermi transitions, for stellar densities $\rho \lesssim 10^{11} g.cm^{-3}$. In addition, for nuclei possessing chemical potential $\geq$ 30 MeV, situated in the region of stability line, the forbidden weak interaction transitions also contribute effectively for stellar densities $\rho \gtrsim 10^{11} g/cm^{3}$ [121]. The lepton capturing reactions are the important weak-decay processes throughout the course of presupernova stages of stellar core evolution. During the shell burning phases of silicon (Si), the electron emission (EE) rates cool down the star and thereby compete with the electron capturing process. During the Si burning phase, the EE rates are on the rise and this increasing rate has consequences. The EE reactions are considered an extra source for the neutrino production and this process cools the stellar core and reduces the core entropy. Beyond the silicon shell burning phases, the EE again contributes in cooling down the temperature of the stellar core. At very high stellar core densities, the allowed charge-changing transitions become insignificant. This is because of a substantial increase in the electron Fermi energy which consequently chokes the available phase space. For the heavier (neutron-rich) nuclei the first-forbidden (FF) transitions become significant as a larger phase space is available for such transitions. For the neutron-rich nuclei, precise and reliable estimations of β-decay half-lives ($T_{1/2}$) are crucial for a better understanding of late stages of stellar epoch and the nucleosynthesis processes (specially the r-process). Half-life estimates are required for the purpose of experimental investigation of nuclear properties and for designing purpose of future radioactive ion-beam experimental facilities.

Due to the scarcity of measured data, use of theoretical models became ever demanding for computation of weak-decay rates for majority of the unstable nuclei. Several nuclear models have been suggested and applied for the determination of the $T_{1/2}$ over the past decades. Special mentions would include the Statistical Gross Theory (SGT) [122], the pn-

QRPA model [34,35] and shell model calculation [123] (the last two models being microscopic in nature). Hybrid model, using the pn-QRPA model for GT and SGT for FF decays, was developed by [124] to perform the half-life calculation. Model calculations were also performed in which the ground level of the parent nucleus was determined by the Hartree-Fock-Bogoliubov (HFB) scheme using Skyrme force in a fully self-consistent pn-QRPA [125]. [126] used the DF3 + CQRPA (continuum QRPA) model and studied the contribution of allowed as well as FF transitions to total $T_{1/2}$ of r-process nuclide. It was concluded that the FF contribution was indeed small to total $T_{1/2}$ values for $A \leq 78$, but substantial for nuclei $A \geq 79$. Under terrestrial conditions, the microscopic investigations, employing the pn-QRPA model, for the allowed weak transitions were performed by [33–35] and for the unique first-forbidden (U1F) transitions by [36]. More recently [24] used the shell model and computed the allowed and FF contribution to the total $T_{1/2}$ of the r-process nuclide. [126] used the CQRPA model for the prediction of GT and U1F contribution to $T_{1/2}$ of heavier nuclide. However the Borzov results were limited only to spherical nuclei. Recently, authors in [127] measured the $T_{1/2}$ and branching ratios for neutron-rich nuclei and found that the deformation of nucleus can have a considerable effect on the half lives. Further to this there was a need to extend these calculations to finite temperature domain, in a microscopic fashion, in order to better comprehend the working mechanism of numerous astrophysical processes.

Recently the allowed Gamow-Teller (GT) and unique first-forbidden (U1F) electron emission rates of the selected neutron-rich Cu nuclide under stellar environment were presented [128]. There the authors concluded that, the calculated half-lives, including both GT and U1F contribution, were in good agreement with available experimental data. The EE rates (GT + U1F) were calculated over a wide range of temperature (T_9 = 0.01– 30) and density (10–10^{11} g/cm^3) scale. It was also concluded that, for $^{80-82}$Cu, a substantial part to the total β^--decay rates came from U1F strength, in line with the conclusion of Borzov [126]. The strength of U1F to total β^--decay rates decreases, when stellar density increases. However the lepton capture rates contribution, both allowed and U1F, were not calculated in [128]. The positron capture (PC) rates may compete with the EE rates under stellar conditions and the relative contribution to the total stellar weak-rates was also missing in [128].

In this chapter the lepton capture rates (GT and U1F) for selected copper isotopes having mass range 72 $\leq$ A $\leq$ 82 and the weak-decay rates for neutron rich odd-odd and even-even nuclei with mass range $70 \leq A \leq 214$ are presented. Motivation of the present calculations also came, in part, from the work of [36]. There the authors pointed out that the U1F transitions have a large impact on the total β-decay weak-rates. Homma and collaborators got better results, for their calculated $T_{1/2}$, using the deformed pn-QRPA theory [36]. However the non-unique FF transition contributions (rank 0 and rank 1) are also important and currently missing in our calculation. We plan to calculate non-unique FF transitions in future.

5.2 Allowed GT and U1F lepton capture rates for neutron-rich Cu isotopes

The allowed GT and U1F EC (λ_{EC}) and PC (λ_{PC}) rates, on Cu isotopes, are computed for a broad range of stellar temperature ($0.01 \times 10^9 \leq T(K) \leq 30 \times 10^9$) and density domain ($10 \leq \rho Y_e(gcm^{-3}) \leq 10^{11}$). Fig. 5.1 depicts the calculated EC rates on selected neutron-rich copper isotopes as function of astrophysical temperature. The calculated capture rates are shown at three different stellar density values of 10^3 gcm^{-3} (depicting low density regions), 10^7 gcm^{-3} (intermediate density regions) and 10^{10} gcm^{-3} (high density regions). The pn-QRPA calculated capture rates are given in logarithmic (to base 10) scales. We observe that the calculated EC rates, both allowed GT and U1F, increase as the stellar temperature and core density rise. Fig. 5.1 clearly show that the U1F capture weak-rates compete well with allowed GT capture rates and the two rates have orders of magnitude differences.

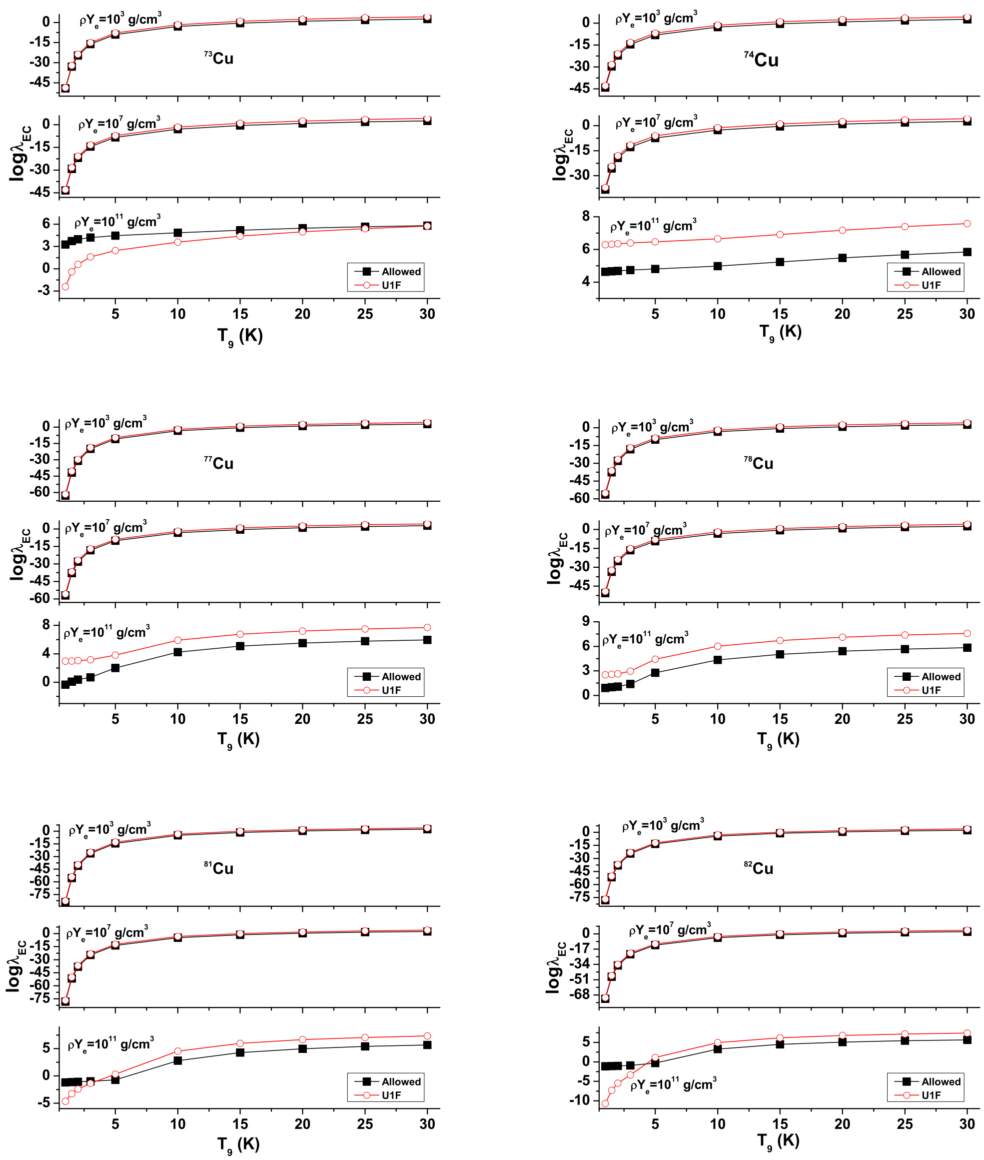

Figure 5.1: Calculated allowed and U1F electron capture (λ_{EC}) rates on ^{73,74,77,78,81,82}Cu in stellar matter as a function of stellar temperature (T_9) at selected stellar densities. The calculated capture rates are tabulated in logarithmic (to base 10) scale in units of s^{-1}

Fig. 5.2 shows similar result for pn-QRPA calculated PC rates on selected copper isotopes. Here one notes that the allowed GT and U1F rates are almost same and differ mostly at high stellar temperatures.

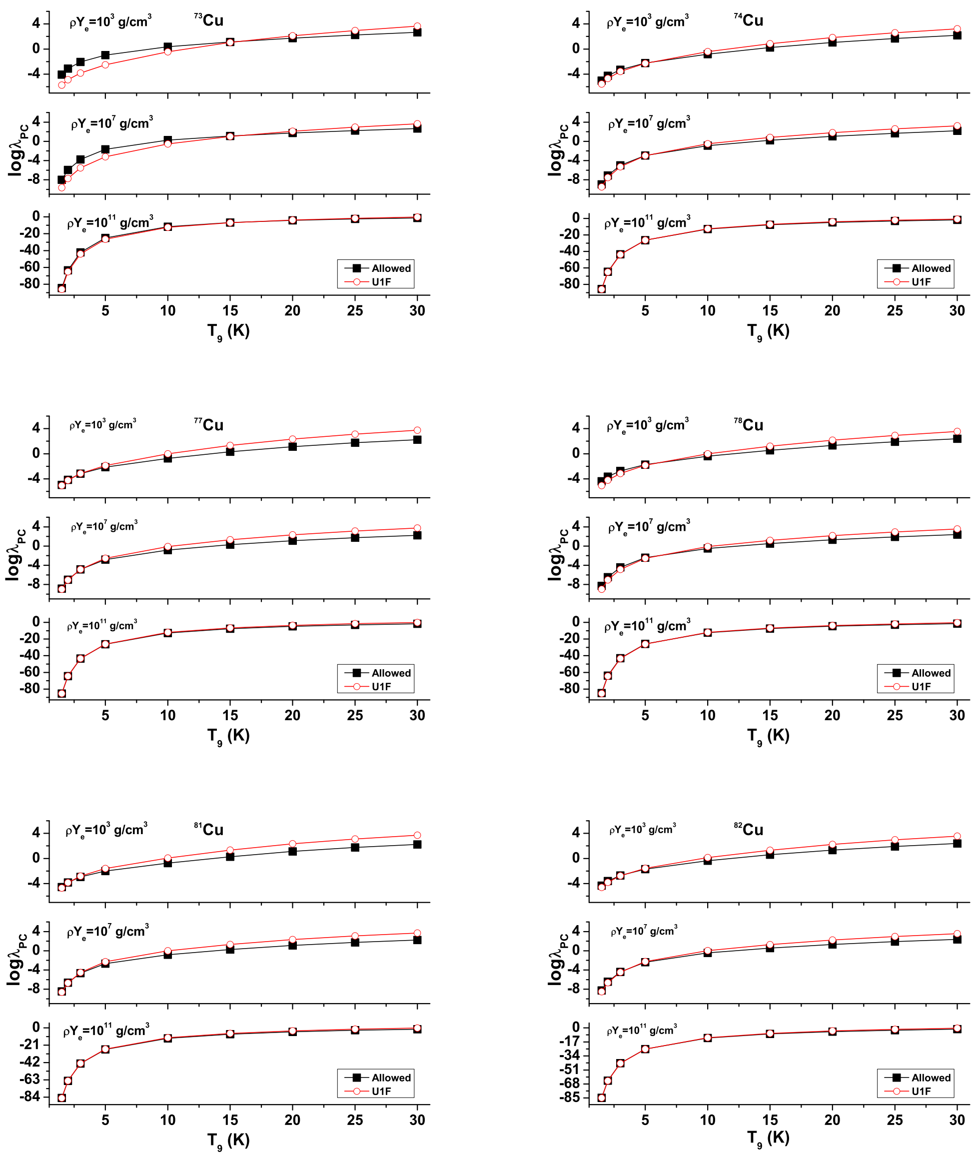

Figure 5.2: Same as Fig. 5.1, but for calculated positron capture rates (λ_{PC})

Tables 5.1, 5.2 and 5.3 show the calculated EC and PC rates for ^{72,73,75,76,79,80}Cu isotopes at selected temperature and density values. Once again all calculated rates are given in log to base 10 scales.

Table 5.1: Calculated allowed (GT) and unique first-forbidden (U1F) lepton capture rates on ^{72,73}Cu for different selected densities and temperatures in stellar matter. The first column shows the stellar density (ρY$_e$) (in units of gcm^{-3}). T$_9$ are given in units of 10^9 K. The calculated capture rates are tabulated in logarithmic (to base 10) scale in units of s^{-1}

ρY_e	T$_9$	^{72}Cu				^{73}Cu			
		λ_{PC} (GT)	λ_{EC} (GT)	λ_{PC} (U1F)	λ_{EC} (U1F)	λ_{PC} (GT)	λ_{EC} (GT)	λ_{PC} (U1F)	λ_{EC} (U1F)
10^2	1.5	-5.46	-30.00	-5.47	-28.75	-4.05	-33.03	-5.72	-32.19
	2	-4.68	-22.44	-4.58	-21.19	-3.11	-24.71	-4.88	-23.71
	3	-3.71	-14.69	-3.44	-13.42	-2.05	-16.20	-3.81	-15.06
	5	-2.63	-8.18	-2.08	-6.88	-0.96	-9.10	-2.51	-7.88
	10	-1.15	-2.74	-0.09	-1.37	0.36	-3.04	-0.44	-1.70
	15	-0.09	-0.48	1.27	0.96	1.14	-0.55	1.04	0.91
	20	0.74	0.90	2.28	2.39	1.74	0.89	2.12	2.44
	25	1.39	1.85	3.07	3.40	2.24	1.86	2.96	3.47
	30	1.90	2.55	3.73	4.15	2.66	2.57	3.66	4.23
10^6	1.5	-7.48	-27.98	-7.49	-26.73	-6.07	-31.00	-7.74	-30.16
	2	-5.96	-21.15	-5.87	-19.89	-4.40	-23.41	-6.17	-22.42
	3	-4.21	-14.18	-3.94	-12.91	-2.55	-15.70	-4.31	-14.56
	5	-2.72	-8.08	-2.17	-6.79	-1.05	-9.01	-2.60	-7.79
	10	-1.16	-2.73	-0.10	-1.36	0.35	-3.03	-0.45	-1.69
	15	-0.09	-0.47	1.26	0.96	1.14	-0.55	1.04	0.91
	20	0.74	0.90	2.28	2.40	1.74	0.89	2.12	2.44
	25	1.39	1.85	3.07	3.40	2.24	1.86	2.96	3.47
	30	1.90	2.55	3.73	4.15	2.66	2.57	3.66	4.23
10^{10}	1.5	-42.80	1.82	-42.80	3.15	-41.39	0.12	-43.06	-0.42
	2	-32.67	1.87	-32.57	3.20	-31.10	0.42	-32.87	0.59
	3	-22.35	1.96	-22.08	3.30	-20.69	0.83	-22.45	1.60
	5	-13.76	2.12	-13.22	3.47	-12.09	1.35	-13.65	2.45
	10	-6.62	2.52	-5.57	3.91	-5.11	2.23	-5.92	3.58
	15	-3.64	2.98	-2.30	4.43	-2.40	2.90	-2.52	4.38
	20	-1.82	3.41	-0.30	4.92	-0.82	3.40	-0.46	4.96
	25	-0.57	3.77	1.11	5.33	0.29	3.78	0.99	5.40
	30	0.37	4.06	2.20	5.67	1.14	4.08	2.13	5.75

Table 5.2: Same as Table 5.1, but for ^{75,76}Cu

ρY_e	T_9	^{75}Cu				^{76}Cu			
		λ_{PC} (GT)	λ_{EC} (GT)	λ_{PC} (U1F)	λ_{EC} (U1F)	λ_{PC} (GT)	λ_{EC} (GT)	λ_{PC} (U1F)	λ_{EC} (U1F)
10^2	1.5	-5.01	-38.87	-5.36	-37.96	-4.24	-34.30	-5.15	-33.06
	2	-4.27	-28.96	-4.53	-27.88	-3.42	-25.54	-4.30	-24.29
	3	-3.39	-18.81	-3.48	-17.58	-2.43	-16.61	-3.22	-15.35
	5	-2.41	-10.33	-2.19	-8.98	-1.35	-9.20	-1.91	-7.91
	10	-1.01	-3.36	-0.20	-1.89	0.04	-3.05	-0.05	-1.68
	15	0.04	-0.68	1.24	0.88	1.01	-0.53	1.22	0.89
	20	0.87	0.82	2.29	2.45	1.77	0.94	2.22	2.42
	25	1.51	1.82	3.08	3.50	2.35	1.92	3.00	3.47
	30	2.03	2.55	3.72	4.27	2.82	2.64	3.65	4.24
10^6	1.5	-7.03	-36.84	-7.39	-35.93	-6.26	-32.28	-7.18	-31.04
	2	-5.56	-27.67	-5.82	-26.59	-4.71	-24.24	-5.59	-23.00
	3	-3.89	-18.31	-3.98	-17.07	-2.92	-16.10	-3.72	-14.84
	5	-2.50	-10.24	-2.28	-8.89	-1.43	-9.11	-2.00	-7.82
	10	-1.02	-3.35	-0.21	-1.88	0.03	-3.04	-0.06	-1.67
	15	0.03	-0.68	1.24	0.88	1.00	-0.53	1.22	0.90
	20	0.87	0.82	2.29	2.45	1.77	0.94	2.22	2.43
	25	1.51	1.83	3.08	3.50	2.35	1.92	3.00	3.47
	30	2.03	2.55	3.72	4.27	2.82	2.64	3.65	4.24
10^{10}	1.5	-42.34	-6.89	-42.70	-6.43	-41.57	-2.98	-42.49	-1.66
	2	-32.27	-4.89	-32.52	-3.75	-31.41	-1.58	-32.30	-0.25
	3	-22.03	-2.32	-22.12	-1.01	-21.06	-0.16	-21.86	1.17
	5	-13.54	-0.11	-13.33	1.31	-12.48	1.01	-13.06	2.36
	10	-6.49	1.88	-5.68	3.38	-5.43	2.18	-5.53	3.58
	15	-3.52	2.76	-2.32	4.35	-2.54	2.91	-2.34	4.36
	20	-1.70	3.33	-0.29	4.97	-0.79	3.44	-0.36	4.95
	25	-0.44	3.74	1.12	5.43	0.41	3.84	1.04	5.40
	30	0.51	4.06	2.19	5.79	1.30	4.15	2.12	5.75

Table 5.3: Same as Table 5.1, but for ^{79,80}Cu

ρY_e	T_9	^{79}Cu				^{80}Cu			
		λ_{PC} (GT)	λ_{EC} (GT)	λ_{PC} (U1F)	λ_{EC} (U1F)	λ_{PC} (GT)	λ_{EC} (GT)	λ_{PC} (U1F)	λ_{EC} (U1F)
10^2	1.5	-4.36	-49.99	-4.97	-49.01	-4.37	-45.64	-4.76	-44.41
	2	-3.59	-36.98	-4.12	-35.91	-3.62	-33.81	-3.93	-32.57
	3	-2.67	-23.78	-3.05	-22.61	-2.72	-21.79	-2.88	-20.54
	5	-1.71	-12.90	-1.78	-11.63	-1.75	-11.88	-1.64	-10.60
	10	-0.42	-4.19	-0.04	-2.80	-0.48	-3.89	0.10	-2.53
	15	0.65	-0.98	1.25	0.47	0.44	-0.90	1.27	0.53
	20	1.48	0.75	2.28	2.24	1.19	0.73	2.21	2.22
	25	2.10	1.85	3.07	3.40	1.78	1.79	2.95	3.33
	30	2.58	2.64	3.70	4.23	2.25	2.54	3.56	4.14
10^6	1.5	-6.39	-47.96	-7.00	-46.99	-6.40	-43.61	-6.78	-42.38
	2	-4.87	-35.68	-5.41	-34.62	-4.91	-32.52	-5.22	-31.28
	3	-3.16	-23.27	-3.54	-22.11	-3.22	-21.29	-3.38	-20.04
	5	-1.80	-12.81	-1.87	-11.54	-1.84	-11.79	-1.73	-10.51
	10	-0.43	-4.18	-0.05	-2.79	-0.49	-3.88	0.09	-2.52
	15	0.65	-0.98	1.24	0.47	0.43	-0.90	1.27	0.53
	20	1.48	0.75	2.28	2.24	1.18	0.73	2.21	2.22
	25	2.10	1.85	3.07	3.40	1.77	1.79	2.95	3.33
	30	2.58	2.64	3.70	4.23	2.25	2.54	3.56	4.14
10^{10}	1.5	-41.70	-15.97	-42.31	-17.95	-41.71	-14.79	-42.10	-13.46
	2	-31.58	-12.07	-32.12	-12.12	-31.61	-10.18	-31.92	-8.85
	3	-21.30	-7.39	-21.69	-6.24	-21.35	-5.54	-21.52	-4.21
	5	-12.84	-2.76	-12.92	-1.43	-12.88	-1.77	-12.78	-0.42
	10	-5.88	1.02	-5.52	2.45	-5.94	1.32	-5.39	2.71
	15	-2.89	2.46	-2.32	3.93	-3.11	2.54	-2.29	3.99
	20	-1.07	3.25	-0.30	4.76	-1.37	3.23	-0.37	4.74
	25	0.16	3.77	1.11	5.33	-0.17	3.70	0.99	5.26
	30	1.06	4.14	2.16	5.74	0.73	4.04	2.02	5.65

5.3 Contribution of EE and PC rates to total rates

The ratio of electron to baryon (Y_e) increases as the electron emission (EE) (presented in [128]) and PC rates increase. Therefore one important query that may arise is how the two rates compete with each other for these neutron-rich copper isotopes. In Fig. 5.3 and

Fig. 5.4, the percentage contribution of EE and PC rates are shown. In Fig. 5.3, the allowed PC and EE rates are shown at $T_9 = 5$ (upper panels) and $T_9 = 30$ (lower panels). The left panels show the situation at low-to-medium density while the right panels depict the percentage contribution at high stellar density of 10^{11}gcm^{-3}. It is evident from Fig. 5.3 that PC rates must be taken into consideration at high stellar temperatures as they well dominate the competing EE rates for most of the copper isotopes.

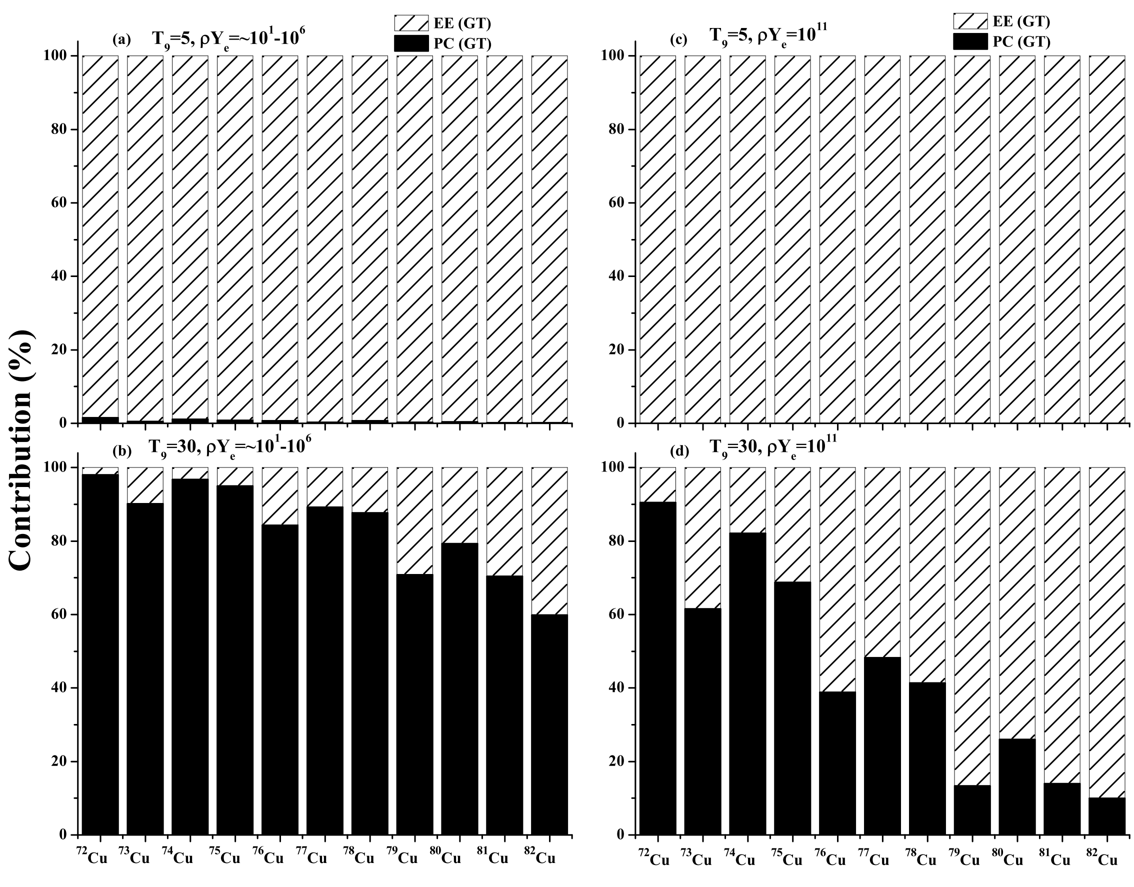

Figure 5.3: Percentage contribution of allowed positron capture and β-decay rates for neutron-rich copper isotopes. T_9 are given in units of 10^9 K. Stellar density, ρY_e, is given in units of g/cm^3

Fig. 5.4 shows analogous results for the U1F rates. At T_9 = 30, the calculated PC rates contribute almost 100% for all copper isotopes. For ^{72,73}Cu, even at T_9 = 5 and low-to-medium density regions, the PC contributes more than 50% to the total weak-rates. These findings are crucial and emphasize that EC and PC rates of copper isotopes need to be taken into account in all prespernova evolution simulation codes at high temperatures.

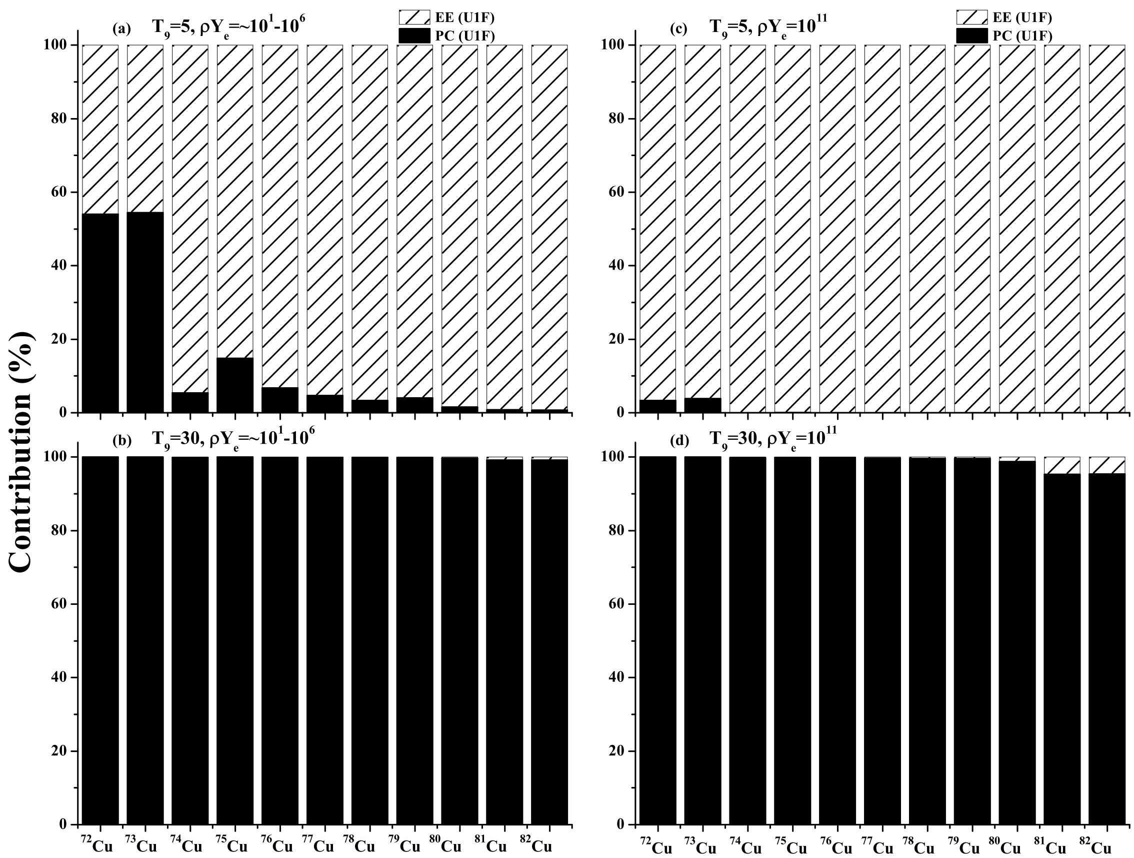

Figure 5.4: Same as Fig. 5.3, but for U1F rates

5.4 Comparison of pn-QRPA calculated U1F reduced matrix elements with experimental and previous theoretical calculation for heavy nuclei

Two different QRPA models were considered for the calculation of U1F reduced matrix elements of heavy nuclei. The first model i.e. pn-QRPA(WS) was applied only on the spherical nuclide, in which the Woods-Saxon potential basis was used and the U1F strength was computed. The detail formalism of pn-QRPA(WS) model can be seen in Ref. [129]. The second model is mentioned as pn-QRPA, in this model separable GT force with *ph*- and *pp*-channels was used and deformation of nuclei was considered. The calculations were performed for a total of 26 (22 odd-odd and 4 even-even) nuclei with mass range $70 \leq A \leq 214$. We begin the proceedings by comparing our calculated reduced matrix elements (for $\Delta J = 2$ transitions), within the pn-QRPA(WS) and pn-QRPA models, with extracted reduced matrix elements from experimental $logft$ values [130]. The results are shown in Table 5.4. It is to be noted that there are 29 entries in Table 5.4. This is because for ^{84}Rb, ^{102}Rh and ^{122}Sb, we calculate U1F transitions in both beta decay and EC directions. Our matrix elements are also compared with the calculated non-relativistic matrix elements taken from [131] and shown as RPA in seventh column of Table 5.4. The last two columns show our calculated matrix elements. The root mean square deviations for pn-QRPA(WS) and pn-QRPA calculated results are 0.1876 and 0.0966, respectively. Table 5.4 shows that the calculated reduced matrix elements of pn-QRPA model are in good matching with the experimental results. The pn-QRPA(WS) model computed matrix elements are in decent accordance with the measured values as compared to the correlated RPA values.

Table 5.4: Experimental and theoretical results for $\Delta J = 2$ first-forbidden β-decay transitions. The $\Delta J = 2$ $[I_i\ (I_f)\ = 2^-\ (0^+)]$ transition which have been considered are shown in the first two columns. The experimental log ft values [130] and the extracted reduced matrix elements are shown in columns three and four. The correlated RPA values of the reduced matrix elements [131] are shown in column seven while last two columns show the reduced matrix elements of pn-QRPA(WS) and pn-QRPA models, respectively.

N	Transition		$logft_{ex}$	$< I_f \| M^{U1F} \| I_i >_{ex}$	s-p transition		$< I_f \| M^{U1F} \| I_i >_{th}$ [fm]		
	initial	final		[fm]	proton	neutron	RPA	pn-QRPA(WS)	pn-QRPA
1	72As(2^-)	72Ge(0^+)	9.80	0.2029	$1f_{5/2}$	$1g_{9/2}$	0.4254	0.1720	0.2355
2	82Br(2^-)	82Kr(0^+)	8.90	0.5988	$1f_{5/2}$	$1g_{9/2}$	1.9297	0.5287	0.4546
3	84Br(2^-)	84Kr(0^+)	9.50	0.3106	$1f_{5/2}$	$1g_{9/2}$	1.3480	0.4404	0.2987
4	86Br(2^-)	86Kr(0^+)	9.07	0.3001	$2p_{3/2}$	$2d_{5/2}$	0.9642	0.4086	0.2864
5	84Rb(2^-)	84Sr(0^+)	9.40	0.3445	$1f_{5/2}$	$1g_{9/2}$	2.0324	0.5478	0.3904
6	84Rb(2^-)	84Kr(0^+)	9.50	0.3036	$1f_{5/2}$	$1g_{9/2}$	1.5500	0.3501	0.1651
7	86Rb(2^-)	86Sr(0^+)	9.40	0.3367	$1f_{5/2}$	$1g_{9/2}$	1.4530	0.4552	0.5019
8	88Rb(2^-)	88Sr(0^+)	9.20	0.4239	$2p_{1/2}$	$2d_{5/2}$	0.5150	0.4238	0.5147
9	90Y(2^-)	90Zr(0^+)	9.20	0.4239	$2p_{1/2}$	$2d_{5/2}$	1.2113	0.5330	0.4555
10	92Y(2^-)	92Zr(0^+)	9.20	0.3938	$2p_{1/2}$	$2d_{5/2}$	1.1722	0.4365	0.5804
11	94Y(2^-)	94Zr(0^+)	9.30	0.3778	$2p_{1/2}$	$2d_{5/2}$	1.0989	0.5136	0.1895
12	90Sr(0^+)	90Y(2^-)	9.40	0.1506	$2p_{1/2}$	$2d_{5/2}$	0.2395	0.1194	0.1454
13	92Sr(0^+)	92Y(2^-)	8.90	0.5995	$2p_{1/2}$	$2d_{5/2}$	0.3422	0.1788	0.5154
14	88Kr(0^+)	88Rb(2^-)	9.30	0.1690	$2p_{3/2}$	$2d_{5/2}$	0.0937	0.3365	0.1604
15	102Rh(2^-)	102Ru(0^+)	9.70	0.5588	$2p_{1/2}$	$2d_{5/2}$	0.4271	0.2111	0.6788
16	102Rh(2^-)	102Pd(0^+)	9.70	0.2439	$2p_{1/2}$	$2d_{5/2}$	1.0570	0.3438	0.2388
17	120I(2^-)	120Te(0^+)	9.30	0.3778	$1g_{7/2}$	$1h1_{1/2}$	1.8610	0.3720	0.2534
18	124I(2^-)	124Te(0^+)	9.30	0.3778	$1g_{7/2}$	$1h1_{1/2}$	2.7326	0.6150	0.3955
19	126I(2^-)	126Te(0^+)	9.13	0.4594	$1g_{7/2}$	$1h1_{1/2}$	3.1254	0.7230	0.4040
20	136I(2^-)	136Xe(0^+)	8.63	0.1487	$1g_{7/2}$	$1h1_{1/2}$	2.3621	0.4520	0.1313
21	122Sb(2^-)	122Sn(0^+)	8.90	0.5988	$1g_{7/2}$	$1h1_{1/2}$	3.2304	0.6453	0.6879
22	122Sb(2^-)	122Te(0^+)	8.60	0.2674	$1g_{7/2}$	$1h1_{1/2}$	1.7336	0.4680	0.2894
23	132La(2^-)	132Ba(0^+)	9.50	0.3001	$1g_{7/2}$	$1h1_{1/2}$	2.0986	0.4540	0.1961
24	140Ba(0^+)	140La(2^-)	8.82	0.2936	$1g_{7/2}$	$1h_{9/2}$	0.1944	0.4060	0.3069
25	142Pr(2^-)	142Nd(0^+)	8.90	0.5987	$1g_{7/2}$	$1h_{9/2}$	1.4403	0.4600	0.5743
26	198Au(2^-)	198Hg(0^+)	11.20	0.0119	$3s_{1/2}$	$3p_{7/2}$	0.0777	0.1880	0.0151
27	204Au(2^-)	204Hg(0^+)	8.50	0.9489	$2d_{7/2}$	$3p_{1/2}$	0.3660	0.6370	0.7151
28	198Tl(2^-)	198Hg(0^+)	9.00	0.1893	$3s_{1/2}$	$3p_{7/2}$	1.8409	0.4730	0.2585
29	204Tl(2^-)	204Pb(0^+)	10.10	0.1513	$1h_{9/2}$	$1i1_{7/2}$	0.8894	0.3370	0.1413

The calculated log ft values are compared with the measured values and with the theoretical calculation of [131] in Fig. 5.5. The figure shows that both QRPA model calculations are in decent agreement with the measured log ft values. The calculated $logft$ values by [131] are up to two orders of magnitude smaller than the measured data. The assumption in [131], that the relativistic β-moment is proportional to the matrix element of non-relativistic β-moment, is the major source of the orders of magnitude disagreement with the experimental data.

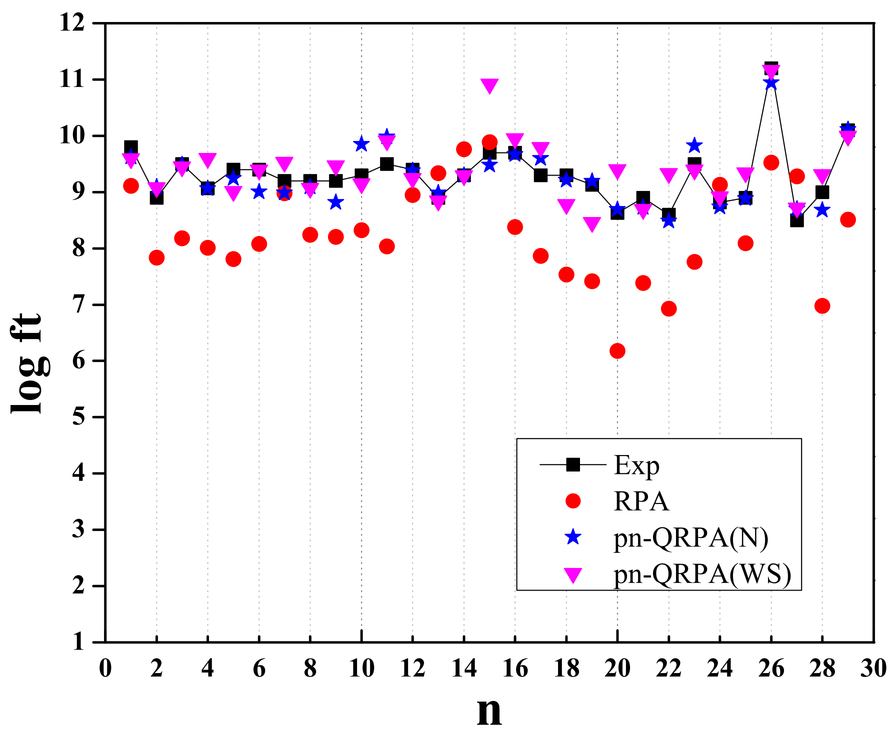

Figure 5.5: Experimental and theoretical *logft* values for $\Delta J = 2$ unique first-forbidden $\beta - decay$ transitions. The transitions are ordered in the same way as in Table 5.4. The solid line represents the experimental data [130]. RPA results are taken from [131].

5.5 Charge-changing strength distribution

The pn-QRPA model takes into account the nuclear deformation. This results in a fragmentation of β-decay strength distribution [34,35]. In order to improve the reliability of our calculated weak-rates, experimental data (XUNDL) were included in our pn-QRPA model calculation wherever possible. The UIF transitions for β-decay of ^{82}Br, ^{94}Y, ^{136}I and ^{204}Au using the pn-QRPA model are shown in Fig. 5.6. Here the abscissa represent the daughter excitation energy in units of MeV. Similarly Fig. 5.7 shows the calculated UIF transitions for electron capture (EC) of ^{72}As and ^{198}Tl. All U1F transitions are shown in units of fm^2 up to 30 MeV in daughter nuclei.

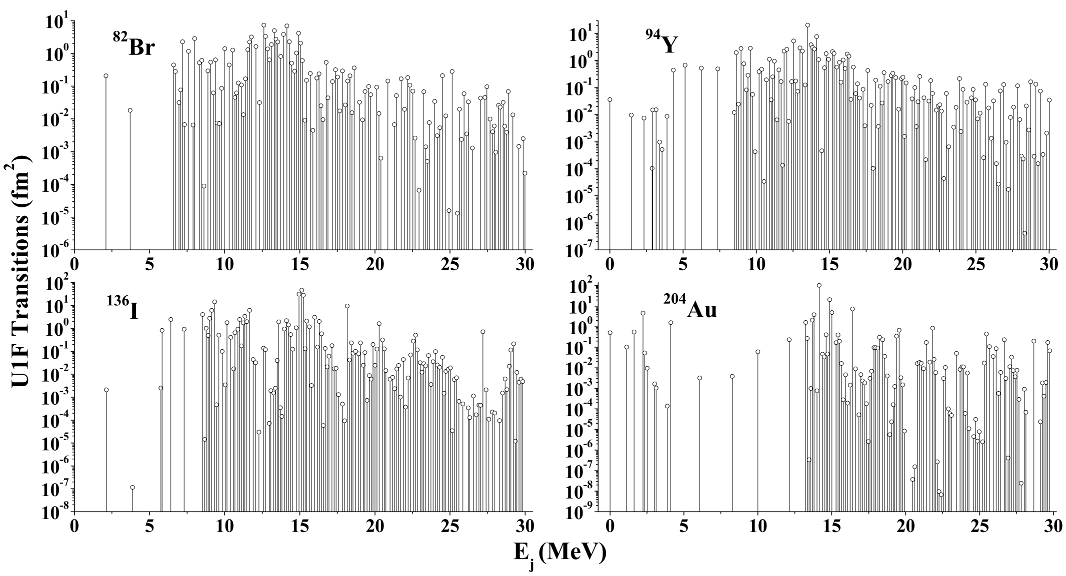

Figure 5.6: Calculated U1F transitions for selected nuclei in β-decay direction using the pn-QRPA model.

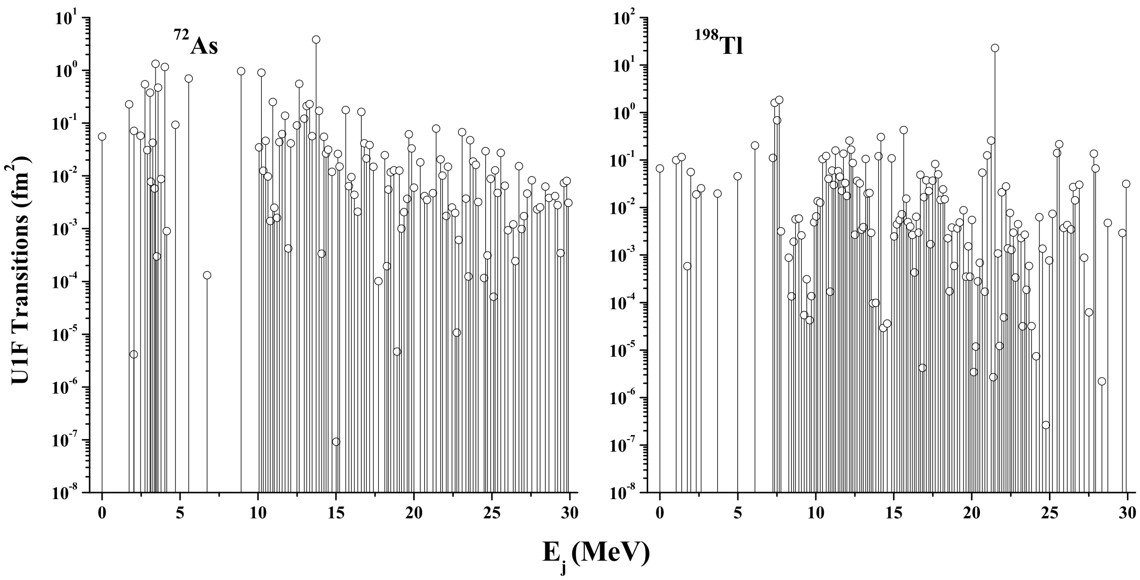

Figure 5.7: Calculated U1F transitions for selected nuclei in electron capture direction using the pn-QRPA model.

The calculated U1F transition strength for selected spherical nuclei (for which deformation (β) equal to zero) in EC and β-decay direction, using the pn-QRPA model are shown in Fig. 5.8. The calculated strength distributions for deformed nuclei are more fragmented than those calculated without the deformation. This means that the deformation results in the fragmentation of transition strength.

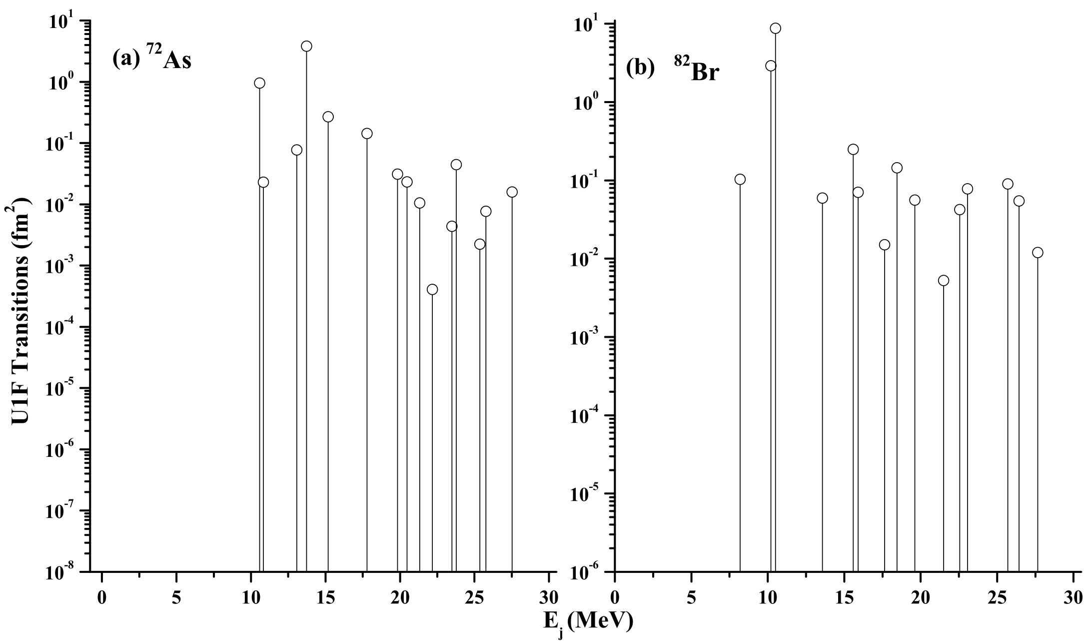

Figure 5.8: Calculated U1F transitions for selected spherical nuclei in (a) electron capture (b) β-decay direction using the pn-QRPA model.

5.6 Allowed and forbidden weak interaction rates

For the first time we calculate the allowed GT and U1F weak interaction rates for all heavy nuclei (shown in Fig. 5.4) using the pn-QRPA model in stellar environment. These include electron and positron emission rates as well as electron and positron capture rates. The weak-rate calculations were performed at stellar density range (10-10^{11})g/cm ^{3} and at stellar temperature in the range $0.01 \leq T_9 \leq 30$ (T_9 represents the stellar temperature in units of 10^9 K). We have plan to calculate also the beta-delayed neutron emission rates for heavier nuclei and which would be taken up as a future project. Tables 5.5 and 5.6 show the total allowed rates in β-decay direction (sum of positron capture (PC) and β^--decay rates) and the percentage contribution of β^--decay to total rate for 20 heavy nuclei. Table 5.7, on the other hand, shows the calculation of weak-rates along the electron capture direction (sum of electron capture (EC) and β^+-decay rates) for allowed transitions for 9 heavy nuclei. The corresponding U1F weak-rates calculation are shown in Tables (5.8-5.10). The rates are shown at selected densities (10^3, 10^7 and 10^{11}) g/cm^3 and at temperatures (1.5, 5, 10 and 30) GK. Tables 5.5 and 5.6 show that the sum of PC and β^--decay rates increases with increasing temperature, but decreases with increase in density. The growth of the stellar density suppresses the rates due to the availability of smaller phase space, whereas increase in temperature weakens the effect of Pauli blocking and consequently enhances the contribution of the GT_- transitions from excited levels of parent nucleus. As the temperature increases the PC rates contribution to the total rate also increases. This makes sense as positrons are produced only at high enough temperatures ($kT > 1$ MeV). At a fixed temperature the percentage contribution of β^--decay rates increases with increasing stellar density. For high stellar temperatures ($T_9 \geq 5$) our calculation shows that PC rates should not be neglected and contribute significantly to the total rates specially for low stellar densities. Regarding U1F transitions, at low stellar temperatures, the total rates are commanded by β^--decay and at high temperatures by PC rates (see Tables 5.8 and 5.9).

Tables 5.7 and 5.10 depict that the sum of EC and β^+-decay rates increases with increasing temperature and density. The weak-rates go up as the temperature increases because more excited levels contribute to the total rate as the stellar temperature rises. Also as the density and temperature of the core increase, the Fermi energy of electrons increases due to which enhancement of EC rates occurs. Consequently the contribution of EC rates to total weak-rates becomes very large at high density and temperature regions. It is seen from these tables that at T_9=30 the contribution of β^+-decay to total rates can safely be neglected.

Table 5.5: Allowed rates for different selected densities and temperatures. The second column gives stellar densities (ρY_e) having units of g/cm^3, where ρ is the baryon density and Y_e is the ratio of the electron number to the baryon number. Temperatures (T_9) are given in units of 10^9 K. λ_{total} shows sum of β^- and positron capture (PC) rates.

Nucleus	ρY_e	$\lambda_{total}(s^{-1})$				Percentage contribution of β^--decay			
		T_9=1.5	T_9=5	T_9=10	T_9=30	T_9=1.5	T_9=5	T_9=10	T_9=30
	10^3	7.22E-07	1.07E-03	8.93E-02	4.35E+02	6.15E+01	3.07E+01	1.55E+01	5.17E-02
^{82}Br	10^7	7.77E-08	4.30E-04	7.38E-02	4.32E+02	1.00E+02	6.52E+01	1.82E+01	5.20E-02
	10^{11}	1.55E-82	5.79E-26	3.05E-13	5.98E-02	1.00E+02	9.90E+01	7.53E+01	1.70E-01
	10^3	6.78E-05	5.36E-03	2.43E-01	5.77E+02	9.77E+01	6.20E+01	3.59E+01	2.77E-01
^{84}Br	10^7	1.02E-05	3.31E-03	2.10E-01	5.72E+02	1.00E+02	8.76E+01	4.07E+01	2.78E-01
	10^{11}	4.65E-77	2.62E-24	2.96E-12	8.03E-02	1.00E+02	9.99E+01	9.48E+01	1.04E+00
	10^3	1.77E-02	6.86E-02	7.25E-01	3.33E+02	1.00E+02	9.36E+01	6.64E+01	7.09E-01
^{86}Br	10^7	1.25E-02	6.04E-02	6.71E-01	3.30E+02	1.00E+02	9.85E+01	7.09E+01	7.14E-01
	10^{11}	2.02E-67	1.58E-21	6.31E-11	4.75E-02	1.00E+02	1.00E+02	9.96E+01	3.53E+00
	10^3	4.57E-05	3.91E-03	4.60E-01	1.65E+02	9.62E+01	3.88E+01	6.54E+01	1.99E+00
^{88}Kr	10^7	2.37E-05	1.92E-03	4.25E-01	1.64E+02	1.00E+02	7.50E+01	7.00E+01	2.00E+00
	10^{11}	4.17E-74	1.14E-22	5.29E-11	2.50E-02	1.00E+02	1.00E+02	9.97E+01	1.00E+01
	10^3	7.76E-12	5.15E-05	2.22E-02	2.90E+02	2.57E-01	9.15E+00	3.17E+00	6.68E-03
^{84}Rb	10^7	3.07E-15	1.30E-05	1.79E-02	2.88E+02	6.99E+01	2.86E+01	3.77E+00	6.71E-03
	10^{11}	5.17E-90	2.22E-28	2.69E-14	3.99E-02	9.94E+01	8.32E+01	2.14E+01	1.88E-02
	10^3	6.62E-10	1.52E-04	3.87E-02	3.73E+02	2.95E+01	2.34E+01	7.52E+00	1.20E-02
^{86}Rb	10^7	1.46E-11	5.26E-05	3.14E-02	3.70E+02	9.96E+01	5.61E+01	8.90E+00	1.21E-02
	10^{11}	1.04E-86	2.17E-27	6.13E-14	5.12E-02	1.00E+02	9.57E+01	4.23E+01	3.47E-02
	10^3	9.06E-04	1.48E-02	3.64E-01	6.52E+02	9.99E+01	9.06E+01	5.22E+01	2.47E-01
^{88}Rb	10^7	4.09E-04	1.25E-02	3.26E-01	6.47E+02	1.00E+02	9.77E+01	5.72E+01	2.48E-01
	10^{11}	1.19E-74	1.87E-23	6.48E-12	9.06E-02	1.00E+02	1.00E+02	9.73E+01	9.33E-01
	10^3	1.84E-09	5.92E-04	1.86E-01	1.85E+02	5.13E-02	6.41E+01	5.27E+01	6.64E-01
^{90}Sr	10^7	7.77E-13	3.97E-04	1.67E-01	1.83E+02	7.17E+01	8.94E+01	5.78E+01	6.68E-01
	10^{11}	2.44E-81	1.03E-24	4.08E-12	2.60E-02	1.00E+02	1.00E+02	9.79E+01	2.60E+00
	10^3	5.12E-05	2.11E-03	1.98E-01	8.05E+01	9.99E+01	8.82E+01	7.31E+01	1.09E+00
^{92}Sr	10^7	1.35E-05	1.82E-03	1.85E-01	7.98E+01	1.00E+02	9.73E+01	7.70E+01	1.10E+00
	10^{11}	8.32E-76	1.72E-23	1.01E-11	1.15E-02	1.00E+02	1.00E+02	9.95E+01	4.81E+00
	10^3	6.81E-09	3.20E-04	3.89E-02	3.78E+02	7.74E+00	5.88E+01	8.74E+00	7.06E-03
^{90}Y	10^7	1.69E-10	1.75E-04	3.15E-02	3.75E+02	9.96E+01	8.48E+01	1.02E+01	7.11E-03
	10^{11}	3.63E-85	4.16E-27	5.49E-14	5.19E-02	1.00E+02	9.74E+01	3.58E+01	1.86E-02

Table 5.6: Same as Table 5.5.

Nucleus	ρY_e	$\lambda_{total}(s^{-1})$				Percentage contribution of β^--decay			
		T_9=1.5	T_9=5	T_9=10	T_9=30	T_9=1.5	T_9=5	T_9=10	T_9=30
^{92}Y	10^3	1.03E-07	5.42E-03	1.60E-01	4.98E+02	9.63E+01	9.39E+01	3.82E+01	6.95E-02
	10^7	2.79E-08	4.50E-03	1.38E-01	4.95E+02	1.00E+02	9.85E+01	4.27E+01	6.98E-02
	10^{11}	6.47E-80	4.47E-25	6.97E-13	6.87E-02	1.00E+02	9.99E+01	8.58E+01	2.04E-01
^{94}Y	10^3	8.02E-04	1.22E-02	7.58E-02	1.24E+02	1.00E+02	9.60E+01	5.33E+01	1.84E-01
	10^7	5.06E-04	1.05E-02	6.76E-02	1.23E+02	1.00E+02	9.91E+01	5.80E+01	1.85E-01
	10^{11}	2.36E-75	2.35E-24	6.80E-13	1.72E-02	1.00E+02	1.00E+02	9.47E+01	5.99E-01
^{102}Rh	10^3	2.11E-09	1.44E-04	2.63E-01	1.11E+03	3.04E+00	2.63E+00	5.52E-01	5.26E-04
	10^7	1.36E-12	3.10E-05	3.29E-01	1.12E+03	8.21E+01	9.22E+00	6.61E-01	5.27E-04
	10^{11}	4.99E-88	2.57E-28	2.37E+05	1.05E+06	9.83E+01	5.58E+01	4.73E+00	1.55E-03
^{122}Sb	10^3	2.00E-06	1.95E-03	1.12E-01	5.22E+02	2.17E+01	2.50E+00	3.46E-01	3.07E-04
	10^7	8.20E-09	4.17E-04	8.97E-02	5.19E+02	9.77E+01	8.27E+00	4.11E-01	3.08E-04
	10^{11}	2.02E-84	2.82E-27	1.15E-13	7.16E-02	9.97E+01	4.52E+01	2.47E+00	8.41E-04
^{136}I	10^3	1.85E-02	5.72E-01	2.29E+00	1.19E+03	1.00E+02	9.85E+01	6.56E+01	2.45E-01
	10^7	1.30E-02	5.19E-01	2.10E+00	1.19E+03	1.00E+02	9.97E+01	7.00E+01	2.46E-01
	10^{11}	5.27E-70	2.77E-22	2.84E-11	1.66E-01	1.00E+02	1.00E+02	9.72E+01	8.12E-01
^{140}Ba	10^3	2.98E-09	8.54E-03	4.68E-01	3.52E+02	7.27E+01	9.56E+01	6.19E+01	2.97E-01
	10^7	1.35E-10	7.47E-03	4.25E-01	3.49E+02	9.99E+01	9.90E+01	6.64E+01	2.98E-01
	10^{11}	7.14E-80	2.34E-24	4.61E-12	4.88E-02	1.00E+02	1.00E+02	9.61E+01	9.55E-01
^{142}Pr	10^3	3.99E-06	1.06E-03	9.13E-02	6.00E+02	9.95E+01	2.75E+01	8.25E-01	2.63E-04
	10^7	1.49E-07	3.32E-04	7.31E-02	5.94E+02	1.00E+02	5.32E+01	9.59E-01	2.65E-04
	10^{11}	1.00E-83	2.47E-27	9.30E-14	8.20E-02	1.00E+02	7.46E+01	3.07E+00	6.34E-04
^{198}Au	10^3	9.87E-09	2.46E-04	6.25E-02	5.87E+02	3.90E+01	4.20E+00	2.01E-01	7.18E-05
	10^7	8.05E-11	5.49E-05	4.99E-02	5.83E+02	9.91E+01	1.44E+01	2.39E-01	7.19E-05
	10^{11}	3.81E-86	4.16E-28	6.22E-14	8.04E-02	9.99E+01	5.45E+01	1.14E+00	1.87E-04
^{204}Au	10^3	1.04E-05	3.53E-03	2.75E-01	1.21E+03	9.97E+01	6.01E+01	9.13E+00	6.56E-03
	10^7	1.26E-06	1.83E-03	2.23E-01	1.20E+03	1.00E+02	8.44E+01	1.06E+01	6.61E-03
	10^{11}	4.79E-77	4.37E-25	4.64E-13	1.66E-01	1.00E+02	9.97E+01	4.64E+01	1.79E-02
^{204}Tl	10^3	2.45E-12	2.30E-05	1.78E-02	3.72E+02	1.42E+01	2.01E+01	5.57E-01	1.07E-04
	10^7	1.22E-13	7.26E-06	1.43E-02	3.69E+02	9.98E+01	4.99E+01	6.62E-01	1.08E-04
	10^{11}	1.22E-87	1.29E-28	1.79E-14	5.07E-02	1.00E+02	8.87E+01	3.18E+00	2.82E-04

Table 5.7: Same as Table 5.5, but for electron capture (EC) direction. Here total rates include β^{+}-decay and electron capture rates.

Nucleus	ρY_e	$\lambda_{total}(s^{-1})$				Percentage contribution of EC			
		T_9=1.5	T_9=5	T_9=10	T_9=30	T_9=1.5	T_9=5	T_9=10	T_9=30
^{72}As	10^3	1.08E-05	5.37E-03	3.01E-01	4.34E+02	6.65E+01	9.58E+01	9.90E+01	1.00E+02
	10^7	6.30E-03	2.35E-02	3.75E-01	4.37E+02	9.99E+01	9.90E+01	9.92E+01	1.00E+02
	10^{11}	7.00E+04	8.05E+04	1.09E+05	4.02E+05	1.00E+02	1.00E+02	1.00E+02	1.00E+02
^{84}Rb	10^3	2.23E-08	1.15E-03	1.69E-01	7.43E+02	9.97E+01	9.96E+01	9.96E+01	1.00E+02
	10^7	4.06E-05	5.34E-03	2.10E-01	7.50E+02	1.00E+02	9.99E+01	9.97E+01	1.00E+02
	10^{11}	3.33E+04	6.64E+04	1.17E+05	7.89E+05	1.00E+02	1.00E+02	1.00E+02	1.00E+02
^{102}Rh	10^3	7.36E-08	1.44E-03	2.63E-01	1.11E+03	1.00E+02	9.96E+01	9.98E+01	1.00E+02
	10^7	2.69E-04	7.00E-03	3.29E-01	1.12E+03	1.00E+02	9.99E+01	9.99E+01	1.00E+02
	10^{11}	8.20E+04	1.42E+05	2.37E+05	1.05E+06	1.00E+02	1.00E+02	1.00E+02	1.00E+02
^{122}Sb	10^3	4.35E-09	7.21E-04	2.40E-01	1.29E+03	1.00E+02	9.98E+01	1.00E+02	1.00E+02
	10^7	2.00E-05	3.37E-03	3.00E-01	1.30E+03	1.00E+02	1.00E+02	1.00E+02	1.00E+02
	10^{11}	1.26E+05	1.80E+05	3.91E+05	1.52E+06	1.00E+02	1.00E+02	1.00E+02	1.00E+02
^{120}I	10^3	3.23E-04	1.64E-02	9.30E-01	6.93E+02	8.79E+00	9.05E+01	9.89E+01	1.00E+02
	10^7	1.88E-02	6.81E-02	1.16E+00	7.00E+02	9.84E+01	9.77E+01	9.91E+01	1.00E+02
	10^{11}	3.99E+04	6.00E+04	1.06E+05	3.77E+05	1.00E+02	1.00E+02	1.00E+02	1.00E+02
^{124}I	10^3	1.84E-06	5.35E-03	7.29E-01	1.38E+03	9.94E+01	9.92E+01	9.99E+01	1.00E+02
	10^7	1.78E-03	2.45E-02	9.11E-01	1.39E+03	1.00E+02	9.98E+01	9.99E+01	1.00E+02
	10^{11}	9.77E+04	1.58E+05	2.85E+05	1.01E+06	1.00E+02	1.00E+02	1.00E+02	1.00E+02
^{126}I	10^3	1.32E-07	1.84E-03	3.98E-01	1.11E+03	1.00E+02	9.97E+01	1.00E+02	1.00E+02
	10^7	2.64E-04	8.68E-03	4.98E-01	1.12E+03	1.00E+02	9.99E+01	1.00E+02	1.00E+02
	10^{11}	1.04E+05	1.46E+05	2.66E+05	9.40E+05	1.00E+02	1.00E+02	1.00E+02	1.00E+02
^{132}La	10^3	7.13E-05	9.51E-03	6.76E-01	6.56E+02	2.79E+01	9.57E+01	9.95E+01	1.00E+02
	10^7	1.39E-02	4.13E-02	8.43E-01	6.62E+02	9.96E+01	9.90E+01	9.96E+01	1.00E+02
	10^{11}	3.01E+04	4.15E+04	8.81E+04	3.69E+05	1.00E+02	1.00E+02	1.00E+02	1.00E+02
^{198}Tl	10^3	1.58E-07	9.60E-03	1.22E+00	8.20E+02	8.64E+01	9.84E+01	9.98E+01	1.00E+02
	10^7	1.18E-04	4.06E-02	1.51E+00	8.26E+02	1.00E+02	9.96E+01	9.98E+01	1.00E+02
	10^{11}	4.34E+04	5.79E+04	1.42E+05	3.79E+05	1.00E+02	1.00E+02	1.00E+02	1.00E+02

Table 5.8: Same as Table 5.5, but for U1F rates.

Nucleus	ρY_e	$\lambda_{total}(s^{-1})$				Percentage contribution of β^--decay			
		T_9=1.5	T_9=5	T_9=10	T_9=30	T_9=1.5	T_9=5	T_9=10	T_9=30
^{82}Br	10^3	7.08E-02	3.59E-02	5.46E-01	3.48E+04	1.00E+02	9.66E+01	2.93E+00	9.44E-06
	10^7	6.46E-02	3.28E-02	4.37E-01	3.46E+04	1.00E+02	9.93E+01	3.57E+00	9.48E-06
	10^{11}	1.46E-72	8.55E-24	7.64E-13	4.75E+00	1.00E+02	1.00E+02	3.24E+01	3.15E-05
^{84}Br	10^3	4.36E-01	1.72E-01	1.63E+00	5.35E+04	1.00E+02	9.83E+01	4.53E+00	2.86E-05
	10^7	4.24E-01	1.67E-01	1.31E+00	5.31E+04	1.00E+02	9.97E+01	5.55E+00	2.87E-05
	10^{11}	5.81E-67	7.11E-22	5.34E-12	7.31E+00	1.00E+02	1.00E+02	7.16E+01	1.26E-04
^{86}Br	10^3	5.01E+00	1.75E+00	7.52E+00	8.93E+04	1.00E+02	9.74E+01	1.07E+01	2.18E-04
	10^7	4.99E+00	1.70E+00	6.16E+00	8.87E+04	1.00E+02	9.95E+01	1.30E+01	2.19E-04
	10^{11}	1.82E-56	2.35E-18	5.46E-10	1.22E+01	1.00E+02	1.00E+02	9.88E+01	1.77E-03
^{88}Kr	10^3	1.64E-02	3.83E-02	3.11E+00	2.78E+04	1.00E+02	4.20E+01	4.21E-01	1.14E-05
	10^7	1.48E-02	1.94E-02	2.48E+00	2.75E+04	1.00E+02	7.72E+01	5.14E-01	1.15E-05
	10^{11}	9.95E-74	2.94E-24	3.23E-12	3.81E+00	1.00E+02	9.94E+01	5.50E+00	3.62E-05
^{84}Rb	10^3	4.53E-04	7.59E-04	1.38E-01	2.07E+04	9.97E+01	1.76E+01	3.87E-02	6.05E-08
	10^7	7.94E-05	2.18E-04	1.10E-01	2.05E+04	1.00E+02	4.23E+01	4.55E-02	6.08E-08
	10^{11}	4.86E-81	1.57E-27	1.35E-13	2.82E+00	1.00E+02	6.77E+01	1.51E-01	1.46E-07
^{86}Rb	10^3	7.13E-03	2.87E-03	2.39E-01	2.45E+04	1.00E+02	7.77E+01	3.97E-01	8.41E-07
	10^7	4.75E-03	2.00E-03	1.90E-01	2.43E+04	1.00E+02	9.36E+01	4.77E-01	8.47E-07
	10^{11}	1.92E-77	6.29E-26	2.38E-13	3.35E+00	1.00E+02	9.92E+01	2.51E+00	2.29E-06
^{88}Rb	10^3	1.50E+00	6.60E-01	2.77E+00	5.85E+04	1.00E+02	9.92E+01	1.17E+01	1.34E-04
	10^7	1.48E+00	6.45E-01	2.27E+00	5.81E+04	1.00E+02	9.98E+01	1.42E+01	1.35E-04
	10^{11}	2.28E-64	9.48E-21	3.14E-11	8.00E+00	1.00E+02	1.00E+02	9.24E+01	6.71E-04
^{90}Sr	10^3	6.06E-06	4.37E-03	2.47E+00	4.02E+04	9.85E+01	1.15E-01	1.51E-04	2.15E-09
	10^7	2.62E-07	8.68E-04	1.96E+00	3.99E+04	1.00E+02	3.54E-01	1.76E-04	2.16E-09
	10^{11}	1.14E-40	3.11E-14	2.41E-12	5.51E+00	1.00E+02	7.58E-01	5.05E-04	4.95E-09
^{92}Sr	10^3	2.01E-04	1.67E-03	6.31E-01	7.78E+03	1.00E+02	1.15E+01	3.33E-02	3.70E-06
	10^7	1.45E-04	4.57E-04	5.06E-01	7.73E+03	1.00E+02	3.60E+01	4.01E-02	3.72E-06
	10^{11}	1.67E-78	8.11E-27	7.11E-13	1.07E+00	1.00E+02	8.55E+01	2.26E-01	9.59E-06
^{90}Y	10^3	1.55E-02	6.65E-03	4.27E-01	3.81E+04	1.00E+02	9.15E+01	6.68E-01	1.89E-06
	10^7	1.25E-02	5.53E-03	3.41E-01	3.78E+04	1.00E+02	9.79E+01	8.12E-01	1.90E-06
	10^{11}	1.17E-75	3.77E-25	4.39E-13	5.20E+00	1.00E+02	9.99E+01	5.67E+00	5.53E-06

Table 5.9: Same as Table 5.5, but for U1F rates.

Nucleus	ρY_e	$\lambda_{total}(s^{-1})$				Percentage contribution of β^--decay			
		T_9=1.5	T_9=5	T_9=10	T_9=30	T_9=1.5	T_9=5	T_9=10	T_9=30
^{92}Y	10^3	3.72E-01	1.80E-01	1.20E+00	5.19E+04	1.00E+02	9.86E+01	7.45E+00	3.48E-05
	10^7	3.51E-01	1.71E-01	9.75E-01	5.15E+04	1.00E+02	9.97E+01	9.02E+00	3.49E-05
	10^{11}	3.58E-70	1.15E-22	3.17E-12	7.10E+00	1.00E+02	1.00E+02	6.57E+01	1.27E-04
^{94}Y	10^3	1.53E-01	7.81E-02	1.25E+00	6.25E+04	1.00E+02	9.85E+01	2.83E+00	1.22E-05
	10^7	1.50E-01	7.56E-02	1.01E+00	6.19E+04	1.00E+02	9.97E+01	3.50E+00	1.23E-05
	10^{11}	1.34E-66	5.25E-22	3.47E-12	8.53E+00	1.00E+02	1.00E+02	6.57E+01	5.66E-05
^{102}Rh	10^3	2.89E-05	2.94E-05	1.10E-01	2.79E+04	9.99E+01	3.71E+01	4.10E-03	3.66E-09
	10^7	9.59E-06	1.18E-05	8.73E-02	2.77E+04	1.00E+02	6.86E+01	4.86E-03	3.68E-09
	10^{11}	1.43E-81	1.36E-28	1.07E-13	3.80E+00	1.00E+02	8.90E+01	1.84E-02	9.14E-09
^{122}Sb	10^3	4.04E-04	1.62E-04	4.97E-01	6.90E+04	1.00E+02	7.38E+01	9.84E-03	1.69E-08
	10^7	2.92E-04	1.11E-04	3.95E-01	6.85E+04	1.00E+02	9.24E+01	1.19E-02	1.70E-08
	10^{11}	4.05E-78	4.53E-27	4.85E-13	9.42E+00	1.00E+02	9.93E+01	7.16E-02	4.72E-08
^{136}I	10^3	7.78E-01	2.45E-01	1.18E+01	1.15E+05	1.00E+02	8.57E+01	7.74E-01	2.14E-05
	10^7	7.71E-01	2.15E-01	9.45E+00	1.14E+05	1.00E+02	9.68E+01	9.63E-01	2.15E-05
	10^{11}	1.09E-59	6.30E-20	4.22E-11	1.57E+01	1.00E+02	1.00E+02	7.28E+01	1.47E-04
^{140}Ba	10^3	7.47E-04	4.53E-03	4.40E+00	8.28E+04	9.99E+01	1.45E+01	1.02E-02	1.11E-07
	10^7	1.78E-04	1.23E-03	3.51E+00	8.20E+04	1.00E+02	3.77E+01	1.20E-02	1.12E-07
	10^{11}	1.58E-80	9.06E-27	4.30E-12	1.13E+01	1.00E+02	6.59E+01	4.20E-02	2.70E-07
^{142}Pr	10^3	2.79E-02	9.87E-03	1.27E+00	9.16E+04	1.00E+02	9.52E+01	3.09E-01	1.09E-06
	10^7	2.14E-02	8.32E-03	1.01E+00	9.08E+04	1.00E+02	9.89E+01	3.74E-01	1.10E-06
	10^{11}	9.20E-76	4.68E-25	1.26E-12	1.25E+01	1.00E+02	9.99E+01	2.46E+00	3.12E-06
^{198}Au	10^3	5.57E-06	2.33E-05	6.61E-01	8.36E+04	1.00E+02	6.50E+00	9.42E-05	2.14E-10
	10^7	2.40E-06	5.47E-06	5.26E-01	8.30E+04	1.00E+02	2.11E+01	1.12E-04	2.14E-10
	10^{11}	9.75E-82	3.89E-29	6.44E-13	1.14E+01	1.00E+02	5.54E+01	4.63E-04	5.43E-10
^{204}Au	10^3	3.72E+00	1.62E+00	3.19E+00	9.29E+04	1.00E+02	9.98E+01	1.92E+01	1.32E-04
	10^7	3.52E+00	1.56E+00	2.65E+00	9.23E+04	1.00E+02	1.00E+02	2.27E+01	1.33E-04
	10^{11}	5.42E-68	2.02E-21	2.10E-11	1.27E+01	1.00E+02	1.00E+02	8.81E+01	5.12E-04
^{204}Tl	10^3	4.41E-05	2.69E-05	2.71E-01	5.31E+04	1.00E+02	4.97E+01	1.75E-03	2.11E-09
	10^7	4.10E-06	1.13E-05	2.16E-01	5.27E+04	1.00E+02	7.61E+01	2.05E-03	2.12E-09
	10^{11}	1.88E-82	9.52E-29	2.64E-13	7.24E+00	1.00E+02	8.85E+01	6.27E-03	4.98E-09

Table 5.10: Same as Table 5.7, but for U1F rates.

Nucleus	ρY_e	$\lambda_{total}(s^{-1})$				Percentage contribution of EC			
		T_9=1.5	T_9=5	T_9=10	T_9=30	T_9=1.5	T_9=5	T_9=10	T_9=30
^{72}As	10^3	6.34E-03	5.78E-03	1.24E+00	4.06E+04	9.30E-02	4.75E+01	9.99E+01	1.00E+02
	10^7	1.31E-02	1.63E-02	1.55E+00	4.09E+04	5.16E+01	8.11E+01	9.99E+01	1.00E+02
	10^{11}	5.64E+06	6.58E+06	9.55E+06	7.62E+07	1.00E+02	1.00E+02	1.00E+02	1.00E+02
^{84}Rb	10^3	9.49E-05	4.34E-04	1.26E-01	1.99E+04	1.84E+00	9.32E+01	1.00E+02	1.00E+02
	10^7	2.18E-03	1.93E-03	1.58E-01	2.01E+04	9.57E+01	9.84E+01	1.00E+02	1.00E+02
	10^{11}	2.28E+06	4.00E+06	6.19E+06	5.18E+07	1.00E+02	1.00E+02	1.00E+02	1.00E+02
^{102}Rh	10^3	9.49E-05	4.34E-04	3.27E+00	1.26E+05	1.84E+00	9.32E+01	1.00E+02	1.00E+02
	10^7	2.18E-03	1.93E-03	4.10E+00	1.26E+05	9.57E+01	9.84E+01	1.00E+02	1.00E+02
	10^{11}	2.28E+06	4.00E+06	2.84E+07	2.26E+08	1.00E+02	1.00E+02	1.00E+02	1.00E+02
^{122}Sb	10^3	1.76E-05	3.31E-03	1.60E+00	1.29E+05	7.61E+01	1.00E+02	1.00E+02	1.00E+02
	10^7	1.63E-02	1.57E-02	2.01E+00	1.30E+05	1.00E+02	1.00E+02	1.00E+02	1.00E+02
	10^{11}	1.16E+07	1.67E+07	4.05E+07	2.86E+08	1.00E+02	1.00E+02	1.00E+02	1.00E+02
^{120}I	10^3	3.14E-02	2.95E-01	9.40E+01	5.56E+05	1.11E-01	9.36E+01	1.00E+02	1.00E+02
	10^7	8.10E-02	1.39E+00	1.18E+02	5.61E+05	6.13E+01	9.86E+01	1.00E+02	1.00E+02
	10^{11}	3.28E+07	7.31E+07	1.50E+08	7.52E+08	1.00E+02	1.00E+02	1.00E+02	1.00E+02
^{124}I	10^3	1.22E-03	1.49E-02	1.36E+01	2.25E+05	1.67E+00	9.70E+01	1.00E+02	1.00E+02
	10^7	2.22E-02	7.17E-02	1.71E+01	2.28E+05	9.46E+01	9.94E+01	1.00E+02	1.00E+02
	10^{11}	1.49E+07	2.66E+07	5.60E+07	3.70E+08	1.00E+02	1.00E+02	1.00E+02	1.00E+02
^{126}I	10^3	6.87E-05	4.18E-03	5.78E+00	1.63E+05	1.82E+01	9.96E+01	1.00E+02	1.00E+02
	10^7	1.40E-02	2.01E-02	7.26E+00	1.65E+05	9.96E+01	9.99E+01	1.00E+02	1.00E+02
	10^{11}	1.51E+07	2.02E+07	4.37E+07	3.02E+08	1.00E+02	1.00E+02	1.00E+02	1.00E+02
^{132}La	10^3	2.97E-03	1.16E-01	3.72E+01	2.85E+05	5.45E-01	9.91E+01	1.00E+02	1.00E+02
	10^7	3.17E-02	5.67E-01	4.66E+01	2.88E+05	9.07E+01	9.98E+01	1.00E+02	1.00E+02
	10^{11}	1.85E+07	2.65E+07	6.07E+07	4.06E+08	1.00E+02	1.00E+02	1.00E+02	1.00E+02
^{198}Tl	10^3	5.62E-04	6.64E-03	1.21E+01	1.78E+05	4.91E+00	9.74E+01	1.00E+02	1.00E+02
	10^7	2.31E-02	3.14E-02	1.52E+01	1.79E+05	9.77E+01	9.94E+01	1.00E+02	1.00E+02
	10^{11}	1.41E+07	1.80E+07	5.58E+07	3.06E+08	1.00E+02	1.00E+02	1.00E+02	1.00E+02

5.7 Percentage contribution of GT and U1F rates to total rates for selected heavy isotopes

Figures 5.9 and 5.10 show the contribution of allowed and U1F rates to total transition probabilities. The bar graphs are shown at stellar density 10^7 g/cm^3 and at temperatures 5×10^9 K. For all nuclei large contribution of U1F rates to total rates is seen at low and higher temperature region. At higher temperature (T_9=30) the contribution of U1F rates increases further both at low and high density regions. Our calculation shows that for some nuclei, forbidden transitions have big contributions to total rates. The significant contribution of U1F strength to total beta decay strength distribution, for many nuclide, was also calculated by Homma *et al.* [36]. The weak-rates reported here has contributions only from U1F transitions. It is desirable to examine the contribution of non-unique forbidden transitions to the calculated β-decay half-lives and which would be taken up as a future project.

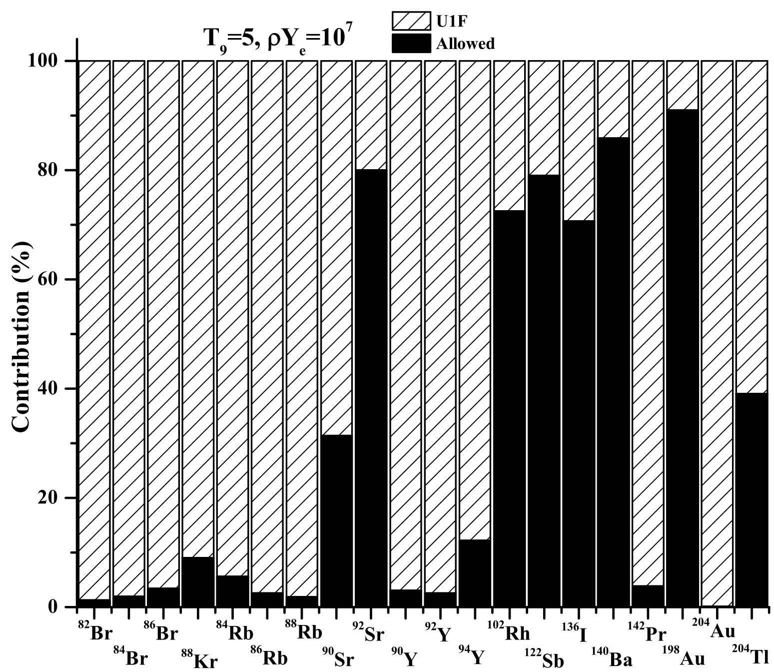

Figure 5.9: Contribution of allowed and U1F transitions to total rates in β-decay direction. Stellar density (ρY_e) is given in units of g/cm^3, whereas temperature (T_9) is given in units of 10^9 K.

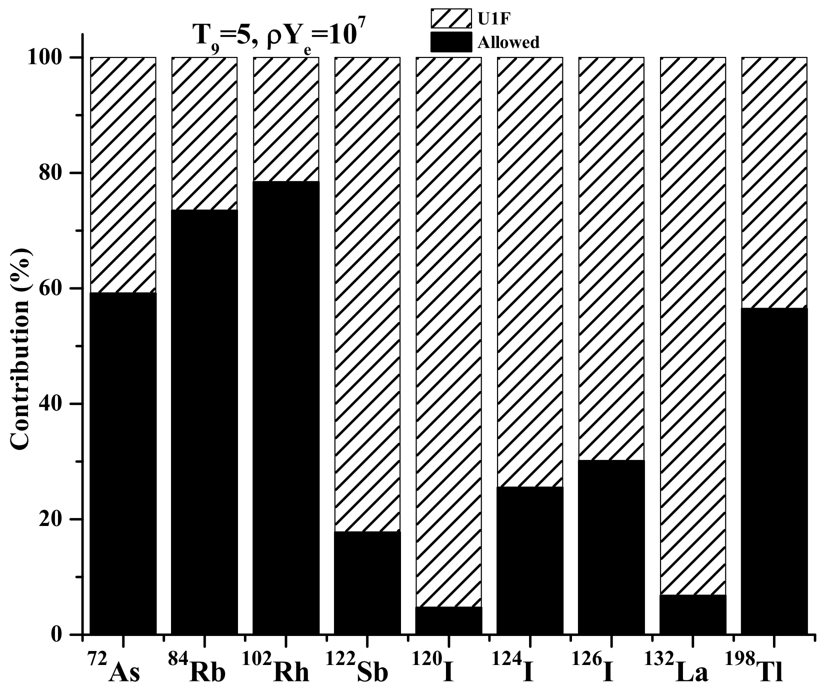

Figure 5.10: Contribution of allowed and U1F transitions to total rates in EC direction. Stellar density (ρY_e) is given in units of g/cm^3, whereas temperature (T_9) is given in units of 10^9 K.

5.8 Conclusions

The deformed pn-QRPA model was used for the calculation of GT + U1F lepton capture rates for neutron-rich copper nuclide in mass range $72 \leq A \leq 82$. We calculated the weak-rates (GT + U1F) over a broad range of density (10–10^{11} g/cm^3) and temperature (0.01 – 30 GK). The EC rates on copper isotopes were found to be important specially in high temperature and high density regions. It was also concluded that at high stellar temperature the PC rates dominate well over the β-decay rates and must be taken into account by core-collapse simulators to depict a realistic picture of the process.

The allowed GT as well as U1F $|\Delta J| = 2$ transitions strength in odd-odd and even-even nuclei in mass range $70 \leq A \leq 214$ are calculated. Two different pn-QRPA models were considered with a schematic separable interaction to compute GT and U1F transitions. The inclusion of U1F strength improved the overall matching of computed β-decay half-lives in both models. The ft values and reduced transition probabilities for the $2^- \longleftrightarrow 0^+$ transitions were also calculated. We compared our calculations with the previously reported correlated RPA calculation and experimental results. Our calculated results agreed well with the experimental results. Supernova simulators are urged to test run our computed rates for probable interesting outcomes.

Chapter 6

Summary and future work

6.1 Summary

The allowed GT and first-forbidden charge-changing transitions are considered to play a key role in numerous nuclear/astrophysical processes. A precise understanding of weak reaction properties of heavy nuclei is essential towards the understanding of supernova explosion, especially for the comprehension of the r-process nucleosynthesis. The focus of this thesis is to study stellar weak interaction rates on astrophysically significant *fp*-shell nuclide. For the calculation of weak-rates in stellar content, we have used the deformed pn-QRPA model with separable Gamow-Teller forces and the nuclear deformation parameter is considered. The stellar weak interaction rates (GT and U1F) are computed over broad range of stellar temperature (0.01 GK – 30 GK) and density ($10 - 10^{11}$ g/cm^3) domain for astrophysical applications. The brief summary of our findings are as follows.

- The electron capture (EC) rates are calculated for chromium nuclide having mass range $42 \leq A \leq 65$, including neutron-deficient and neutron-rich isotopes.
- The selections of interaction constant parameters (χ and κ) were done in an optimum way to reproduce the available experimental half-lives and satisfy the Ikeda sum rule (ISR). For allowed GT the value of χ is deduced 4.2/A (MeV), displaying a $1/A$

dependence and κ to be 0.10 MeV.

- The pn-QRPA model EC rates are compared with the pioneering work of FFN and LSSM. The pn-QRPA calculated rates are enhanced as compared to the FFN and LSSM rates.

- It is observed that in $^{42-47}$Cr nuclide at stellar temperatures (1, 5, and 10)$\times 10^{9} K$ and density 10^{7} gcm^{-3}, β^{+} rates are greater than the EC rates by 1-2 orders of magnitude and must be taken into account in simulation codes. At high densities $(10^{9} - 10^{11})$ g/cm^{3} the EC rates are bigger than the competing β^{+}-decay rates by 1-4 orders of magnitude. As $N \geq Z$, the EC rates exceed the competing β^{+} values both in low and high temperature and density region. The positron emission (PE) values decreases as the neutron number (N) increases. For N $\geq$ 31, the calculated PE rates become less than 10^{-100} and can safely be neglected.

- The charge-changing GT transitions and EC rates for odd-A medium-heavy nuclei (^{45}Sc and ^{55}Mn) are calculated in β^{+} direction. The pn-QRPA results are compared with both theoretical (including shell and other QRPA models) and measured charge-changing reaction data. The pn-QRPA calculation are found in decent agreement with the measured data.

- In Cole et al. study, it was concluded that QRPA results exhibit larger deviations and overestimate the total experimental GT strength. This work has probed the finding of the Cole et al. work and provide useful information that this is not true for all kind of QRPA models.

- The charge-changing transitions (β-decay and EC directions) and lepton capture rates for neutron-rich nickel isotopes ($^{66-71}$Ni) are calculated. The computed capture rates of lepton are compared with the Pruet and Fuller calculation. The overall comparison demonstrates that, at lower stellar densities and higher temperatures, pn-QRPA EC computed rates are larger by two orders of magnitude. It is further found that at higher temperatures the lepton capture (electron and positron) weak-rates are the dominant mode for the stellar weak rates and the corresponding lepton emission rates may be neglected.

- The allowed GT as well as U1F weak-rates for copper isotopes having mass range 72 $\leq$ A $\leq$ 82 and for neutron rich odd-odd and even-even nuclei with mass range $70 \leq A \leq 214$ are calculated.
- The deformed pn-QRPA computed terrestrial half-lives values are found in decent agreement with measured values. It is noted that the addition of U1F transition in pn-QRPA calculation improves the overall comparison with the experimental data.
- The positron capture (PC) rates must be taken into consideration at high core temperatures as they well dominate the competing electron emission rates for most of the copper isotopes. At $T_9 = 30$, the calculated PC rates contribute almost 100% for all copper isotopes.
- The lepton capture rates of copper isotopes need to be taken into account in all prespernova evolution simulation codes at high temperatures.
- The ft values and reduced matrix elements for the $\Delta J = 2$ transitions, in the mass region $70 \leq A \leq 214$, are determined. It is observed that the pn-QRPA calculated results agreed well with the experimental results and proved to be a considerable improvement over previous RPA calculations.
- The calculated charge-changing transition strength for deformed nuclei are found more fragmented than those calculated without the nuclear deformation parameter.

6.2 Future work

- (Anti)neutrinos are produced in weak-decay processes, and escape from the stellar content having densities less than 10^{11} g/cm^3. They take away energy and reduce the stellar core entropy. Therefore, the microscopic calculations of these antineutrino and neutrino cooling rates are necessary for the better understanding of supernova physics. On the other hand, gamma emission rates are considered to affect remarkably the core growth and increase the entropy of the core. These competing cooling and heating rates control the evolutionary phases of the stellar core. Therefore the accurate calculations of these cooling and heating rates are of central importance, which can be done in future.

- The first-forbidden transitions become important, in the circumstances where allowed GT transitions are unfavored, specifically for neutron-rich nuclide due to phase space considerations. Our findings show that the addition of unique first-forbidden transitions ($|\Delta J| = 2$) to the allowed GT rates improves the overall comparison with the measured data. However the non-unique forbidden transition contributions (rank 0 and rank 1) are also very important, but such contributions are currently missing in our calculation. We plan to calculate non-unique FF transitions in future.

- The same study can be performed for a number of astrophysically important *fp*- and *fpg*-shell nuclide and it is expected to achieve some more interesting results.

- In our model the pairing gap is considered to be independent of temperature. Also in our model the nuclear Fermi surface is smeared due to pairing correlations only. The high temperature corrections are applicable at stellar temperatures $T_9 = 50$–60 for light and intermediate nuclei and as low as $T_9 = 14$ for heavy nuclei. We did not incorporate any high temperature corrections in our calculation. The complete finite-temperature effects on the GT transition functions (applicable at high stellar temperatures exceeding 10^{10} K) and on the pairing correlations can be studied in future and it is hoped to get some more realistic outcomes of supernova mechanism.

- The beta-delayed neutron and proton emission rates and probabilities over wide range of stellar temperatures and densities can be calculated in future.

- The same pn-QRPA model can be used to calculate the electron capture cross-section for these selected nuclide. I hope to investigate this in future.

Bibliography

[1] D. A. Ostlie and B. W. Carroll, Modern Stellar Astrophysics, Adison-Wesley Publishing Company, Inc., Boston, (1996).

[2] G. M. Fuller, W. A. Fowler and M. J. Newman, Ap. J. Sup. Ser. **42**, 447 (1980); Ap. J. Sup. Ser. **48**, 279 (1982); Ap. J. Sup. Ser. **252**, 715 (1982).

[3] B. R. Martin, Nuclear and Particle Physics: an introduction, John Wiley Sons, New York, (2006).

[4] F. R. Stephenson and D. A. Green, Historical Supernovae and their Remnants, Clarendon Press, Oxford, (2002).

[5] L. A. Marschall, The Supernova Story, Plenum Press, New York, (1988).

[6] W. R. Hix, O. E. B. Messer, A. Mezzacappa, M. Liebendörfer, J. Sampaio, K. Langanke, D. J. Dean and G. Martínez-Pinedo, Phys. Rev. Lett. **91**, 201102 (2003).

[7] H. A. Bethe, G. E. Brown, J. Applegate and J. M. Lattimer, Nucl. Phys. A **324**, 487 (1979).

[8] K. Langanke and G. Martínez-Pinedo, Rev. Mod. Phys. **75**, 819 (2003).

[9] NASA's Hubble Space Telescope, (2007). http://hubblesite.org/newscenter/archive/releases/2007/10/

[10] J. Stephen Smartt, Annu. Rev. Astron. Astrophys. **47**, 63 (2009).

[11] M. S. Smith and K. E. Rehm, Annu. Revi. Nucl. Par. Sci. **51**, 91 (2001).

[12] E. M. Burbidge, G. R. Burbidge, W. A. Fowler and F. Hoyle, Rev. Mod. Phys. **29**, 547 (1957).

[13] A. G. W. Cameron, Pub. Astron. Soc. Pac. **69**, 201, 1957; Astr. J. **62**, 9 (1957).

[14] M. Busso, R. Gallino and G. J. Wasserburg, Annu. Rev. Astron. Astrophys. **37**, 239 (1999).

[15] F. Herwig, Annu. Rev. Astron. Astrophys. **43**, 435 (2005).

[16] A. I. Karakas and J. C. Lattanzio, Publ. Astron. Soc. Aust. **31**, 30 (2014).

[17] F.-K. Thielemann, A. Arcones, R. Käppeli, M. Liebendörfer, T. Rauscher, C. Winteler, C. Fröhlich, I. Dillmann, T. Fischer, G. Martínez-Pinedo and K. Langanke, Prog. Part. Nuc. Phys. **66**, 346 (2011).

[18] M. Lugaro, Stardust from Meteorites: an introduction to presolar grains, World Scientific, (2005).

[19] J. J. Cowan and F.-K. Thielemann, Phys. Today **57**, 47 (2004).

[20] G. Gamow and E. Teller, Phys. Rev. **49**, 895 (1936).

[21] S. M. Wong, Introductory Nuclear Physics, John Wiley Sons, New York, (1998).

[22] I. N. Borzov, Nucl. Phys. A **777**, 645 (2006).

[23] J.-U. Nabi, Adv. Space Res. **46**, 1191 (2010).

[24] Q. Zhi, E. Caurier, J. J. Cuenca-García, K. Langanke, G. Martínez-Pinedo and K. Sieja, Phys. Rev. C **87**, 025803 (2013).

[25] O. Civitarese and J. Suhonen, Nucl. Phys. A **607**, 152 (1996).

[26] V. I. Tretyak and Y. G. Zdesenko, At. Data Nucl. Data Tables **61**, 43 (1995).

[27] M. Moe and P. Vogel, Ann. Rev. Nucl. Part. Sci. **44**, 247 (1994).

[28] K. Takahashi and M. Yamada, Prog. Theor. Phys. **41**, 1470 (1969).

[29] J. A. Halbleib and R. A. Sorensen, Nucl. Phys. A **98**, 542 (1967).

[30] J. Randrup, Nucl. Phys. A **207**, 209 (1973).

[31] K. Muto, E. Bender and H. V. Klapdor-Kleingrothaus, Z. Phys. A **333**, 125 (1989).

[32] P. Möller and J. Randrup, Nucl. Phys. A **514**, 1 (1990).

[33] H. V. Klapdor, J. Metzinger and T. Oda, At. Data Nucl. Data Tables **31**, 81 (1984).

[34] M. Hirsch, A. Staudt, K. Muto and H. V. Klapdor-Kleingrothaus At. Data Nucl. Data Tables **53**, 165 (1993).

[35] A. Staudt, E. Bender, K. Muto and H. V. Klapdor-Kleingrothaus, At. Data Nucl. Data Tables **44**, 79 (1993).

[36] H. Homma, E. Bender, M. Hirsch, K. Muto, H. V. Klapdor-Kleingrothaus and T. Oda, Phys. Rev. C **54**, 2972 (1996).

[37] I. Kenar, C. Selam and A. Kucukbursa, Math. Comp. App. **10**, 2 (2005).

[38] J.-U. Nabi and H. V. Klapdor-Kleingrothaus, Eur. Phys. J. A **5**, 337 (1999).

[39] J.-U. Nabi and H. V. Klapdor-Kleingrothaus, At. Data Nucl. Data Tables **71**, 149 (1999).

[40] J.-U. Nabi and H. V. Klapdor-Kleingrothaus, At. Data Nucl. Data Tables **88**, 237 (2004).

[41] J.-U. Nabi and S. Stoica, Astrophys. Space Sci. **349**, 843 (2014).

[42] M. C. Vetterli, O. Häusser, R. Abegg, W. P. Alford, A. Celler, D. Frekers, R. Helmer, R. Henderson, K. H. Hicks, K. P. Jackson, R. G. Jeppesen, C. A. Miller, K. Raywood and S. Yen, Phy. Rev. C **40**, 559 (1989).

[43] W. G. Love and M. A. Franey, Phys. Rev. C **24**, 1073 (1981).

[44] W. P. Alford, R. L. Helmer, R. Abegg, A. Celler, D. Frekers, P. Green, O. Häusser, R. Henderson, K. Hicks, K. P. Jackson, R. Jeppesen, C. A. Miller, A. Trudel, M. Vetterli, S. Yen, R. Pourang, J. Watson, B. A. Brown and J. Engel, Nucl. Phys. A **514**, 49 (1990).

[45] E. W. Grewe, C. Bäumer, A. M. van den Berg, N. Blasi, B. Davids, D. De Frenne, D. Frekers, P. Haefner, M. N. Harakeh, M. Huynyadi, E. Jacobs, B. Junk, A. Korff, A. Negret, P. von Neumann-Cosel, L. Popescu, S. Rakers and H. J. Wörtche, Phys. Rev. C **69**, 064325 (2004).

[46] M. Hagemann, A. M. van den Berg, D. de Frenne, V. M. Hannen, M. N. Harakeh, J. Heyse, M. A. de Huu, E. Jacobs, K. Langanke, G. MartínezPinedo and H. J. Wörtche, Phys. Lett. B 579, **251** (2004).

[47] R. Helmer, Can. J. Phys. **65**, 588 (1987).

[48] J. Rapaport and E. Sugarbaker, Annu. Rev. Nucl. Part. Sci. **44**, 109 (1994).

[49] N. Bohr and J. A. Wheeler, Phys. Rev. **56**, 426 (1939).

[50] E. Cameron, Ann. Rev. Nucl. Sci. **8**, 299 (1958).

[51] K. Takahashi, M. Yamada and T. Kondoh, At. Data Nucl. Data Tables **12**, 101 (1975).

[52] T. Tachibana, M. Yamada and N. Yoshida, Prog. Theor. Phys. **84**, 641 (1992).

[53] H. Nakata. T. Tachibana and M. Yamada, Nucl. Phys. A **625**, 521 (1997).

[54] R. F. Casten, Nuclear Structure from a Simple Perspective, Oxford University Press, (1990).

[55] F. Iachello and P. Van Isacker, The Interacting Boson Fermion Model, Cambridge University Press, Cambridge, England, (1991).

[56] J. D. Walecka, Ann. Phys. **83**, 491 (1974).

[57] J. Boguta and A. R. Bodmer, Nucl. Phys. A **292**, 413 (1977).

[58] Y. C. Sugahara and H. Toki, Nucl. Phys. A **579**, 557 (1994).

[59] H. Lenske and C. Fuchs, Phys. Lett. B **345**, 355 (1995).

[60] M. Honma, T. Mizusaki and T. Otsuka, Phys. Rev. Lett. **77**, 3315 (1996).

[61] T. Mizusaki, M. Honma and T. Otsuka, Phys. Rev. C **53**, 2786 (1996).

[62] D. J. Dean, K. Langanke, L. Chatterjee, P. B. Radha and M. R. Strayer, Phys. Rev. C **58**, 536 (1998).

[63] D. Brink, D. Phil. Thesis, Oxford University, Unpublished (1955); P. Axel, Phys. Rev. **126**, 671 (1962).

[64] M. B. Aufderheide, I. Fushiki, S. E. Woosley and D. H. Hartmann, Astro. J. Sup. Ser. **91**, 389 (1994).

[65] K. Langanke and G. Martínez-Pinedo, Nucl. Phys. A **673**, 481 (2000).

[66] J.-U. Nabi and M. Sajjad, Phys. Rev. C **76**, 055803 (2007).

[67] J.-U. Nabi, Phys. Rev. C **78**, 045801 (2008).

[68] S. Cakmak, J.-U. Nabi, T. Babacan and I. Maras, Adv. Space Res. **55**, 440 (2015).

[69] S. G. Nilsson, Mat. Fys. Medd. Dan. Vid. Selsk **29**, 16 (1955).

[70] M. Hirsch, Ph.D. Thesis, Hiedelberg University, Germany, (1992).

[71] E. U. Condon and G. H. Shortley, The Theory of Atomic Structure, Cambridge University Press, Cambridge, (1935).

[72] P. Ring and P. Schuck, The Nuclear Many-body Problem, Springer Science & Business Media, (2004).

[73] J.-U. Nabi, Ph.D. Thesis, University of Heidelberg, Germany (1999).

[74] A. Staudt, E. Bender, K. Muto and H. V. Klapdor-Kleingrothaus, At. Data Nucl. Data Tables **44**, 79 (1990).

[75] E. Bender, K. Muto and H. V. Klapdor, Phys. Lett. B **208**, 53 (1988).

[76] J. Krumlinde and P. Möller, Nucl. Phys. A **417**, 419 (1984).

[77] J. Suhonen, T. Taigel and A. Faessler, Nucl. Phys. A **486**, 91 (1988).

[78] A. Staudt, M. Hirsch, K. Muto and H. V. Klapdor-Kleingrothaus, Phys. Rev. Lett. **65**, 1543 (1990).

[79] K. Muto, E. Bender, T. Oda and H. V. Klapdor, Z. Phys. A **341**, 407 (1992).

[80] K. Muto, E. Bender and H. V. Klapdor, Z. Phys. A At. Nuc. **334**, 187 (1989).

[81] N. B. Gove and M. J. Martin, At. Data Nucl. Data Tables, **10**, 205 (1971).

[82] S., Chandrasekhar, An Introduction to the Study of Stellar Structure, University of Chicago Press (1939).

[83] A. Heger, S. E. Woosley, G. Martínez-Pinedo and K. Langanke, Astrophys. J. **560**, 307 (2001).

[84] J. Zioni, A. A. Jaffe, E. FriedMan, N. Haik, R. Schectman and D. Nir, Nucl. Phys. A **181**, 465 (1972).

[85] Y. Fujita, B. Rubio and W. Gelletly, Prog. Part. Nucl. Phys. **66**, 549 (2011).

[86] T. Adachi, Y. Fujita, P. Von Brentano, G. P. A. Berg, C. Fransen, D. D. Frenne, H. Fujita, K. Hatanaka, M. Honma and E. Jacobs, Nucl. Phys. A **788**, 70 (2007).

[87] J.-U. Nabi and C. W. Johnson, J. Phys. G **40**, 065202 (2013).

[88] A. Staudt, E. Bender, K. Muto and H. V. Klapdor, Z. Phys. A **334**, 47 (1989).

[89] A. L. Cole, T. S. Anderson, R. G. T. Zegers, S. M. Austin, B. A. Brown, L. Valdez, S. Gupta, G. W. Hitt and O. Fawwaz, Phys. Rev. C **86**, 015809 (2012).

[90] K. Ikeda, S. Fujii and J. I. Fujita, Phys. Lett. **3**, 271 (1963).

[91] I. Ragnarsson and R. K. Sheline, Phys. Scr. **29**, 385 (1984).

[92] M. Hirsch, A. Staudt, K. Muto and H. V. Klapdor-Kleingrothaus, Nucl. Phys. A **535**, 62 (1991).

[93] S. Raman, C. H. Malarkey, W. T. Milner, C. W. Nestor and P. H. Jr. Stelson, At. Data Nucl. Data Tables **36**, 1 (1987).

[94] P. Möller and J. R. Nix, At. Data Nucl. Data Tables **26**, 165 (1981).

[95] G. Audi, F. G. Kondev, M. Wang, B. Pfeiffer, X. Sun, J. Blachot and M. MacCormick, Chin. Phys. C **36**, 1157 (2012).

[96] C. Gaarde, Nucl. Phys. A **396**, 127 (1983).

[97] J.-U. Nabi and M.-U. Rahman, Phys. Lett. B **612**, 190 (2005).

[98] K. Langanke and G. Martínez-Pinedo, At. Data Nucl. Data Tables **79**, 1 (2001).

[99] M. B. Aufderheide, S. D. Bloom, G. J. Mathews and D. A. Resler, Phys. Rev. C **53**, 3139 (1996).

[100] J. Pruet and G. M. Fuller, Astrophys. J. Sup. Ser. **149**, 189 (2003).

[101] W. P. Alford, A. Celler, B. Brown, R. Abegg, K. Ferguson, R. Helmer, K. Jackson, S. Long, K. Raywood and S. Yen, Nucl. Phys. A **531**, 97 (1991).

[102] P. Sarriguren, Phys. Rev. C **87**, 045801 (2013).

[103] E. Chabanat, P. Bonche, P. Haensel, J. Meyer and R. Schaeffer, Nucl. Phys. A **635**, 231 (1998).

[104] P. Möller, J. R. Nix, W. D. Myers and W. J. Swiatecki, At. Data Nucl. Data Tables **59**, 185 (1995).

[105] A. Poves, J. Sánchez-Solano, E. Caurier and F. Nowacki, Nucl. Phys. A **694**, 157 (2001).

[106] M. Honma, T. Otsuka, B. A. Brown and T. Mizusaki, Phys. Rev. C **65**, 061301 (2004); Phys. Rev. C **69**, 034335 (2002).

[107] W. D. Arnett, Supernovae and Nucleosynthesis, Princeton University Press, Princeton, (1996).

[108] H. A. Bethe, Rev. Mod. Phys. **62**, 801 (1990).

[109] J.-U. Nabi and M.-U. Rahman, Phys. Rev. C **75**, 035803 (2007).

[110] T. Rönnqvist, T. Condé, H. Olsson, N. Ramstr̈om, E. Zorro, R. Blomgren, J. Hákansson, A. Ringbom, A. Tibell and G. Jonsson, Nucl. Phys. A **563**, 225 (1993).

[111] S. El-Kateb, K. P. Jackson, W. P. Alford, R. Abegg, R. E. Azuma, B. A. Brown, A. Celler, D. Frekers, O. Häusser, R. Helmer and R. S. Henderson, Phys. Rev. C **49**, 3129 (1994).

[112] J. Rapaport, T. Taddeucci, T. P. Welch, C. Gaarde, J. Larsen, D. J. Horen and E. Sugarbaker, Nucl. Phys. A **410**, 371 (1983).

[113] B. D. Anderson, C. Lebo, A. R. Baldwin, T. Chittrakarn, R. Madey, J. W. Watson and C. C. Foster, Phys. Rev. C **41**, 1474 (1990).

[114] J.-U. Nabi, Eur. Phys. J. A **48**, 84 (2012).

[115] J.-U. Nabi, N. Cakmak and Z. Iftikhar, Eur. Phys. J. A **52**, 1 (2016).

[116] J.-U. Nabi, Astrophys. Space Sci. **331**, 537 (2011).

[117] H. V. Klapdor, Prog. Part. Nucl. Phys. **10**, 131 (1983).

[118] K. Grotz and H. V. Klapdor, The Weak Interaction in Nuclear, Particle and Astrophysics. Adam Hilger, New York, (1990).

[119] G. McLaughlin and G. Fuller, Astrophys. J. **489**, 766 (1997).

[120] R. K. Wallace and S. E. Woosley, Astrophys. J. Sup. Ser. **45**, 389 (1981).

[121] J. Cooperstein and J. Wambach Nucl. Phys. A **420**, 591 (1984).

[122] K. Takahashi, M. Yamada, and T. Kondoh, At. Data Nucl. Data Tables **12**, 101 (1973).

[123] K. Muto, E. Bender and T. Oda, Phys. Rev. C **43**, 1487 (1991).

[124] P. Möller, B. Pfeiffer and K.-L. Kratz, Phys. Rev. C **67**, 055802 (2003).

[125] J. Engel, M. Bender, J. Dobaczewski, W. Nazarewicz and R. Surman, Phys. Rev. C **60**, 014302 (1999).

[126] I. N. Borzov, Phys. Rev. C **71**, 065801 (2005).

[127] P. Hosmer, H. Schatz, A. Aprahamian, O. Arndt, R. R. C. Clement, A. Estrade, K. Farouqi, K.-L Kratz, S. N. Liddick and A. F. Lisetskiy, Phys. Rev. C. **82**, 025806 (2010).

[128] M. Majid, J.-U. Nabi and G. Daraz, Astrophys. Space Sci. **362**, 108 (2017).

[129] J.-U. Nabi, N. Çakmak and Z. Iftikhar, Eur. Phys. J. A **52**, 5 (2016).

[130] C. M. Lederer and V. S. Shireley, Table of Isotopes, John Wiley Sons, New York, (1978).

[131] O. Civitarese, F. Krmpotić and O. A. Rosso, Nucl. Phys. A **453**, 45 (1986).